Two-Dimensional Vibrational-Electronic Spectroscopy: The Design and Development of a Novel Multidimensional Spectroscopic Technique to Directly Measure Coherent Coupling Between Vibrational and Electronic Degrees of Freedom

Zachary W. Fox

A dissertation

submitted in partial fulfillment of the

requirements for the degree of

Doctor of Philosophy

University of Washington

2018

Reading Committee:

Munira Khalil, Chair

Joshua C. Vaughan

Brandi M. Cossairt

Program Authorized to Offer Degree:

Chemistry

University of Washington

Abstract

Two-Dimensional Vibrational-Electronic Spectroscopy: The Design and Development of a Novel Multidimensional Spectroscopic Technique to Directly Measure Coherent Coupling Between Vibrational and Electronic Degrees of Freedom

Zachary W. Fox

Chair of the Supervisory Committee:

Professor Munira Khalil

Chemistry

Two-dimensional vibrational-electronic (2D VE) spectroscopy fulfills the need for a direct measure of how vibrational motions effect electron transfer. This third-order Fourier transform technique probes electronic transitions that occur after excitation of an infrared (IR) pump. The information contained within a 2D VE spectrum is outlined alongside the details of how this spectroscopy is implemented. The mixed-valent molecule $[(CN)_6Fe^{II}(CN)Ru^{III}(NH_3)_5]^-$ (FeRu), which features a cyanide bridged metal-to-metal charge transfer (MMCT) from iron to ruthenium, serves as a model to demonstrate how 2D VE can be used to study how high frequency C≡N vibrations couple to the MMCT.

The vibrational modes found to couple most strongly with the MMCT are the ones that modulate the distance between the two metal centers, specifically the bridging mode, ν_{bridge}. Spectra taken with varying delay times between excitation and detection demonstrate changes in lineshape indicative of fluctuating correlation as a function of the time between the vibrational excitation and the electronic transition. Improvements to the experiment including incorporating continuous, fast scanning and polarization selectivity allow more spectra to be taken in a shorter period of time while looking at the orientational dependence of 2D VE signal.

FeRu exhibits strong orientational dependence because of the large angles found around the metal centers. The polarization dependent 2D VE data is fit to a model which includes the orientational response function, allowing the separation of signal amplitude resulting from strong vibronic coupling and orientational alignment. The ν_{radial} mode are shown to align nearly perpendicularly to the MMCT, while the ν_{bridge} and ν_{trans} modes are found to be 3° and 9° relative to the MMCT respectively. This also improves the understanding of the coupling strength, independent of orientational factors. The ν_{bridge} mode is shown to be the dominating vibration when it comes to coupling with the MMCT with a coupling strength almost 3 times that of the similarly oriented ν_{trans} and more than 5 times stronger than the ν_{radial} mode. By separating the orientational and coupling strength components to 2D VE signal amplitude, quantitative models can be developed to fully describe 2D VE phenomena and better the understanding of vibrational-electronic coupling.

Table of Contents

List of Figures

List of Tables

Acknowledgements

There have probably been hundreds of people that I have encountered over the course of graduate school who have helped me in some small way or another. I probably haven't thanked all of them properly or even realized how much help they were providing at the time. So, I would like to start with a blanket Thank You, to all the people whose combined assistance probably got me over this finish line.

Over the past six years, I've had the pleasure to work directly with some fantastic individuals. Of course, I have to first thank Munira for helping me realize that I could do spectroscopy, even if I had never actually touched a laser before. Your guidance was instrumental, and I will always be thankful for the breadth of experience that you entrusted me with during graduate school: from building the fast scanning instrument the way I envisioned, to participating in multiple X-ray beamtimes. It was instrumental in my becoming a true scientist. Trevor, thanks for being my mentor and teaching me everything about optics. We had hours of conversations about sports and science, especially during late nights in lab trying to figure out the precise order everything had to be turned off and on again to function. I learned about the importance of details and being sure of the fundamentals by answering the obligatory set of "Trevor Questions" (did you turn it on?) which solved more of my problems than I care to admit. Along with Trevor, I also learned from the older members of the group, Karla, Anthony, and Jen, who pushed me to really understand the theory behind what we were doing every day. Madhu started in the group at the same time as I did. We spent a lot of time figuring out how to do spectroscopy, and it is always better to have someone learning right along with you and helping you work through more challenging material. Thank you for being a release from lab, discussing our plans for the future, and our dream of remodeling

the office space to include a loft and balcony (French doors and all). James came along a couple of years later, bringing a considerable amount of class to our group. His unending thirst for knowledge pushes everyone around him to be the best scientist they can possibly be, and we all owe him for that. Thanks also to Tyler for maintaining his great positivity and endless stream of dad jokes when I threw him into the deep end of 2D VE in the never-ending quest for more and better data. Finally, to Laura, Julia, and Cindy: I know you probably never want to consider making FeRu ever again, but each of you in turn became the de facto masters of the wet lab, and I am endlessly thankful!

Equally important to my success over the course of graduate school have been my friends outside of lab. That first-year office may have been freezing but sharing it with Tracey and Steve gave it a warm and friendly atmosphere anyway. Thanks to you and Brooke for being the people that I could just hang out with, playing board games and not having to think about science for an hour or two. Charlie, you've been a great friend and roommate over the years, and nothing is better than having a roommate that understands the importance of cheese-based foods and random TV after a long day in lab (I'm not sure who lost the remote this time, but I am pretty sure it is gone for good). Andrea, we've had quite a few adventures, and I am still always excited for the next one. Thanks for keeping me on task (mostly) and smiling (always). To all those in the WBR family, thank you all for being the greatest second family anyone could ever ask for. I wouldn't be the same person without the vast collection of memories and experiences from every corner of this country that I share with each and every one of you.

Finally, I have to thank my family: my parents Katie and Mark, my brother Josh, and everyone else back in Salt Lake. I am always genuinely excited when I get the chance to see you all; there

isn’t much better than hanging out in the backyard catching up with everyone and watching the dogs run around. I’m thankful to have such a supportive and loving family!

Chapter 1

Introduction

1.1 Understanding Complex Photochemical Reactions

Much of the chemistry important to life occurs in solution. When studying the way light interacts with molecular systems, spectroscopists must consider not only how the idealized molecule should interact, but also how the environment of the molecule will affect the outcome. In condensed phase systems, the molecule not only interacts with the electromagnetic field of the light, but also with its solvent environment. Additionally, the motion of the atoms and electrons within a molecule are not completely independent from one another. The motion of an electron may change the structure, and thus the associated vibrational modes of a molecule, while nuclear motion may change the potential energy surface observed by electrons within that molecule. The correlation between nuclear and electronic degrees of freedom has been linked to photosystems important to biology, chemistry, and materials science, which makes measuring these effects an important task for spectroscopists across many fields.[1–4]

This dissertation details the design and development of two-dimensional vibrational electronic (2D VE) spectroscopy, which can observe the interplay of vibrational and electronic motion. Here, experiments on intramolecular charge transfer systems reveal coherent coupling between vibrational excitations and electron motion. These are the first experiments to directly measure such an effect in the electronic ground state. In addition to demonstrating the power of this new spectroscopy, improvements in the data collection speed and sensitivity are outlined. The increase the speed at which data is collected enables additional information, quantifying the effect of this type of coupling and allows the relative angles between electronic and vibrational transition

dipoles to be extracted. Together, the experiments presented here thoroughly explore the complex interactions between vibrational and electronic degrees of freedom in intramolecular charge transfer systems.

1.2 Two-Dimensional Fourier Transform Spectroscopy

Linear spectroscopy techniques such as Fourier transform infrared (FTIR) and ultraviolet-visible (UV-vis) spectroscopies provide insight into the way a molecule absorbs light of a specific frequency. However, these linear techniques rely only on a single light-matter interaction which limits the information available. Studying how individual transitions couple to one another and respond in dynamic situations requires non-linear spectroscopies that utilize a series of interactions to extract information within complex spectra. Of particular interest are interactions between vibrational and electronic motion, which are at the center of understanding the mechanisms behind ultrafast photo-processes. Two-dimensional Fourier transform (2D FT) spectroscopies provide the information and insight to answer these questions, and the development of these techniques continues to provide a better understanding of the world around us. Experiments which exhibit unique detection schemes,[5,6] and shorter data collection times,[7,8] continue to expand the range of problems that 2D FT spectroscopy can address.

One of the fundamental challenges faced by spectroscopists is the difficulty in separating the microscopic interactions which are spectrally overlapped. For example, in linear spectroscopy, lineshapes are broadened by inhomogeneous and homogenous processes, as well as anharmonic coupling. In a linear FTIR experiment, coherent infrared (IR) light passes through the sample of interest and IR active vibrational modes will absorb photons which have energy equal to the difference between the initial vibrational state v_n and the next highest vibrational state v_{n+1}. The absorption of photons alters the spectrum of the source IR light, reducing the intensity at

frequencies associated with vibrational transitions. The speed and relative low cost of the FTIR instrument comes from the time domain detection method employed in all Fourier transform (FT) spectroscopies. The modified IR light is sent through an interferometer where the pathlength in one arm is changed relative to the other. This difference in path length corresponds to a delay in time between the two copies of the IR light, which interfere with one another as the time delay is scanned. All of the spectral information associated with the IR spectrum is encoded in the Fourier transform of this time-domain interference pattern. Instead of having to disperse the light and use a large, carefully calibrated, multi-channel detector, the intensity of the entire beam of light can be detected as a function of delay time on a single channel with a much smaller total instrument size.

Two-dimensional (2D) FT spectroscopy techniques allow time domain measurements and more complicated transfer pathways to uncover the underlying structure hidden within a linear spectrum. The 2D label refers to the *x* (ω_1) and *y* (ω_3) axes, which correspond to the energy ranges of the pump and probe beams, respectively. A simple example to demonstrate the molecular information found in 2D FT spectroscopy is to consider 2D IR spectroscopy of a coupled, two-mode, anharmonic system Figure 1-1(a). The six levels that exist in this system correspond to the ground state $|0\rangle$, the first vibrationally excited states $|a\rangle$ and $|b\rangle$, the two quanta excited state of each $|2a\rangle$ and $|2b\rangle$, and finally the mixed state $|a+b\rangle$ which is a combination band of the two vibrational states $|a\rangle$ and $|b\rangle$.

The cartoon 2D spectrum of this system (Figure 1-1(b)) exhibits 8 distinct peaks, all of which would be obscured within the two peaks in the linear spectrum. On the diagonal, where $\omega_1 = \omega_3$, positive (red) peaks indicate the combined ground state bleach (GSB) and excited state emission (ESE) pathways in which the pump and probe both interact with the same transition between the ground and first excited state, $\omega_1 = \omega_3 = \omega_{a(b)}$. This is not the only GSB pathway possible, the off-

diagonal GSB peaks will show up at $\omega_1 = \omega_{a(b)}$, $\omega_3 = \omega_{b(a)}$. The negative (blue) peaks are all pathways that interact with the second excited states. The excited state absorption (ESA) peaks occur when the probe promotes the system into the second excited state, either $|2a(b)\rangle$ or $|a+b\rangle$. The ESA peaks just below the diagonal will be shifted by the degree of anharmonicity in each mode, Δ_{aa} and Δ_{bb} in Figure 1-1(a). The ESA peaks adjacent to the cross-peak GSB features correspond to absorbance into the mixed $|a+b\rangle$ state after excitation into either $|a\rangle$ or $|b\rangle$. The energy associated with this transition is modulated by the mixed mode anharmonicity, $\Delta_{ab,}$ which is a measure of how strongly the two modes are coupled. If the system were to be perfectly harmonic, the transition energy between the ground and first excited state would match the transition energy between the first and second excited state bringing the positive and negative peaks on top of one another. Therefore, some degree of anharmonicity is required for a 2D spectrum to exhibit all possible peaks. In addition to the above information, the 2D FT spectroscopy pulse sequence Figure 1-1(c) allows the spectrum to be parametrized by the waiting time between the second pump pulse and the probe pulse, τ_2. By collecting spectra at different τ_2 delays, the researcher can elucidate dynamic information about the system, something that is not possible with linear spectroscopy.

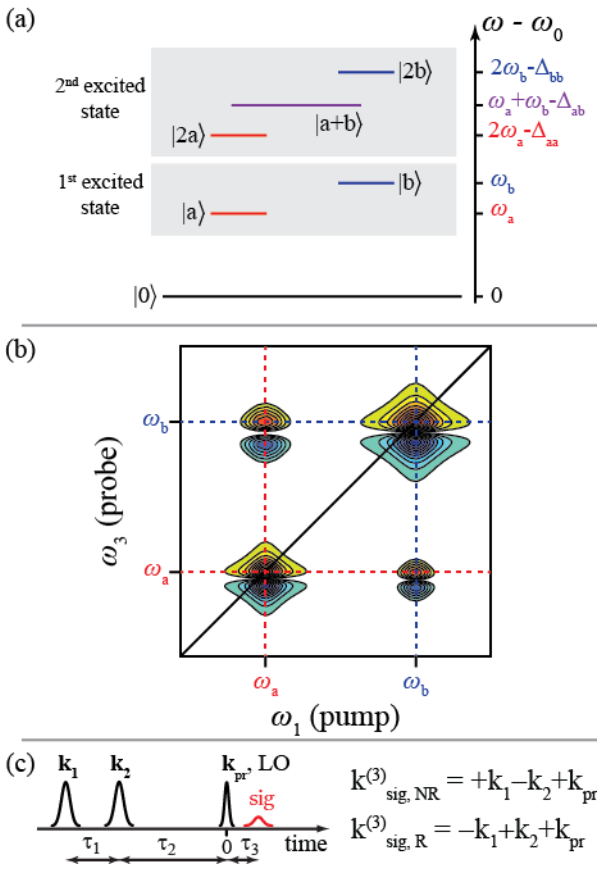

Figure 1-1 Overview of a third-order 2D IR experiment. (a) the six-level model which describes a coupled, anharmonic, two-mode system. (b) A cartoon 2D FT spectrum based on the system described in (a). A generic pulse sequence for a 2D FT experiment. In order to determine the direction in which the signal is emitted, the wavevectors of the pulses responsible are added together. Because $\mathbf{k}_1$ and $\mathbf{k}_2$ should be identical pulses, the non-rephasing (NR) and rephasing (R) pathways are dependent on pulse ordering. In experiments which use dispersive detection of either the local oscillator (LO) or the probe, ω_3 is defined as 0.

Two-dimensional Fourier transform spectroscopy begins with a pulse sequence of three temporally distinct laser pulses (Figure 1-1(c)). The time delay between the first two pulses, τ_1, is used to create the time-domain axis by which the FT spectroscopy gets its name. Scanning along τ_1 creates interference between the second pump pulse and the coherence created by the first pump pulse. Taking the Fourier transform of the resulting interference determines which pump frequencies interacted with the sample. The signal in a 2D FT experiment is emitted in the direction required to conserve momentum. Therefore, adding the wavevectors of the incoming pulses will define the emittance direction of the signal (Figure 1-1(c)).

2D FT spectroscopies are uniquely flexible because the same pulse sequence can be used to study different phenomena dependent only on the energy of light used. 2D electronic spectroscopy (2D ES) and 2D infrared (2D IR) spectroscopies allow researchers to study the electronic (E) and vibrational (V) landscape of molecules to better understand a host of phenomena including energy-transfer, correlated electronic states and vibrational modes, and hydrogen bonding dynamics in proteins and liquids.[1,3,9–11] Though powerful, 2D ES and 2D IR spectroscopy do not directly probe the extreme off-diagonal peaks associated with the coupling between electronic and vibrational transitions. The first experimental success in that area was accomplished by Fleming et al. with the introduction of 2D EV.[12] The 2D EV experiment has been used to study direct coupling between electronic excitations and vibrational modes in molecular aggregates, biologically important photoreceptors, and intramolecular charge transfer,[13–15] while understanding of the lineshapes and dynamics associated with such an experiment continue to increase.[16–18] Another way to look at directly coupled vibrations and electron motion as in 2D EV spectroscopy is the complimentary 2D VE experiment, which pumps the vibrational transitions and probes how those excited vibrational states modulate an electronic transition.

The pulse sequence that is used in 2D VE matches the generic pulse sequence of many 2D FT experiment (see Figure 1-1(c)) except, as in 2D EV, the energy range of the pump and probe are significantly different, $\omega_1 << \omega_3$. This means that the experiment is focused exclusively on cross-peaks between the mid-IR (MIR) pumps and the optical probe. The pump pulses are used to excite a vibrational mode before the electronic transition dependent on the probe occurs. Some of the unique features of 2D VE spectroscopy come from the fact that the spectroscopic window is restricted to only detect cross-peaks. Many of the features discussed in Figure 1-1(b) are not present, and the ESE pathways are all completely forbidden because they would require an

electronic emission from the ground electronic state. Therefore only the GSB and ESA pathways Figure 1-2(a,b) can occur. As a result, the simulated 2D VE spectrum shown in Figure 1-2(d) looks significantly simpler than the 2D IR cartoon in Figure 1-1(b).

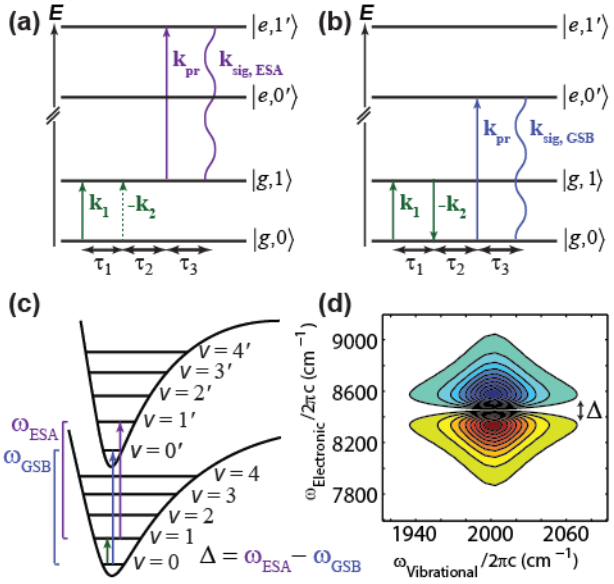

Figure 1-2 Details of the spectroscopic features found in 2D VE spectroscopy. The MIR pumps (green) only excited vibrations in the ground electronic state, lower potential well in (c). If the vibrational states, *v*, couple with the electronic state transition, a peak will be present in the simulated 2D VE spectrum shown in (d). The two peaks arising from the GSB and ESA will be separated by the quantity Δ which is dependent on the difference between the energy of the electronic transitions probed.

1.3 Metal-to-Metal Charge Transfer Model System

When choosing the initial model system to validate this new spectroscopic method, mixed valence compounds which exhibit intramolecular metal-to-metal charge transfer (MMCT) make for a smart choice for measuring vibrational-electronic correlation. This class of mixed metal dimers and trimers have been used to study the coupling between electronic and vibrational motions in both steady-state and time resolved experiments.[19–27] Many of these compounds exhibit complicated interactions in the condensed phase with the solvent bath interactions and structural rearrangement modifying the electron transfer process inherent to these systems.[28–33] Throughout this dissertation, the mixed-valence, MMCT molecule $Na[(CN)_5Fe^{II}(CN)Ru^{III}(NH_3)_5]$, referred to

as FeRu, is used as the model system. This molecule serves as an excellent model system as the photo-induced charge transfer has been repeatedly linked to higher frequency C≡N vibrational modes, $\nu_{CN,}$ by a range of experiments including transient-IR, and transient absorption spectroscopies, as well as resonance Raman.[21,24,25] These vibrations provide distinct markers in the IR region for an experiment especially when dissolved in formamide (FA) as shown in Figure 1-3. The high degree of solvent interaction previously studied in the Khalil group means that when dissolved in FA, the four IR active ν_{CN} transition centers shift apart from one another.[34] previous 2D IR work provided the ν_{CN} mode assignments and transition centers in FA as: ν_{trans}, 2002 cm^{-1}; ν_{radial}, 2049 cm^{-1}; ν_{axial}, 2065 cm^{-1}; and ν_{bridge}, 2096 cm^{-1}.[35]

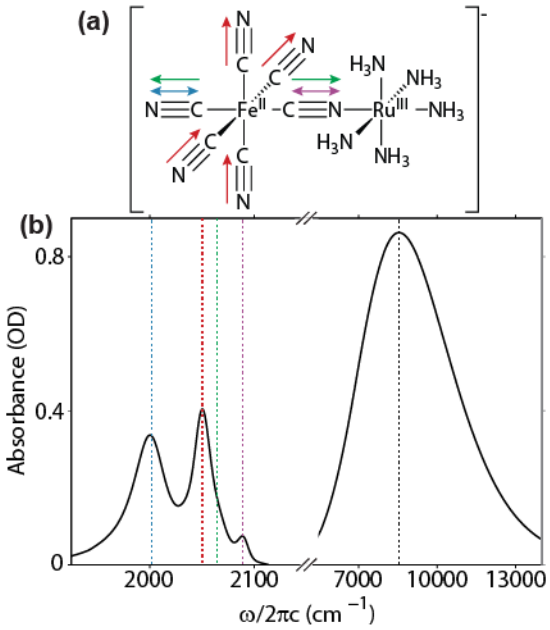

Figure 1-3 Overview of the FeRu MMCT model system. (a) The four vibrational modes, ν_{trans} (blue), ν_{radial} (red), ν_{axial} (green), and ν_{bridge} (purple) are color-coded and shown in relation to the molecular structure. The linear spectra of FeRu dissolved in formamide solvent, including both FTIR and UV-visible, are shown in (b). The transition centers for each ν_{CN} mode are given by the dashed vertical line matching its previously defined color, and the MMCT transition (8547 cm^{-1}) is shown with the black dashed vertical line.

The demonstrated coupling between the ν_{CN} modes and the MMCT is expected considering the structure of the molecule (Figure 1-3(a)). The MMCT transfers an electron from the Fe^{II} to the

Ru^{III}, resulting in an excited state molecule featuring Fe^{III} and Ru^{II} which undergoes rapid back electron transfer resulting in significant excitation of the ν_{CN} modes.[24] The ν_{bridge} mode is directly between the two metal centers so the vibrational motion should be able to directly modulate the MMCT. This is where 2D VE spectroscopy can be used, to not only directly measure any coupling between a vibrational mode and an electron transfer, but also to distinguish between the various IR modes coupling strength. In addition, structural information such as the angle between the MMCT and the vibrational transition dipole can be extracted with polarization sensitive techniques.

1.4 Dissertation Overview

In this dissertation, I will introduce 2D VE spectroscopy with an emphasis on intramolecular charge transfer dynamics. Chapter 2 will motivate the experiment and reflect on the progress previously made towards this kind of cross-peak spectroscopy. I will also introduce the expected signals and molecular information that can be studied with 2D VE spectroscopy. The initial experimental results and proof of concept experiments are provided in Chapter 3. There, a comparison of resonant and non-resonant experiments featuring intramolecular charge transfer provide an excellent demonstration of the results one can expect from 2D VE spectroscopy. One of the biggest challenges to collecting 2D VE data, the time of data acquisition, is addressed in Chapter 4, and the introduction of a continuous fast scanning detection scheme is demonstrated. This opens the door to new 2D VE experiments that would have previously been unfeasible due to the time constraints inherent to working with ultrafast laser systems. In Chapter 5, an experiment to examine polarization dependence is fully demonstrated along with a fitting model which allows for the extraction of more physically relevant data. By introducing polarization control, the 2D VE experiment allows for the extraction of angles that relate the MMCT to the

individual vibrational dipole moments as well as a more accurate quantification of the coupling strength between them. The appendices that follow are meant to shed light on some of the more challenging aspects of the experimental design and data processing, as well as provide additional detail for the experiments described in this work. This dissertation lays the groundwork for 2D VE spectroscopy to be one of the fundamental techniques used to understand the complex interplay between vibrational motion and electron transfer.

References

(1) Mukamel, S. Multidimensional Femtosecond Correlation Spectroscopies of Electronic and Vibrational Excitations. *Annu. Rev. Phys. Chem.* **2000**, *51*, 691–729.

(2) Cho, M. Coherent Two-Dimensional Optical Spectroscopy. *Chem. Rev.* **2008**, *108* (4), 1331–1418.

(3) Jonas, D. M. Two-Dimensional Femtosecond Spectroscopy. *Annu. Rev. Phys. Chem.* **2003**, *54*, 425–463.

(4) Kraack, J. P.; Hamm, P. Surface-Sensitive and Surface-Specific Ultrafast Two-Dimensional Vibrational Spectroscopy. *Chem. Rev.* **2017**, *117* (16).

(5) Bakulin, A. A.; Silva, C.; Vella, E. Ultrafast Spectroscopy with Photocurrent Detection: Watching Excitonic Optoelectronic Systems at Work. *J. Phys. Chem. Lett.* **2016**, *7* (2), 250–258.

(6) Aeschlimann, M.; Brixner, T.; Fischer, A.; Kramer, C.; Melchior, P.; Pfeiffer, W.; Schneider, C.; Strueber, C.; Tuchscherer, P.; Voronine, D. V. Coherent Two-Dimensional Nanoscopy. *Science (80-.).* **2011**, *333* (6050), 1723–1726.

(7) Roberts, S. T.; Loparo, J. J.; Ramasesha, K.; Tokmakoff, A. A Fast-Scanning Fourier Transform 2D IR Interferometer. *Opt. Commun.* **2011**, *284*, 1062–1066.

(8) Dunbar, J. A.; Osborne, D. G.; Anna, J. M.; Kubarych, K. J. Accelerated 2D-IR Using Compressed Sensing. *J. Phys. Chem. Lett.* **2013**, *4*, 2489–2492.

(9) Thielges, M. C.; Fayer, M. D. Protein Dynamics Studied with Ultrafast Two-Dimensional Infrared Vibrational Echo Spectroscopy. *Acc. Chem. Res.* **2012**, *45* (11), 1866–1874.

(10) Hamm, P.; Lim, M.; DeGrado, W. F.; Hochstrasser, R. M. The Two-Dimensional IR Nonlinear Spectroscopy of a Cyclic Penta-Peptide in Relation to Its Three-Dimensional Structure. *Proc. Natl. Acad. Sci.* **1999**, *96* (5), 2036–2041.

(11) Roberts, S. T.; Ramasesha, K.; Tokmakoff, A. Structural Rearrangements in Water Viewed Through Two-Dimensional Infrared Spectroscopy. *Acc. Chem. Res.* **2009**, *42* (9, SI), 1239–1249.

(12) Oliver, T. A. A.; Lewis, N. H. C.; Fleming, G. R. Correlating the Motion of Electrons and Nuclei with Two-Dimensional Electronic-Vibrational Spectroscopy. *Proc. Natl. Acad. Sci. U. S. A.* **2014**, *111* (28), 10061–10066.

(13) Lewis, N. H. C.; Dong, H.; Oliver, T. A. A.; Fleming, G. R. A Method for the Direct Measurement of Electronic Site Populations in a Molecular Aggregate Using Two-Dimensional Electronic-Vibrational Spectroscopy. *J. Chem. Phys.* **2015**, *143* (12).

(14) Lewis, N. H. C.; Fleming, G. R. Two-Dimensional Electronic-Vibrational Spectroscopy of Chlorophyll a and B. *J. Phys. Chem. Lett.* **2016**, *7* (5), 831–837.

(15) Gaynor, J. D.; Courtney, T. L.; Balasubramanian, M.; Khalil, M. Fourier Transform Two-Dimensional Electronic-Vibrational Spectroscopy Using an Octave-Spanning Mid-IR Probe. *Opt. Lett.* **2016**, *41* (12), 2895–2898.

(16) Lewis, N. H. C.; Dong, H.; Oliver, T. A. A.; Fleming, G. R. Measuring Correlated Electronic and Vibrational Spectral Dynamics Using Line Shapes in Two-Dimensional Electronic-Vibrational Spectroscopy. *J. Chem. Phys.* **2015**, *142* (17).

(17) Dong, H.; Lewis, N. H. C.; Oliver, T. A. A.; Fleming, G. R. Determining the Static Electronic and Vibrational Energy Correlations via Two-Dimensional Electronic-Vibrational Spectroscopy. *J. Chem. Phys.* **2015**, *142* (17).

(18) Gaynor, J. D.; Khalil, M. Signatures of Vibronic Coupling in Two-Dimensional Electronic-Vibrational and Vibrational-Electronic Spectroscopies. *J. Chem. Phys.* **2017**, *147* (9).

(19) Barbara, P. F.; Meyer, T. J.; Ratner, M. A. Contemporary Issues in Electron Transfer Research. *J. Phys. Chem.* **1996**, *100* (31), 13148–13168.

(20) Son, D. H.; Kambhampati, P.; Kee, T. W.; Barbara, P. F. Femtosecond Multicolor Pump-Probe Study of Ultrafast Electron Transfer of [(NH3)(5)(RuNCRuII)-N-III(CN)(5)](-) in Aqueous Solution. *J. Phys. Chem. A* **2002**, *106* (18), 4591–4597.

(21) Tominaga, K.; Kliner, D. A. V; Johnson, A. E.; Levinger, N. E.; Barbara, P. F. Femtosecond Experiments and Absolute Rate Calculations on Intervalence Electron-Transfer of Mixed Valence Compounds. *J. Chem. Phys.* **1993**, *98* (2), 1228–1243.

(22) Lynch, M. S.; Slenkamp, K. M.; Khalil, M. Communication: Probing Non-Equilibrium Vibrational Relaxation Pathways of Highly Excited C N Stretching Modes Following Ultrafast Back-Electron Transfer. *J. Chem. Phys.* **2012**, *136* (24).

(23) Lynch, M. S.; Van Kuiken, B. E.; Daifuku, S. L.; Khalil, M. On the Role of High-Frequency Intramolecular Vibrations in Ultrafast Back-Electron Transfer Reactions. *J. Phys. Chem. Lett.* **2011**, *2* (17), 2252–2257.

(24) Wang, C. F.; Mohney, B. K.; Akhremitchev, B. B.; Walker, G. C. Ultrafast Infrared Spectroscopy of Vibrational States Prepared by Photoinduced Electron Transfer in (CN)(5)FeCNRu(NH3)(5)(-). *J. Phys. Chem. A* **2000**, *104* (18), 4314–4320.

(25) Wang, C. F.; Mohney, B. K.; Williams, R. D.; Petrov, V.; Hupp, J. T.; Walker, G. C. Solvent Control of Vibronic Coupling upon Intervalence Charge Transfer Excitation of (CN)(5)FeCNRu(NH3)(5)(-) as Revealed by Resonance Raman and near-Infrared

Absorption Spectroscopies. *J. Am. Chem. Soc.* **1998**, *120* (23), 5848–5849.

(26) Doorn, S. K.; Dyer, R. B.; Stoutland, P. O.; Woodruff, W. H. Ultrafast Electron-Transfer and Coupled Vibrational Dynamics in Cyanide Bridged Mixed-Valence Transition-Metal Dimers. *J. Am. Chem. Soc.* **1993**, *115* (14), 6398–6405.

(27) Tivansky, A. V; Wang, C. F.; Walker, G. C. Vibrational Mode Coupling to Ultrafast Electron Transfer in [(CN)(5)OsCNRu(NH3)(5)](-) Studied by Femtosecond Infrared Spectroscopy. *J. Phys. Chem. A* **2003**, *107* (43), 9051–9058.

(28) Reid, P. J.; Silva, C.; Barbara, P. F.; Karki, L.; Hupp, J. T. Electronic Coherence, Vibrational Coherence, and Solvent Degrees of Freedom in the Femtosecond Spectroscopy of Mixed-Valence Metal Dimers in H2O and D2O. *J. Phys. Chem.* **1995**, *99* (9), 2609–2616.

(29) Watson, D. F.; Tan, H. S.; Schreiber, E.; Mordas, C. J.; Bocarsly, A. B. Femtosecond Pump-Probe Spectroscopy of Trinuclear Transition Metal Mixed-Valence Complexes. *J. Phys. Chem. A* **2004**, *108* (16), 3261–3267.

(30) Watson, D. F.; Bocarsly, A. B. The Effects of Electronic Coupling and Solvent Broadening on the Intervalent Electron Transfer of a Centrosymmetric Mixed-Valence Complex. *Coord. Chem. Rev.* **2001**, *211*, 177–194.

(31) Jortner, J.; Bixon, M. Intramolecular Vibrational Excitations Accompanying Solvent-Controlled Electron-Transfer Reactions. *J. Chem. Phys.* **1988**, *88* (1), 167–170.

(32) Hennessy, M. H.; Soos, Z. G.; Watson, D. F.; Bocarsly, A. B. Raman Excitation Profiles with Self-Consistent Excited-State Displacements. *J. Phys. Chem. B* **2000**, *104* (46), 10909–10914.

(33) Pfennig, B. W.; Wu, Y.; Kumble, R.; Spiro, T. G.; Bocarsly, A. B. Time-Dependent Resonance Raman Analysis of a Trinuclear Mixed Valence Coordination Complex. *J. Phys. Chem.* **1996**, *100* (14), 5745–5750.

(34) Brookes, J. F.; Slenkamp, K. M.; Lynch, M. S.; Khalil, M. Effect of Solvent Polarity on the Vibrational Dephasing Dynamics of the Nitrosyl Stretch in an Fe-II Complex Revealed by 2D IR Spectroscopy. *J. Phys. Chem. A* **2013**, *117* (29), 6234–6243.

(35) Slenkamp, K. M.; Lynch, M. S.; Van Kuiken, B. E.; Brookes, J. F.; Bannan, C. C.; Daifuku, S. L.; Khalil, M. Investigating Vibrational Anharmonic Couplings in Cyanide-Bridged Transition Metal Mixed Valence Complexes Using Two-Dimensional Infrared Spectroscopy. *J. Chem. Phys.* **2014**, *140* (8), 084505.

Chapter 2

The 2D VE Experiment

The work presented in this chapter has been published in the following paper:

- *Courtney, T. L.; Fox, Z. W.; Slenkamp, K. M.; and Khalil, M., "Two Dimensional Vibrational-Electronic Spectroscopy", J. Chem. Phys.,* ***2015****, 143, 154201.*

In this chapter, I will detail the technique of 2D VE spectroscopy, including theoretical background, the experimental setup and methodology, data collection and processing, as well as discuss the presence of detected VE signals that are not resonant with all three incident fields. In this work, 2D VE spectroscopy is used to study coupled electronic and vibrational motions on an ultrafast time scale in cyanide-containing iron complexes. This new spectroscopy enables the measurement of the cross-peaks between cyanide stretching vibrations (ν_{CN}) and a charge transfer transition in two molecules: $[Fe^{III}(CN)_6]^{3-}$, which has a ligand-to-metal charge transfer (LMCT) transition, and $[(CN)_5Fe^{II}–CN–Ru^{III}(NH_3)_5]^{-}$ (FeRu), which has a metal-to-metal charge transfer (MMCT) transition.

2.1 Introduction

The coupling of vibrational and electronic degrees of freedom dictates energy localization/delocalization and transfer pathways in photochemical processes in solution. Our ability to understand and eventually control energy transfer in molecules and materials hinges on being able to measure coupled vibrational and electronic motion in complex systems. 2D femtosecond Fourier transform (FT) spectroscopy is a coherent technique with the high time and frequency resolution necessary for probing both electronic and vibrational couplings.[1,2] Numerous experimental methods of coherent 2D electronic and infrared (IR) spectroscopies have evolved over recent years, which extend the spectral range and applications of this multidimensional

Fourier transform technique. Driven by new technologies and motivated by the desire to gain a deeper understanding of molecular and solid-state systems, researchers have expanded 2D electronic spectroscopy (2D ES) experiments in the near-IR[1–5] and visible[6,7] spectral regions, thus filling out the 2D ES spectral window shown in Figure 2-1. Recent efforts include broadband and two-color spectroscopies in the visible region (slightly off-diagonal 2D ES peaks, Figure 2-1),[8–11] accessing lower energy electronic transitions in the short-wave IR region,[12–14] and collection of 2D spectra at progressively shorter wavelengths into the deep UV[15–20] (overall top right of Figure 2-1). Collectively, the 2D ES experiments have enriched our understanding of coherent and incoherent energy transfer among coupled excitons in molecular, biological and material systems. Similarly, researchers have developed 2D IR spectroscopies[21–26] to understand complex phenomena in a variety of molecular and materials systems. Signals from these early experiments across the mid-IR spectrum lie along the diagonal of the 2D IR spectral window in Figure 2-1. Experiments in new 2D spectral regions include the introduction of mid-IR two-color and broadband-probe 2D spectroscopies (off-diagonal 2D IR peaks, Figure 2-1)[27–30] and the extension of 2D IR spectroscopy to study low frequency vibrations in the long-wave IR region[31] and into the THz domain.[32,33] (overall bottom left of Figure 2-1). 2D IR spectroscopy continues to play an important role in furthering our understanding of non-covalent interactions, structural fluctuations, and vibrational energy transfer dynamics in complex systems.

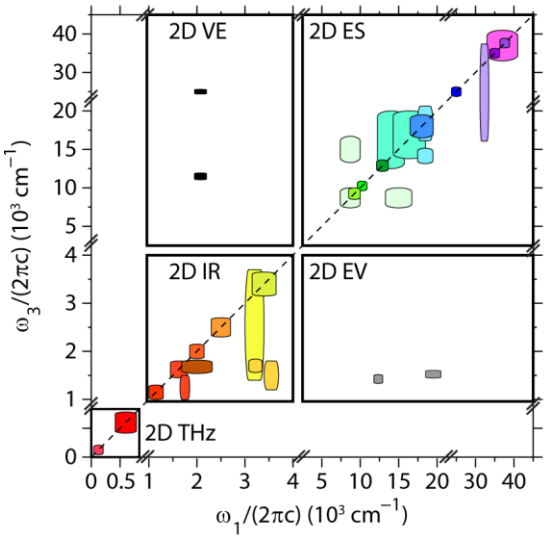

Figure 2-1 Spectral landscape of femtosecond 2D FT spectroscopies. Existing 2D vibrational spectroscopies, which span mid-IR through THz spectral regions, and 2D electronic spectroscopies (2D ES), which include short-wave IR through deep UV wavelengths, are depicted mainly along the diagonal of the ω_3 (detection) and ω_1 (excitation) axes. Some broadband (in ω_3 or both domains) and two-color experiments reach beyond the diagonal. Developing spectroscopies that measure cross-peaks well off the diagonal include 2D electronic-vibrational (2D EV) (gray region) and 2D vibrational-electronic (2D VE) (black regions). 2D VE spectroscopy is the subject of this work.

All preceding spectroscopies are sensitive to the detection of signals on or near the diagonal (excitation frequency, ω_1 = detection frequency, ω_3) in a 2D spectrum (Figure 2-1). The large empty areas of the Figure 2-1 spectrum above and below this diagonal correspond to emerging experiments that combine elements from IR and optical spectroscopies. Previous work in these so-called extreme cross-peak corners of the spectrum has been limited to the following: 1D third-order pump-probe techniques with pulse ordering of either optical – IR (transient IR spectroscopy)[34–36] or IR – optical,[37] and a 2D FT 2nd-order experiment in which an optical pulse sequence excites a low-frequency polarization that radiates a mid-IR field.[38] Other 2D techniques, which can be loosely grouped as 5th-order transient 2D IR spectroscopies of both FT and non-FT forms, have various pulse schemes that introduce an optical excitation to a series of mid-IR pulses; however, such a 2D signal of a system approaching equilibrium is still frequency resolved in the mid-IR in both ω_1 and ω_3.[39–44] Recently, Fleming and coworkers introduced a third-order

multidimensional coherent technique combining vibrational (V) and electronic (E) spectroscopies, 2D EV,[45,46] which is depicted by the gray regions in Figure 2-1. These experiments, which have motivated theoretical investigations,[47,48] combine the advantages of 2D IR and 2D ES in a femtosecond technique that is frequency resolved in two distinct spectral regions. 2D EV spectroscopy provides the ability to correlate initial electronic absorptions in a molecule, excited by an optical pump pulse pair, with subsequent nuclear motions, probed by a mid-IR pulse. In this dissertation, I detail our development of another FT spectroscopy that provides insight into the coupling between vibrational and electronic transitions by directly probing these cross-peaks: coherent 2D vibrational-electronic (2D VE) spectroscopy.[49] In 2D VE spectroscopy, two mid-IR pump pulses excite high frequency vibrations, and the subsequent optical probe field is resonant with an electronic transition. Fully resonant 2D VE spectra contain IR and electronic transition dipole moment cross terms.

The one experimental example of VE spectroscopy resonant in both mid-IR and optical fields is the 1D VE femtosecond pump-probe experiment by Tahara et al., in which an excited molecular vibration induces a low-frequency vibrational coherence that is detected through optical probe oscillations.[37] The 2D VE spectroscopy in the present work is sensitive to the coupling between electronic motions and both high- and low-frequency vibrations, and this FT technique provides the excitation frequency resolution to separate the VE spectral signatures of each vibration. The IR-IR-optical pulse ordering in 2D VE spectroscopy[49] has been incorporated in theoretically proposed spectroscopies with two resonant IR fields and either one nonresonant[50] or resonant[51,52] optical pulse; experimental studies with this pulse ordering have been limited to the resonant IR, nonresonant optical fields.[53,54] In the coherent 2D IR spectroscopy (COTIRS) experiment proposed by Park and Cho, two tunable mid-IR pulses excite a vibrational transition to generate

two vibrational coherence states.[50] The integrated scattered field from the subsequent nonresonant optical probe pulse interaction is detected and plotted in a quasi-frequency domain 2D IR spectrum against the two IR excitation frequency axes. A second example of the pulse ordering is the group of doubly vibrationally enhanced (DOVE) four-wave-mixing (FWM) techniques developed by Wright and coworkers to enhance vibrational cross peaks in IR and Raman experiments.[53] The third-order DOVE-FWM technique has also been adapted to IR-IR-visible sum frequency generation (IIV-SFG) experiments to measure vibrations on surfaces.[54] In theorized triply resonant (TR) IIV-SFG experiments, the visible pulse is electronically resonant to obtain vibronic and vibrational couplings of molecules including those dissolved in an isotropic medium.[51] In another theoretical triply resonant experiment, Cho modified COTIRS by replacing the probe with an electronically resonant optical pulse to study linear and quadratic vibronic coupling strengths of molecules in isotropic or anisotropic media.[52] The proposed 2D vibrational spectroscopy by Cho in Ref. 54 is the non-FT precursor to the 2D VE experiments presented in this dissertation.

2.2 Theoretical Background

The pulse sequence in the 2D VE experiments (Figure 2-2(a)) includes electric fields of two mid-IR pump pulses, $\mathbf{E}_1$ and $\mathbf{E}_2$ with wave vectors $\mathbf{k}_1$ and $\mathbf{k}_2$, separated by the vibrational coherence time, τ_1. An optical (near-IR or visible in the current work) probe pulse field, $\mathbf{E}_{pr}$ in the $\mathbf{k}_{pr}$ direction, follows after a waiting time, τ_2. The third-order signal is generated at detection time, τ_3. Experimental delays, τ_n, are with respect to field envelope maxima, t_n; delays, τ_n' , are between successive field-matter interactions and are used in calculating the third-order nonlinear polarization, $\mathbf{P}^{(3)}$ (Figure 2-2(a)):

$$\boldsymbol{P}^{(3)}(\boldsymbol{k}_s, t, \tau_2, \tau_1) = \int_0^\infty \int_0^\infty \int_0^\infty \boldsymbol{R}^{(3)}(\tau_3', \tau_2', \tau_1') \boldsymbol{E}_{pr}\left(\boldsymbol{k}_{pr}, t - \tau_3'\right) \times \tag{2.1}$$

$$\boldsymbol{E}_2(\boldsymbol{k}_2, t + \tau_2 - \tau_3' - \tau_2') \boldsymbol{E}_1(\boldsymbol{k}_1, t + \tau_2 + \tau_1 - \tau_3' - \tau_2' - \tau_1')\, d\tau_1' d\tau_2' d\tau_3'$$

In general, the 2D VE signal can be related to $\mathbf{P}^{(3)}$, which is the convolution of incident fields with the third-order material response function, $\mathbf{R}^{(3)}$:[22,52]

$$\boldsymbol{R}^{(3)}(\tau_3', \tau_2', \tau_1') = \left(\frac{i}{\hbar}\right)^3 \langle [[[M_{eg}(\tau_3' + \tau_2' + \tau_1'), M_{eg}(\tau_2' + \tau_1')], \boldsymbol{M}(\tau_1')], \boldsymbol{M}(0)] \rho_0 \rangle \tag{2.2}$$

where $\mathbf{M}$ is the IR dipole operator, M_{eg} is the electronic dipole operator, ρ_0 is the equilibrium reduced density matrix for the system eigenstates, and the trace $\langle ... \rangle$ is over both the electronic and vibrational state manifolds. Consider a system with two electronic states and one IR-active vibration, which has a different frequency in the ground and excited electronic states. $\mathbf{R}^{(3)}$ comprises responses from several pathways of this system evolving during τ_n' delays following interactions with the three corresponding incident fields. The possible pathways are presented as double-sided Feynman diagrams for the 2D VE signal contributions in both the rephasing (R), $\boldsymbol{k}_{sig} = -\boldsymbol{k}_1 + \boldsymbol{k}_2 + \boldsymbol{k}_{pr}$ (Figure 2-2(b)), and nonrephasing (NR), $\boldsymbol{k}_{sig} = +\boldsymbol{k}_1 - \boldsymbol{k}_2 + \boldsymbol{k}_{pr}$ (Figure 2-2(c)) phase-matched directions. The 2D VE experiments in this work are performed in the pump-probe 2D geometry[55–57] to simplify the phase-matching in this degenerate spectroscopy; therefore, the R and NR signals copropagate with the probe as $\boldsymbol{k}_{sig} = \boldsymbol{k}_1 \pm \boldsymbol{k}_2 + \boldsymbol{k}_{pr} = \boldsymbol{k}_{pr}$, and the fully absorptive 2D signal is detected.[55] Additionally, the probe acts as the local oscillator (LO), as indicated by the common $\mathbf{E}_{\mathrm{pr,LO}}$ field in Figure 2-2(a); as a result, τ_3 is fixed at zero delay.

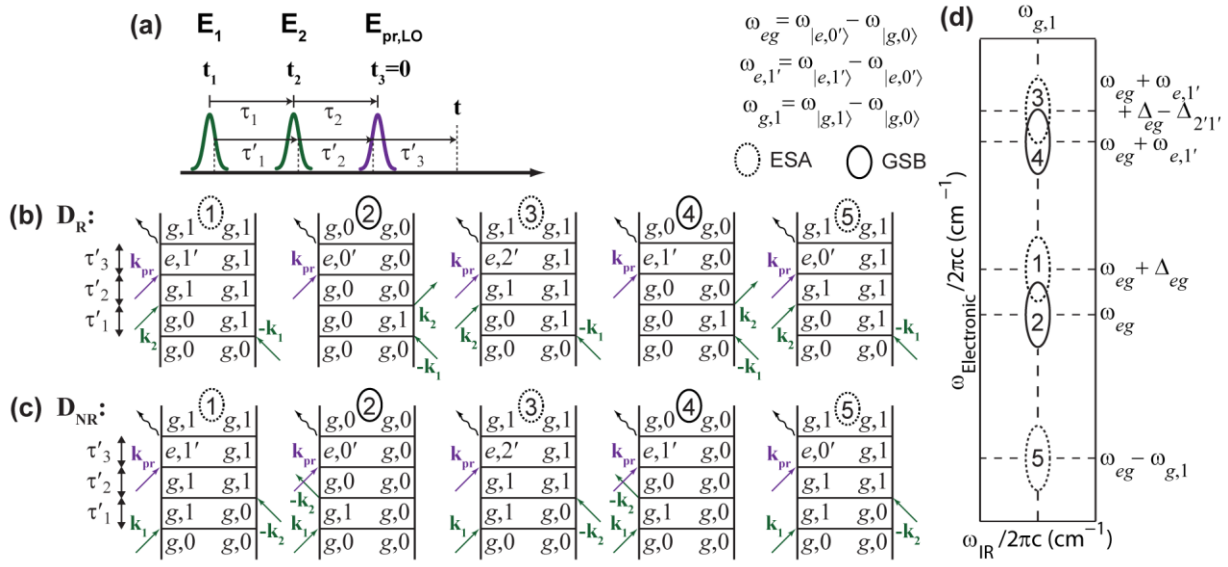

Figure 2-2 2D VE spectroscopy overview. (a) Pulse sequence and time variables. The field-matter interactions within the input pulse envelopes, E_n (mid-IR pump) and E_{pr} (optical probe), radiate a third-order nonlinear polarization, $P^{(3)}$, at t; field-matter interaction delays are $\boldsymbol{\tau'_n}$ with respect to t. The delays, $\boldsymbol{\tau_n}$, are experimentally controlled between envelope centers, t_n, of successive input fields. The probe field serves as the local oscillator (LO) field. (b,c) Double-sided Feynman diagrams that contribute to the 2D VE signal for a model system containing one resonant electronic excited state and one resonant anharmonic vibrational mode: (b) rephasing (R) phase-matched direction diagrams, D_R, (c) nonrephasing (NR) diagrams, D_{NR}. States are denoted as $|N,n\rangle$ where N = g, e are the electronic states and n = 0, 1, 2 (n′ = 0′, 1′, 2′) are the vibrational eigenstates in the electronic ground (excited) state. D_R and D_{NR} are numbered 1-5 for various excited state absorption (ESA, dotted line, negative) signals and ground state bleach (GSB, solid line, positive) signals. (d) The sums of correspondingly numbered D_R and D_{NR} make up peaks 1-5 in a depiction of an absorptive 2D VE spectrum. 2D VE peaks share the vibrational excitation, $\omega_{IR} = \omega_{g,1}$; along the $\omega_{Electronic}$ detection axis, 2D VE peaks have larger line widths and are positioned with respect to the transition frequency, ω_{eg}, between the vibrational ground states $|g,0\rangle$ and $|e,0'\rangle$. The displacements of peaks 1, 3, 4, and 5 from ω_{eg} arise from one or more of the following: probing at $\omega_{eg} \pm 1$ quantum of the vibration; the difference in frequency, Δ_{eg}, of the vibration in the e versus g state; and a vibrational anharmonicity in the e state, $\Delta_{2'1'}$.

In Figure 2-2, each numbered diagram $D_{R,j}$ has a correspondingly numbered $D_{NR,j}$; these pathways sum to form the signal contribution at each numbered peak, j, in the real 2D VE spectrum (Figure 2-2(d)). $D_{R,j}$ and $D_{NR,j}$ for j=[1,3,5] contain the excited state absorption (ESA) negative signals, in which a population exists during τ_2 in the first vibrationally excited state, $|g,1\rangle$ reached via $\omega_{IR} = \omega_{g,1}$ excitation, where $\omega_{g,1}$ is the transition frequency between the lowest two vibrational levels on the electronic ground state. $D_{R,2}$, $D_{R,4}$, $D_{NR,2}$, and $D_{NR,4}$ correspond to ground state bleach (GSB) positive signals, in which a population exists in the ground state, $|g,0\rangle$, after two field interactions (again, $\omega_{IR} = \omega_{g,1}$). In this simplified picture, the optical probe is defined to have a

bandwidth greater than $2\omega_{g,1}$ with a spectral center of $\omega_{\text{Electronic}} = \omega_{eg}$, where ω_{eg} defines the transition frequency between the vibrational ground state of each electronic level, i.e., between $|g,0\rangle$ and $|e,0'\rangle$. The spectrum in Figure 2-2(d) is based on a typical system with vibrational anharmonicity in each electronic state and a difference in frequency, $\Delta_{eg} = \omega_{e,1'} - \omega_{g,1}$, of the IR active vibration between the excited and ground electronic states. For the $|g,n\rangle$ to $|e,n'\rangle$ probe transitions, the ESA peak 1 is shifted from the GSB peak 2 at ω_{eg} by Δ_{eg}. The pair of peaks resulting from $|g,n\rangle$ to $|e,(n+1)'\rangle$ probe transitions are peak 4 at$\left(\omega_{g,1}, \omega_{eg} + \omega_{e,1'}\right)$ and peak 3 shifted from peak 4 by both Δ_{eg} and the vibrational anharmonicity, $\Delta_{2'1'}$, to $\left(\omega_{g,1}, \omega_{eg} + \omega_{e,1'} + \Delta_{eg} - \Delta_{2'1'}\right)$. For $|g,(n+1)\rangle$ to $|e,n'\rangle$ probe transitions, ESA peak 5 is centered at $\left(\omega_{g,1}, \omega_{eg} - \omega_{g,1'}\right)$; no GSB peak exists in this case for a system initially in a vibrational ground state. In this picture, both Δ_{eg} and $\Delta_{2'1'}$ are positive, with $\Delta_{eg} > \Delta_{2'1'}$. The electronic line widths of the 2D VE peaks are expected to be broadened around each quantum of the vibration by features such as low mode combination bands within the vibronic structure. The extent to which the discrete 2D VE peaks are broadened is still being investigated. Furthermore, these combination bands with high- and low-frequency modes could give rise to additional peaks in the 2D VE spectrum. These peaks would be shifted in the ω_{IR} and $\omega_{\text{Electronic}}$ dimensions from the labeled peaks in Figure 2-2(d). For example, one can modify $D_{R,1}$ and $D_{R,2}$ (Figure 2-2(b)) to identify peaks involving a combination mode and their frequency shifts from peaks 1 and 2 (Figure 2-2(d)). Following two IR field interactions at $\omega_{g,1}$, a probe transition from $|g,n\rangle$ to $|e,(n \pm low)'\rangle$ (modified $D_{R,1}$ and $D_{R,2}$) results in $\omega_{\text{Electronic}}$-shifted 2D VE signals. Peaks shifted in ω_{IR} arise from ground state combination modes in one of two ways: 1.) IR excitations at $\omega_{g,(1\pm\text{low})}$ followed by electronic transitions between either$|g,0\rangle$ and $|e,0'\rangle$ (modified $D_{R,2}$) or $|g,1 \pm low\rangle$ and $|e,(1 \pm low)'\rangle$ (modified $D_{R,1}$); 2.) At room temperature, $|g,0 \pm low\rangle$ could be populated if the

frequency of the low mode is ≤ kT, and IR excitations at $\omega_{g,(1\text{-low})}$ precede electronic transitions between either $|g, 0 \pm low\rangle$ and $|e, (0 \pm low)'\rangle$ (modified $D_{R,2}$) or $|g, 1\rangle$ and $|e, 1'\rangle$ (modified $D_{R,1}$). 2D VE spectral peaks shifted in ω_{IR} can also be shifted in $\omega_{Electronic}$ with respect to peaks 1 and 2 (Figure 2-2(d)) by including additional low mode combination bands in the electronic excited state. The relative magnitudes of signals arising from the pathways in Figure 2-2(b) and (c) are expected to be different for each IR-active high frequency vibrational mode or combination band, depending on the specific Franck-Condon factors and non-Condon effects.

The non-FT version of the 2D VE experiment was proposed by Cho where he detailed the molecular interactions deemed important for this new spectroscopy.[52] I will briefly summarize his results, which were developed using a model system consisting of two electronic states (*g*, *e*) and one anharmonic vibrational state. As formulated by Cho, a difference potential between the ground and excited electronic states, δV_{eg}, can describe the strength of vibronic coupling and the fluctuating chromophore-bath interaction potential which induce the electronic dephasing process.[52] Because δV_{eg} is a fluctuating difference potential, it has no zeroth-order term but can be expanded into first-order (linear) and second-order (Duschinsky) vibronic coupling terms $\delta V_{eg}^{(1)}$, and $\delta V_{eg}^{(2)}$, respectively. The $\delta V_{eg}^{(1)}$ terms are largely responsible for describing the extent to which the vibration is displaced when a system undergoes an electronic transition, i.e., the Δ_{eg} term in Figure 2-2(d). However, $\delta V_{eg}^{(2)}$ terms should not be neglected as they are responsible for the Duschinsky rotation effect, which describes the rotation of the vibrational normal coordinates on the electronic excited state and depends quadratically on the vibrational coordinates.[52] In general, nonzero vibronic coupling ($\delta V_{eg} \neq 0$) is required for signals in 2D VE spectra. Additionally, Cho has established three cases to assure signal in his proposed vibronic spectroscopies using a Brownian oscillator model.[52] For 2D VE spectroscopy, at least one of the

following must be fulfilled for a nonzero $\mathbf{R}^{(3)}$: 1.) nonzero $\delta V_{eg}^{(2)}$ and $\mathbf{M}^{(1)}$ (where $\mathbf{M}^{(n)}$ is the *n*th-order spatial derivative from the expansion of **M** over vibrational coordinates); 2.) nonzero $\delta V_{eg}^{(1)}$, $\mathbf{M}^{(1)}$, and $\mathbf{M}^{(2)}$; 3.) nonzero $\delta V_{eg}^{(1)}$, $\mathbf{M}^{(1)}$, and cubic anharmonic potential ($\Delta_{2'1'}$). Future work should explore how $\delta V_{eg}^{(1)}$, $\delta V_{eg}^{(2)}$, $\mathbf{M}^{(1)}$, $\mathbf{M}^{(2)}$ and $\Delta_{2'1'}$ affect the positions, amplitudes and line-shapes of the spectral features in a 2D VE spectrum.

2.3 Experimental Methods

2.3.1 Materials

All starting materials and solvents were purchased from Sigma Aldrich and Alfa Aesar and used without further purification. Steady-state infrared spectra were collected with a JASCO FT/IR-4100 with a spectral resolution of 0.5 cm^{-1}. Steady-state electronic spectra were collected with a JASCO V-630 spectrometer (UV/visible spectra, 0.5 nm spectral resolution) or a Cary 5000 (Agilent) spectrophotometer (near-IR spectra, 1 nm resolution). The mixed valence compound, FeRu, was synthesized according to literature methods,[49,58,59] starting with ~0.6 mmol each of $K_4[Fe(CN)_6]$ and $[RuCl_2(NH_3)_5]Cl_2$ dissolved in 25 mL of H_2O. After heating, filtration, and separation, the product was passed through ion exchange and size exclusion columns. The final sodium form of FeRu in H_2O was dried. A saturated solution of FeRu in formamide (FA) was prepared with a maximum optical density (OD) of 0.4 in the ν_{CN} region (140 μm path length) after solvent subtraction. At $\nu_{max\ MMCT}$ = 8547 cm^{-1} and near $\nu_{max\ near\text{-}IR}$ = 11750 cm^{-1}, the solvent-subtracted electronic absorption spectrum of FeRu in FA (140 μm path length) has OD of 0.85 and ~0.3, respectively. Both $K_4[Fe(CN)_6]$ and $K_3[Fe(CN)_6]\cdot 3H_2O$ samples were used as purchased without further purification. Solutions were prepared of ~30 mM $K_3[Fe(CN)_6]\cdot 3H_2O$ in FA and ~11 mM $K_4[Fe(CN)_6]$ in FA, with solvent-subtracted OD maxima in the ν_{CN} region of 0.34 (140

μm path length) and 0.40 (140 μm path length), respectively. The solvent-subtracted electronic absorption spectrum of $[Fe^{III}(CN)_6]^{3-}$ has a peak OD of 0.47 at $\nu_{\max\ LMCT}$ = 23585 cm^{-1} and an OD of ~0.4 near $\nu_{\max\ visible}$ = 24750 cm^{-1} (140 μm path length).

2.3.2 The 2D VE Spectrometer

The output from a commercial Spectra Physics Spitfire Pro 35F-XP regenerative amplifier operating at 1 kHz (800 nm, 35 fs, 2.5 W) is used to generate the pulses in this experiment. The 2D VE experimental layout is shown in Figure 2-3. To create the mid-IR pump pulses, one third of the amplified 800 nm light pumps a dual-pass optical parametric amplifier (OPA-800C, Newport), which yields short-wave IR signal and idler pulses. These pulses are then spatially and temporally overlapped in a 0.5-mm thick $AgGaS_2$ crystal; a difference frequency mixing process generates tunable mid-IR pulses. For this application, the pulse spectra are centered at $\nu_{\max\ mid\text{-}IR}$ ≈ 2050 cm^{-1} ($\lambda_{\max\ mid\text{-}IR}$ ≈ 4.88 μm) with a full width at half maximum (FWHM) of $\Delta\nu_{mid\text{-}IR}$ = 300 cm^{-1}. The mid-IR radiation is vertically polarized as it enters a Mach-Zehnder interferometer with two matched 50:50 ZnSe beam splitters (Rocky Mountain Instrument Co.); the pulse pairs from the bright output (symmetric interferometer paths, each with one beam splitter transmission and one reflection) serve as the vibrational pump pulses in the experiment. Within the interferometer, each beam path includes a gold-coated cubic retroreflector mounted to a computer-controlled translation stage (XMS50, Newport). These stages are used for precise control of the temporal positions of pump pulses, t_1 and t_2, which are related to the vibrational coherence time by $\tau_1 = t_2 - t_1$. For the single-pump, 1D VE experiments presented in this work, the second arm of the Mach-Zehnder is blocked, and the t_1 stage is used to scan the pump with respect to a fixed electronic probe. A chopper in the pump path modulates either the single IR pump (1D VE) or the collinear pump pair (2D VE) at 500 Hz to enable collection of alternate shots of the LO intensity, I_{LO}, with

and without the third-order signal field with a CCD spectrograph. The mid-IR pump pulses are routed toward and focused at the sample (0.4 μJ each, $1/e^2$ spot size of 180 μm) by a 150-mm focal length CaF_2 lens. The pulses are ~70 fs in duration as determined by field and interferometric autocorrelation measurements. After the sample, the mid-IR pump pulses are routed and collimated for infrared integrated or spectral detection to determine the τ_1 delay or detect transient IR signals in the complementary experiment discussed in Section 2.3.3. Spectrally resolved infrared detection uses direct coupling into a 0.190 m Czerny-Turner spectrometer (Triax 190, Horiba Jobin Yvon, 75 groove/mm grating blazed at 4 μm) and a 2 × 32 mercury cadmium telluride (MCT) array detector and integrator (FPAS-6416, Infrared Systems Development).

A smaller portion of the Ti:Sapphire amplifier output passes through a computer-controlled delay stage (ILS150CC, Newport) to control the time delay, τ_2, between the second IR pulse and the probe. For the experiments presented here, the probe is either a near-IR continuum or the second harmonic of the Ti:Sapphire fundamental. 1D VE and 2D VE spectroscopies of a given molecule have identical probe characteristics. Switching spectral regions of the probe necessitates minor changes to the optical path such as exchanging between nonlinear crystals and between antireflection-coated lenses. To generate the white light continuum, ~500 nJ of 800 nm light is focused in a 3-mm thick sapphire window. Compression with a pair of fused silica prisms and spectral filtering of the continuum with an 850-nm longpass filter yield a transform-limited near-IR probe with $\nu_{\text{max near-IR}}$ = 11750 cm^{-1} ($\lambda_{\text{max near-IR}}$ = 851 nm), $\Delta\nu_{\text{near-IR}} \approx 400$ cm^{-1}, and pulse durations of 35 fs as measured by intensity autocorrelation in a 50-μm thick Type I BBO crystal.

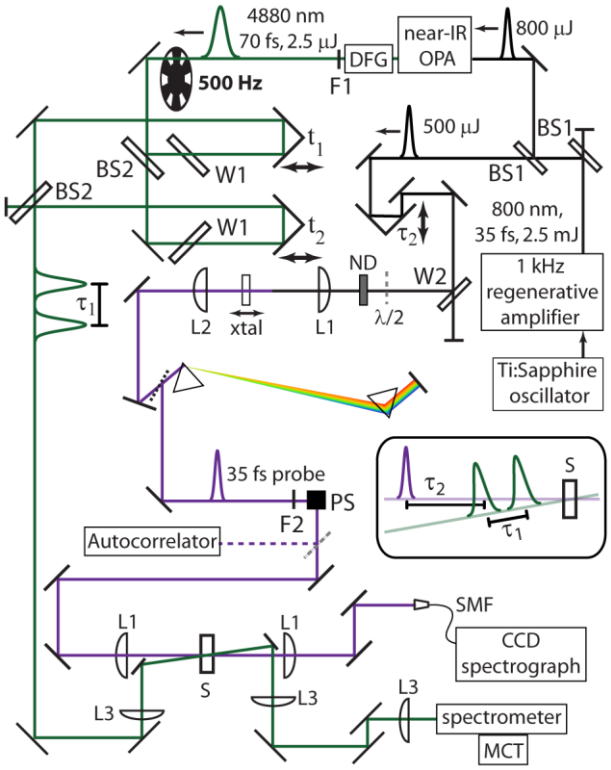

Figure 2-3 Experimental setup. Pulses are generated from 1 kHz regeneratively amplified 800 nm light. A mid-IR pulse train formed via difference frequency generation (DFG) of the optical parametric amplifier (OPA) outputs is chopped at 500 Hz and enters a Mach-Zehnder interferometer that has computer-controlled translation stages in each path to define pulse time positions t_1 and t_2. Collinear pump pulse pairs separated by delay $\tau_1 = t_2 - t_1$ precede the probe pulse by a computer-controlled delay τ_2. Near-IR probe: 800 nm light is reflected from a window (W2), attenuated with a neutral density (ND) filter, and < 1 μJ is focused onto a 3 mm sapphire window (xtal). 400 nm probe: a mirror replaces W2, a λ/2-plate is inserted prior to the ND filter, and a 100-μm thick type I BBO (xtal) just behind the focus replaces the sapphire. Each probe is prism-compressed and spectrally filtered from 800 nm (additional 850 nm longpass filter, F2, for near-IR), before passing through a periscope (PS). At the sample, S, all pulses have vertical polarization, and lenses are used to focus the intersecting beams. The third-order signals and probe copropagate and are detected with a CCD spectrograph. After the sample, IR pulses are routed to a spectrometer and mercury cadmium telluride (MCT) detector. W1: ZnSe window, W2: fused silica (FS) window, BS1: 800 nm dielectric beam splitter, BS2: 50:50 ZnSe beam splitter, F1: Ge filter, L1: FS (near-IR AR coated) or BK7 (400 nm AR coated) plano-convex (PC) lens, *f*=100 mm, L2: FS (near-IR) or BK7 (400 nm) PC lens, *f*=50 mm, L3: CaF_2 PC lens, *f*=150 mm. Silver (probe path) and gold (pump path) mirrors are unlabeled.

At the sample, each near-IR probe pulse is ~10 nJ in energy. The probe centered at $\nu_{\text{max visible}}$ = 24750 cm^{-1} ($\lambda_{\text{max visible}}$ = 404 nm) with $\Delta\nu_{\text{visible}} \approx 400$ cm^{-1} is created with the flexibility to use it also as a pump (maximum 300 nJ/pulse at the sample for pump, ~30 nJ/pulse for probe) in corresponding transient IR experiments, as discussed in Section 2.3.3. The Ti:Sapphire fundamental passes through a half-wave plate and neutral density filter before being focused just

before a 100-μm thick Type I BBO crystal. The blue light is spatially filtered from the fundamental in a shortened prism compressor optimized for minimizing the duration of the cross-correlation with a mid-IR pump pulse. The polarization of each electronic probe is rotated via periscope to match the vertically polarized mid-IR pump. Each type of probe is focused to a 100 μm $1/e^2$ spot size at the sample by a 100 mm focal length lens. After the sample, the probe (LO) and third-order signals are routed and collimated for integrated or spectral detection. All optical spectral detection in 1D VE and 2D VE experiments involves the coupling of the signal and LO through a microscope objective (Newport M-10X) into a single-mode fiber (ThorLabs 780HP or S405-XP). The output of the fiber is fed into a 0.303 m Czerny-Turner spectrometer (Andor Shamrock SR-303i, 600 groove/mm grating blazed at 800 nm or 1200 groove/mm grated blazed at 300 nm, f/4 optics) and a 200 × 1600 pixel, fan cooled (-80° C), front-illuminated CCD array (Andor DU970P-UV). The light is contained in the top 20 (out of 200) pixel rows, which are vertically binned in 0.8 ms to satisfy 1 kHz single-shot data collection. Resonant and nonresonant third-order 2D VE signals are found to depend linearly on IR pump power. For a given experimental time step in 1D VE or 2D VE experiments, the intensity difference ($I_{\text{pump on}} - I_{\text{pump off}}$) between adjacent background-subtracted shots is calculated in LabVIEW for 2000 total shots and averaged. In all 1D VE and 2D VE experiments, the sample cell consists of two 1-mm thick CaF_2 windows separated by a 140 μm Teflon spacer. The sample can be held static or flowed in this sample cell, which is translated perpendicularly to the beam propagation direction to prevent photodamage.

Spatial and temporal overlap between the pump and probe can be found using a number of methods. For convenience, a 100-μm thick Type I BBO crystal following a 1 mm CaF_2 sample window was initially used as phase-matching can be achieved for upconversion of a λ = 5 μm pump with either optical probe. Although this provides a robust visual indicator of overlap

between IR and weak electronic pulses, the absorption of BBO between 2000 and 2100 cm^{-1} complicates and broadens the temporal profile of the cross correlation. Substitution of the BBO crystal for a thin, transparent lithium niobate crystal improves the mid-IR bandwidth that is phase-matched with the near-IR probe but greatly reduces the mid-IR bandwidth that is phase-matched for 400 nm upconversion. Given the phase-matching and absorption limitations in crystals and the need to characterize the instrument and solvent response (see Section 2.4), it is still possible to characterize the temporal overlap by detecting the nonresonant integrated 1D VE solvent signal from the sample cell as a function of delay, τ_2, with a photodiode (silicon for near-IR probe, gallium phosphide for visible probe). Whether or not a solute is present, the signal for pulse overlap characterization near $\tau_2 = 0$ and for assignment of $\tau_2 = 0$ in 1D VE and 2D VE scans is dominated by the solvent response. For the experiments shown here, the temporal response in the sample under extreme phase-matching conditions is 180 fs FWHM.

2.3.3 Data Processing

For a 2D VE spectrum at a given τ_2 delay, the second mid-IR pump is defined to be at $-\tau_2$ delay with respect to the probe pulse ($t_3 = 0$, Figure 2-2(a)). A symmetric scan with respect to $\tau_1 = 0$ (or $t_1 = t_2 = -\tau_2$) is collected in two halves in the following manner. For $t_2 = -\tau_2$, t_1 is scanned over [$-\tau_2 - 2100$ fs, $-\tau_2 - 20$ fs] in 4 fs steps and [$-\tau_2 - 20$ fs, $-\tau_2 + \delta$ fs] in 1 fs steps, for positive τ_1 delays. Then, while t_1 is held fixed at $-\tau_2$, t_2 is scanned in the same manner, producing negative τ_1 delays. Each of these half scans samples a small delay of δ fs beyond $-\tau_2$ to provide extra points for finding $\tau_1 = 0$ in case of an initial time assignment error, stage motion error, or other experiment drift. For each half of a 2D VE scan, the time-domain interferences of selected pixels of 2D VE raw data are compared to the integrated IR interference to find the $\tau_1 = 0$ point to the nearest 1 fs step and verify that the $\tau_1 = 0$ position maintains the same τ_2 delay, as reported by stage positions. If the delay of

pulse 1 or 2 differs from the established τ_2 position, then $\tau_1 = 0$ for $t_1 \neq t_2$, and the resulting 2D VE spectrum would be a mixture of 2D VE τ_2 spectra. Preventing these errors is most important at short waiting times. Multiple scans are collected at each τ_2 for averaging, depending on the signal-to-noise level of the data. After averaging, two complementary half scans are stitched together using the necessary and unique points ($\tau_1 = 0$ from one half scan only) to create a [-2100 fs, 2100 fs] range of data with a combination of ~1 fs and ~4 fs steps, as reported by stage position. Interpolation with a cubic spline results in time-domain 2D VE data over a range of [-2048 fs, 2048 fs] with even steps of 4 fs; multiplication of the data by the Jacobian[60,61] then transforms from wavelength to frequency in the detection dimension.

Given the subtraction of I_{LO} from the copropagating signal and LO fields in LabVIEW (Section 2.3.2), the time-domain 2D VE data (Figure 2-4(a)) are now of the form:

$$I_{raw}^{(3)}(\omega_3, \tau_1, \tau_2) = \left|\hat{E}_{LO}(\omega_3) + \hat{E}_{2D}^{(3)}(\omega_3, \tau_1, \tau_2) + \hat{E}_{PP}^{(3)}(\omega_3, \tau_2) + \ldots \right. \tag{2.3}$$

$$\left. \ldots \hat{E}_{PP}^{(3)}(\omega_3, |\tau_1| + \tau_2)\right|^2 - I_{LO}(\omega_3)$$

Slices of 2D VE data for individual ω_3 values corresponding to CCD pixels are plotted in Figure 2-4(b) and (c). In addition to the $\hat{E}_{2D}^{(3)}(\omega_3, \tau_1, \tau_2)$ signal from one interaction with each of the three pulses, third-order pump-probe signal fields exist from two interactions each with either the stationary, $\hat{E}_{PP}^{(3)}(\omega_3, \tau_2)$, or scanning, $\hat{E}_{PP}^{(3)}(\omega_3, |\tau_1| + \tau_2)$, pump. The τ_1-independent pump-probe signal dictates the nonzero baseline most evident in Figure 2-4(c), while the τ_1-dependent pump-probe signal is responsible for the envelope that is asymmetric in intensity about this baseline offset. Because $\hat{E}_{LO}(\omega_3) >> \hat{E}^{(3)}(\omega_3)$, where all third-order fields are grouped as $\hat{E}^{(3)}(\omega_3)$, the detected third-order intensities are negligible, which leaves only $\hat{E}_{LO}(\omega_3)$ and

$\hat{E}^{(3)}(\omega_3)$ cross products. The τ_1-independent pump-probe signal can be approximated from $I_{raw}^{(3)}(\omega_3, \tau_1, \tau_2)$ at large $|\tau_1|$ for subtraction, but the removal of $\hat{E}_{PP}^{(3)}(\omega_3, |\tau_1| + \tau_2)$ requires a fit to the data. Alternately, chopping each mid-IR pump would enable the separate determination of each pump-probe field for direct subtraction. Only$\hat{E}_{PP}^{(3)}(\omega_3, \tau_2)$ is subtracted before performing the FT. Given the underlying shape of $\hat{E}_{PP}^{(3)}(\omega_3, |\tau_1| + \tau_2)$ at the τ_1 values sampled in this work, this FT has no ringing in ω_1 due to derivative discontinuities in τ_1. In future investigations of 2D VE signals at directly excited low-frequency modes, complete removal of non-interfering terms in τ_1 may be necessary to distinguish features near $\omega_1 = 0$.

After subtraction of the $\hat{E}_{PP}^{(3)}(\omega_3, \tau_2)$ contribution from Equation 2.3, a hyperbolic tangent apodization function is applied to the resulting data for smooth decay to zero at large $|\tau_1|$. Finally, the FT with respect to τ_1 results in the isolation of the interference term and a 2D VE spectrum (Figure 2-4(d) and (e)) in the mid-IR ω_1 and electronic ω_3 spectral regions:

$$\hat{S}_{2D}^{raw}(\omega_3, \omega_1, \tau_2) = \hat{E}_{2D}^{(3)}(\omega_3, \omega_1, \tau_2)\hat{E}_{LO}^{*}(\omega_3) + c.c. \tag{2.4}$$

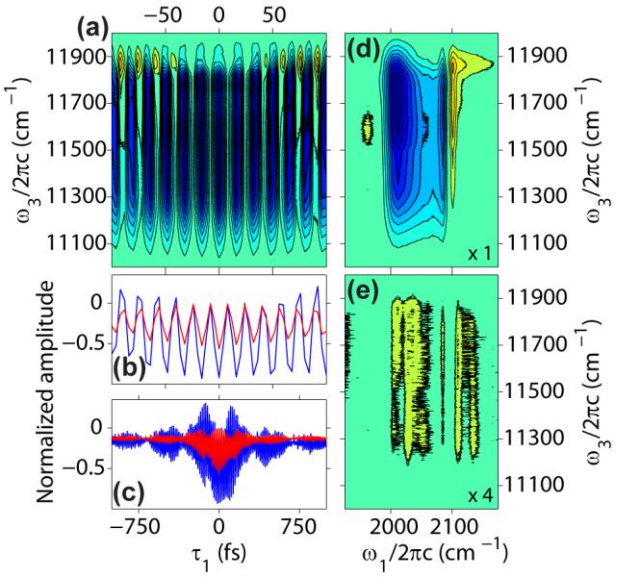

Figure 2-4 Application of the Fourier transform (FT) on 2D vibrational-electronic (VE) spectroscopy time-domain data. (a-c) Averaged 2D VE data (τ_2 = 50 fs) of $[(CN)_5Fe^{II}CNRu^{III}(NH_3)_5]^-$ (FeRu) dissolved in formamide after subtraction of an average baseline dominated by the τ_2 = 50 fs single-pump third-order signals. Over the τ_1 range [-100 fs, 100 fs], the spectrally resolved (a) and individual ω_3 pixel slices (b) at 11200 cm^{-1} (red line) and 11800 cm^{-1} (blue line) are nearly symmetric about $\tau_1 = 0$. (c) The beat pattern evident over a larger portion of a τ_1 scan indicates narrow absorptions in ω_1; frequency resolving these absorptions dictates the τ_1 scanning range. (d) Real (absorptive) part of 2D VE spectrum obtained by FT of (a) with strong negative peaks at FeRu cyanide stretching modes and a narrow positive signal near 2100 cm^{-1} that is not apparent in (a) across the majority of the ω_3 axis. (e) Imaginary part of FT spectrum with signal magnitude ≤ 5% of the real spectrum maximum with no phase correction. (a, d, e) Contour lines are at the following positions: ±0.1, ±0.2, ±0.3, ±0.4, ±0.5, ±0.6, ±0.7, ±0.8, ±0.9, and ±1.0.

In this work, the 2D VE data is presented as the cross product in Equation 2.4 without division by the LO field to avoid the introduction of noise, as the third-order signal extends out to the wings of the probe spectrum in ω_3. The signal field, $\hat{E}_{2D}^{(3)}(\omega_3, \omega_1, \tau_2)$, appears to have a nearly constant magnitude across the LO spectrum and an electronic line width that is not contained within the LO bandwidth for experiments to this point. The FT of the time-domain amplitude-modulated 2D VE signal centered at $\tau_1 = 0$ yields a nominally fully real (absorptive) 2D spectrum.[55] Deviation from this spectrum, i.e., imaginary 2D VE amplitude, could result from a spectral phase difference, $\Delta\phi_{12}(\omega_1) = \phi_2(\omega_1) - \phi_1(\omega_1)$, between the two pump pulses. The phase differences are considered only in ω_1 because of the intrinsic heterodyne detection of the signal with the probe field, a simplification of the pump-probe geometry that has been noted in 2D IR and 2D ES

studies.[13,55,56,62,63] The Mach-Zehnder interferometer that creates the pump pulse pairs is found to have a $\Delta\phi_{12}(\omega_1)$ that is nearly linear with a slope of $\omega_1 \tau_1$. Therefore, the extent of the imaginary part of the 2D VE FT signal corresponds to the difference between the experimentally determined and true $\tau_1 = 0$ values. Figure 2-4(e) shows the imaginary part of a 2D VE spectrum normalized to the real part in Figure 2-4(d) and then multiplied by 4. The maximum magnitude of the imaginary part is ~5% of that of the real part. In each half scan, $\tau_1 = 0$ is found to the nearest 1 fs. One strategy to account for the small $\tau_1 = 0$ displacement is to apply a phase correction to the FT of each individual scan and average the 2D spectra. However, the low signal-to-noise ratios of individual scans introduce large errors into phase corrections; furthermore, the experimental $\tau_1 = 0$ differs slightly for each half scan due to stepping variations, so a complete scan could not be phase corrected by a single factor. Given stage motion and readout errors, the average of several time-domain scans each with ~1 fs precision ensures that their center points fall within ±0.5 fs of the true $\tau_1 = 0$. This averaging strategy results in high signal-to-noise ratios of time-domain data with τ_1 determined to the nearest ~1/16 of a mid-IR cycle. A single phase correction applied to the FT of this data would not accurately account for the phase shifts from individual scans. Therefore, no phase shift is applied, $\hat{S}_{2D}^{final}(\omega_3, \omega_1, \tau_2) = \hat{S}_{2D}^{raw}(\omega_3, \omega_1, \tau_2)$, the time-centering artifact that makes up the imaginary FT component is considered negligible, and the real component of the FT is presented as the 2D VE spectrum.

2.4 Resonant and Nonresonant 2D VE Spectroscopic Signals

The 2D VE technique is sensitive to nonresonant signal contributions, notably from solvent and glass, in addition to fully resonant signals. As in the resonant case (Eq. (1) and (2)), the nonresonant 2D VE signal can also be related to $\mathbf{P}^{(3)}$ and $\mathbf{R}^{(3)}$. However, when the electronic probe

is nonresonant, the Raman excitation interaction and stimulated signal are time-coincident based on the assumption of short lifetime in a Raman virtual state, i.e., $\tau_3' = 0$. The components of $\boldsymbol{P}^{(3)}_{nonres}$ and $\boldsymbol{R}^{(3)}_{nonres}$ corresponding to nonresonant 2D VE signals are as follows:[50,64]

$$\boldsymbol{P}^{(3)}_{nonres}(\boldsymbol{k}_s, t, \tau_2, \tau_1) = \boldsymbol{E}_{pr}(\boldsymbol{k}_{pr}, t) \int_0^\infty \int_0^\infty \boldsymbol{R}^{(3)}_{nonres}(\tau_2', \tau_1')\, \boldsymbol{E}_2(\boldsymbol{k}_2, t + \tau_2 - \tau_2') \times \ldots \tag{2.5}$$

$$\boldsymbol{E}_1(\boldsymbol{k}_1, t + \tau_2 + \tau_1 - \tau_2' - \tau_1') d\tau_1' d\tau_2'$$

$$\boldsymbol{R}^{(3)}_{nonres}(\tau_2', \tau_1') = -\left(\frac{1}{\hbar^2}\right) \langle \big[[\alpha(\tau_2' + \tau_1'), \boldsymbol{M}(\tau_1')], \boldsymbol{M}(0)\big] \rho_0 \rangle \tag{2.6}$$

where α is the polarizability and **M** and ρ_0 are defined as in Equation 2.2. The polarization can be expanded into terms based on phase with respect to the probe field. A general form of the expansion of $\mathbf{P}^{(3)}$ in Eq. (2.1) or (2.5) is given by[64]

$$\boldsymbol{P}^{(3)}(\boldsymbol{k}_s, t, \tau_2, \tau_1) = 2\mathbb{R}\big[\boldsymbol{P}^{(3)}(\boldsymbol{k}_s, t, \tau_2, \tau_1)\big] \cos(\omega t) + 2\mathbb{I}\big[\boldsymbol{P}^{(3)}(\boldsymbol{k}_s, t, \tau_2, \tau_1)\big] \sin(\omega t) \tag{2.7}$$

Each third-order signal (resonant and nonresonant) radiated in the $\boldsymbol{k}_{sig} = \boldsymbol{k}_1 \pm \boldsymbol{k}_2 + \boldsymbol{k}_{pr} = \boldsymbol{k}_{LO}$ direction has a phase shifted by π/2 from the polarization:

$$\begin{aligned} \boldsymbol{E}^{(3)}_{2D}(\boldsymbol{k}_s, t, \tau_2, \tau_1) &\propto i\boldsymbol{P}^{(3)}(\boldsymbol{k}_s, t, \tau_2, \tau_1) \\ &= 2\mathbb{R}\big[\boldsymbol{P}^{(3)}(\boldsymbol{k}_s, t, \tau_2, \tau_1)\big] \sin(\omega t) + 2\,\mathbb{I}\big[\boldsymbol{P}^{(3)}(\boldsymbol{k}_s, t, \tau_2, \tau_1)\big] \cos(\omega t) \\ &= \boldsymbol{E}^{birefringent}_{2D}(\boldsymbol{k}_s, t, \tau_2, \tau_1) \sin(\omega t) + \boldsymbol{E}^{dichroic}_{2D}(\boldsymbol{k}_s, t, \tau_2, \tau_1) \cos(\omega t) \end{aligned} \tag{2.8}$$

The imaginary, or dichroic, part of the polarization measures a change of absorption in the sample and oscillates in phase with the LO ($\Delta\phi_{LO} = 0$). The real, or birefringent, part of the

polarization measures a change in the real part of the refractive index in the sample and oscillates out of phase with the LO ($\Delta\phi_{LO} = \pi/2$).

The dominant signal components in a 2D VE spectroscopy experiment are the following: 1) the dichroic signal from fields resonant with vibrational and electronic transitions in the sample; 2) a birefringent signal from the resonant IR pumps and nonresonant electronic probe interaction in solvent; 3) a birefringent signal from the interaction of all three nonresonant incident fields in the CaF_2 sample cell windows. The detection sensitivity of each of these signals is dependent on experimental parameters. The pump-probe 2D geometry provides intrinsic heterodyne detection of $E_{2D}^{(3)}$ with the fixed in-phase probe (LO) field, and this lack of LO phase control should preclude the measurement of the large birefringent signal components in quadrature. However, nonresonant dichroic signals have been reported in nonlinear spectroscopies, with spectral signatures that correspond to the extent to which the incident pulses are transform limited.[65,66] Resonant spectroscopies in the pump-probe geometry have exhibited solvent or neat liquid signals, especially at early time delays, that are included in the instrument response.[33,37] In their 1D VE experiment, Tahara et al. attribute this signal to the Raman-induced Kerr effect,[67] in which excited solvent vibrations cause a temporal change in the sample refractive index and induce phase modulations.[37] Collinear or pump-probe geometry nonresonant techniques such as Z-scan,[68] spatially masked optical Kerr effect (SM-OKE),[69] position-sensitive Kerr lens spectroscopy (PSKLS),[70] and apertured optical heterodyne detected (OHD) OKE[71] have been used in different applications to simplify the experimental determination of the full nonlinear susceptibility. In these experiments, the nonlinear complex signals have polarization amplitudes with spatial variations, which are sensitive to both sample position and insertion of beam stops such as apertures or slits between the sample and detector. Adapting the expression from Gardecki, et al.

from a pump-probe OHD OKE experiment to a 2D experiment, the expression for the measured heterodyne detected signal is given here as a function of post-sample aperture radius, r_a, and sample displacement, z, from the focal spot size (w) of the beams:[71]

$$\boldsymbol{S}_{2D}^{(3)}(\boldsymbol{k}_s, r_a, z, \tau_2, \tau_1) = \frac{2w_{0,LO}w_{0,sig}kL}{w_{LO}w_{sig}\left[1+\frac{z^2}{z_0^2}\right]^2}\int_0^{r_a} \exp\left[-r^2\left(\frac{1}{w_{LO}^2}+\frac{1}{w_{sig}^2}\right)\right]\ldots \tag{2.9}$$

$$\times\left\{\sin\left(\Delta\theta_{LO}(r,z)\right)\boldsymbol{S}_{2D}^{birefringent}(\boldsymbol{k}_s,\tau_2,\tau_1)+\cos\left(\Delta\theta_{LO}(r,z)\right)\boldsymbol{S}_{2D}^{dichroic}(\boldsymbol{k}_s,\tau_2,\tau_1)\right\}rdr$$

In this expression, $w_{0,LO}=\sqrt{3}w_{0,sig}=w\sqrt{1+z^2/z_o^2}$ defines spot sizes at the sample, where $z_0=kw^2/2$ is the Rayleigh range, $k=2\pi/\lambda$, and the factor of $\sqrt{3}$ arises from the creation of the third-order polarization by three incident light fields. The terms $w_{LO}=w_{0,LO}\sqrt{g^2+d^2/d_{LO}^2}$ and $w_{sig}=w_{0,sig}\sqrt{g^2+d^2/d_{LO}^2}$ are the beam radii at the aperture, d is the distance between the sample of length L and the aperture, $d_{LO}=kw_{0,LO}^2/2$, $d_{sig}=kw_{0,sig}^2/2$, $g=1+d/R_{LO}(z)$, and the radius of curvature is $R_{LO}(z)=z(1+z^2/z_o^2)$. The spot size difference between the signal and LO causes a phase difference, θ_{LO}, that varies radially at finite distances from the sample:

$$\Delta\theta_{LO}(r,z)=\left(\theta_{sig}-\theta_{LO}\right)-\frac{kr^2}{2}\left(\frac{1}{R_{sig}}-\frac{1}{R_{LO}}\right) \tag{2.10}$$

where $\theta_{LO}=\tan^{-1}\left[\frac{d}{gd_{LO}}\right]$, $\theta_{sig}=\tan^{-1}\left[\frac{d}{gd_{sig}}\right]$, $R_{LO}=d\left[1-\frac{g}{g^2+d^2/d_{LO}^2}\right]^{-1}$, and $R_{sig}=d\left[1-\frac{g}{g^2+d^2/d_{sig}^2}\right]^{-1}$. Specifically, the magnitudes of birefringent signals detected with an in-phase LO increase with sample displacement from the beam waist and insertion of apertures in the post-sample beam.[68,71]

Beam apertures and sample z-position are explored in the 2D VE experiments presented here. The coupling into <5 μm diameter single-mode optical fibers via a microscope objective serves as a spatial mask for the signal and LO, which have different spatial and divergence properties. The experiment is also found to be equally sensitive to nonresonant signals with free-space coupling through a spectrometer entrance slit. With fiber entrance or slit apertures, the strengths and signs of the nonresonant signals depend strongly on the LO (and thus signal) beam steering. Careful alignment into the optical fiber is performed for optimal LO and resonant VE signals, which are narrow in ω_1 and can be distinguished from broad nonresonant signals via the FT of preliminary 2D scans at $\tau_2 > 0$. Given the z-position dependence of birefringent signals, it is important to explore the placement of the sample with respect to the intersection of IR and optical beam waists. Spectrally resolved or diode-integrated VE signals are dominated near $\tau_2 = 0$ by nonresonant response from the solvent or 1-mm thick CaF_2 sample windows over several millimeters of z-dimension translation. To find a z-position near the center of the 140 μm thick sample, transient IR spectroscopy, which reverses the roles of the pump and probe is a useful tool. A chopper inserted into the optical path modulates the ≤300 nJ visible or ~10 nJ near-IR pump pulse at 500 Hz, and a single unchopped mid-IR pulse (~0.4 μJ) serves as the probe and eventual LO. Transient IR spectra at and near $\tau_2 = 0$ are collected on the MCT detector to find a z-position at roughly maximum signal. Iterative beam steering and sample position adjustments are made to optimize the signal and match it to previously reported transient IR traces for both $[Fe^{III}(CN)_6]^{3-}$ and FeRu.[35,72] The roles of the mid-IR and optical pulses are then switched back to the original VE spectroscopy scheme. Final integrated time-domain interferograms and 1D VE spectra, generally with a slight reduction in nonresonant signal, are collected to refine stage settings corresponding to pulse overlap, as described earlier.

The experimental setup described in this chapter is the basis for all 2D VE experiments to date although modifications have been made it increase the speed and sensitivity (Chapter 4) as well as the addition of polarization to study orientation dependence (Chapter 5). The data presented throughout this dissertation will be collected in the manner described here unless a modification has been explicitly outlined within the individual chapter.

References

(1) Hybl, J. D.; Albrecht, A. W.; Gallagher Faeder, S. M.; Jonas, D. M. Two-Dimensional Electronic Spectroscopy. *Chem. Phys. Lett.* **1998**, *297*, 307–313.

(2) Tian, P. F.; Keusters, D.; Suzaki, Y.; Warren, W. S. Femtosecond Phase-Coherent Two-Dimensional Spectroscopy. *Science (80-.).* **2003**, *300* (5625), 1553–1555.

(3) Borca, C. N.; Zhang, T. H.; Li, X. Q.; Cundiff, S. T. Optical Two-Dimensional Fourier Transform Spectroscopy of Semiconductors. *Chem. Phys. Lett.* **2005**, *416* (4–6), 311–315.

(4) Vaughan, J. C.; Hornung, T.; Stone, K. W.; Nelson, K. A. Coherently Controlled Ultrafast Four-Wave Mixing Spectroscopy. *J. Phys. Chem. A* **2007**, *111* (23), 4873–4883.

(5) Grumstrup, E. M.; Shim, S.-H.; Montgomery, M. a; Damrauer, N. H.; Zanni, M. T. Facile Collection of Two-Dimensional Electronic Spectra Using Femtosecond Pulse-Shaping Technology. *Opt. Express* **2007**, *15* (25), 16681–16689.

(6) Cowan, M. L.; Ogilvie, J. P.; Miller, R. J. D. Two-Dimensional Spectroscopy Using Diffractive Optics Based Phased-Locked Photon Echoes. *Chem. Phys. Lett.* **2004**, *386* (1–3), 184–189.

(7) Brixner, T.; Stiopkin, I. V.; Fleming, G. R. Tunable Two-Dimensional Femtosecond Spectroscopy. *Opt. Lett.* **2004**, *29* (8), 884–886.

(8) Myers, J. A.; Lewis, K. L. M.; Tekavec, P. F.; Ogilvie, J. P. Two-Color Two-Dimensional Fourier Transform Electronic Spectroscopy with a Pulse-Shaper. *Opt. Express* **2008**, *16* (22), 17420–17428.

(9) Tekavec, P. E.; Myers, J. A.; Lewis, K. L. M.; Ogilvie, J. P. Two-Dimensional Electronic Spectroscopy with a Continuum Probe. *Opt. Lett.* **2009**, *34* (9), 1390–1392.

(10) Turner, D. B.; Hassan, Y.; Scholes, G. D. Exciton Superposition States in CdSe Nanocrystals Measured Using Broadband Two-Dimensional Electronic Spectroscopy. *NANO Lett.* **2012**, *12* (2), 880–886.

(11) Spokoyny, B.; Harel, E. Mapping the Vibronic Structure of a Molecule by Few-Cycle Continuum Two-Dimensional Spectroscopy in a Single Pulse. *J. Phys. Chem. Lett.* **2014**, *5* (16), 2808–2814.

(12) Brida, D.; Manzoni, C.; Cerullo, G. Phase-Locked Pulses for Two-Dimensional Spectroscopy by a Birefringent Delay Line. *Opt. Lett.* **2012**, *37* (15), 3027–3029.

(13) Courtney, T. L.; Park, S. D.; Hill, R. J.; Cho, B.; Jonas, D. M. Enhanced Interferometric Detection in Two-Dimensional Spectroscopy with a Sagnac Interferometer. *Opt. Lett.* **2014**, *39* (3).

(14) Mehlenbacher, R. D.; McDonough, T. J.; Grechko, M.; Wu, M.-Y.; Arnold, M. S.; Zanni, M. T. Energy Transfer Pathways in Semiconducting Carbon Nanotubes Revealed Using Two-Dimensional White-Light Spectroscopy. *Nat. Commun.* **2015**, *6*.

(15) Moran, A. M.; Maddox, J. B.; Hong, J. W.; Kim, J.; Nome, R. A.; Bazan, G. C.; Mukamel, S.; Scherer, N. F. Optical Coherence and Theoretical Study of the Excitation Dynamics of a Highly Symmetric Cyclophane-Linked Oligophenylenevinylene Dimer. *J. Chem. Phys.* **2006**, *124* (19).

(16) Tseng, C.; Matsika, S.; Weinacht, T. C. Two-Dimensional Ultrafast Fourier Transform Spectroscopy in the Deep Ultraviolet. *Opt. Express* **2009**, *17* (21), 18788–18793.

(17) Selig, U.; Schleussner, C.-F.; Foerster, M.; Langhojer, F.; Nuernberger, P.; Brixner, T. Coherent Two-Dimensional Ultraviolet Spectroscopy in Fully Noncollinear Geometry. *Opt. Lett.* **2010**, *35* (24), 4178–4180.

(18) West, B. A.; Moran, A. M. Two-Dimensional Electronic Spectroscopy in the Ultraviolet Wavelength Range. *J. Phys. Chem. Lett.* **2012**, *3* (18), 2575–2581.

(19) Krebs, N.; Pugliesi, I.; Hauer, J.; Riedle, E. Two-Dimensional Fourier Transform Spectroscopy in the Ultraviolet with Sub-20 Fs Pump Pulses and 250-720 Nm Supercontinuum Probe. *NEW J. Phys.* **2013**, *15*.

(20) Prokhorenko, V. I.; Picchiotti, A.; Maneshi, S.; Dwayne Miller, R. J. Broadband Electronic Two-Dimensional Spectroscopy in the Deep UV. *Springer Proceedings in Physics*. Springer: Yamanouchi, K. 2015, pp 432–435.

(21) Asplund, M. C.; Zanni, M. T.; Hochstrasser, R. M. Two-Dimensional Infrared Spectroscopy of Peptides by Phase-Controlled Femtosecond Vibrational Photon Echoes. *Proc. Natl. Acad. Sci. U. S. A.* **2000**, *97* (15), 8219–8224.

(22) Khalil, M.; Demirdoven, N.; Tokmakoff, A. Coherent 2D IR Spectroscopy: Molecular Structure and Dynamics in Solution. *J. Phys. Chem. A* **2003**, *107* (27), 5258–5279.

(23) Zheng, J.; Kwak, K.; Fayer, M. D. Ultrafast 2D IR Vibrational Echo Spectroscopy. *Acc. Chem. Res.* **2007**, *40* (1), 75–83.

(24) Roberts, S. T.; Ramasesha, K.; Tokmakoff, A. Structural Rearrangements in Water Viewed Through Two-Dimensional Infrared Spectroscopy. *Acc. Chem. Res.* **2009**, *42* (9, SI), 1239–1249.

(25) Bakulin, A. A.; Liang, C.; Jansen, T. L. C.; Wiersma, D. A.; Bakker, H. J.; Pshenichnikov, M. S. Hydrophobic Solvation: A 2D IR Spectroscopic Inquest. *Acc. Chem. Res.* **2009**, *42* (9), 1229–1238.

(26) Hamm, P.; Zanni, M. T. *Concepts and Methods of 2D Infrared Spectroscopy*; Cambridge University Press, 2011.

(27) Rubtsov, I. V; Kumar, K.; Hochstrasser, R. M. Dual-Frequency 2D IR Photon Echo of a Hydrogen Bond. *Chem. Phys. Lett.* **2005**, *402* (4–6), 439–443.

(28) Kurochkin, D. V; Naraharisetty, S. R. G.; Rubtsov, I. V. A Relaxation-Assisted 2D IR Spectroscopy Method. *Proc. Natl. Acad. Sci. U. S. A.* **2007**, *104* (36), 14209–14214.

(29) Leger, J. D.; Nyby, C. M.; Varner, C.; Tang, J.; Rubtsova, N. I.; Yue, Y.; Kireev, V. V; Burtsev, V. D.; Qasim, L. N.; Rubtsov, G. I.; et al. Fully Automated Dual-Frequency Three-Pulse-Echo 2DIR Spectrometer Accessing Spectral Range from 800 to 4000 Wavenumbers. *Rev. Sci. Instrum.* **2014**, *85* (8).

(30) Mandal, A.; Ramasesha, K.; De Marco, L.; Tokmakoff, A. Collective Vibrations of Water-Solvated Hydroxide Ions Investigated with Broadband 2DIR Spectroscopy. *J. Chem. Phys.* **2014**, *140* (20).

(31) Costard, R.; Heisler, I. A.; Elsaesser, T. Structural Dynamics of Hydrated Phospholipid Surfaces Probed by Ultrafast 2D Spectroscopy of Phosphate Vibrations. *J. Phys. Chem. Lett.* **2014**, *5* (3), 506–511.

(32) Elsaesser, T. Two-Dimensional Infrared Spectroscopy of Intermolecular Hydrogen Bonds in the Condensed Phase. *Acc. Chem. Res.* **2009**, *42* (9), 1220–1228.

(33) Savolainen, J.; Ahmed, S.; Hamm, P. Two-Dimensional Raman-Terahertz Spectroscopy of Water. *Proc. Natl. Acad. Sci. U. S. A.* **2013**, *110* (51), 20402–20407.

(34) Lynch, M. S.; Cheng, M.; Van Kuiken, B. E.; Khalil, M. Probing the Photoinduced Metal-Nitrosyl Linkage Isomerism of Sodium Nitroprusside in Solution Using Transient Infrared Spectroscopy. *J. Am. Chem. Soc.* **2011**, *133* (14), 5255–5262.

(35) Zhang, W.; Ji, M.; Sun, Z.; Gaffney, K. J. Dynamics of Solvent-Mediated Electron Localization in Electronically Excited Hexacyanoferrate(III). *J. Am. Chem. Soc.* **2012**, *134* (5), 2581–2588.

(36) Nibbering, E. T. J.; Fidder, H.; Pines, E. Ultrafast Chemistry: Using Time-Resolved Vibrational Spectroscopy for Interrogation of Structural Dynamics. *Annu. Rev. Phys. Chem.* **2005**, *56*, 337–367.

(37) Ishii, K.; Takeuchi, S.; Tahara, T. Infrared-Induced Coherent Vibration of a Hydrogen-Bonded System: Effects of Mechanical and Electrical Anharmonic Couplings. *J. Chem. Phys.* **2009**, *131* (4).

(38) Belabas, N.; Joffre, M. Visible-Infrared Two-Dimensional Fourier-Transform Spectroscopy. *Opt. Lett.* **2002**, *27* (22), 2043–2045.

(39) Bredenbeck, J.; Helbing, J.; Hamm, P. Continuous Scanning from Picoseconds to Microseconds in Time Resolved Linear and Nonlinear Spectroscopy. *Rev. Sci. Instrum.* **2004**.

(40) Baiz, C. R.; Nee, M. J.; McCanne, R.; Kubarych, K. J. Ultrafast Nonequilibrium Fourier-

Transform Two-Dimensional Infrared Spectroscopy. *Opt. Lett.* **2008**, *33* (21), 2533–2535.

(41) Xiong, W.; Laaser, J. E.; Paoprasert, P.; Franking, R. A.; Hamers, R. J.; Gopalan, P.; Zanni, M. T. Transient 2D IR Spectroscopy of Charge Injection in Dye-Sensitized Nanocrystalline Thin Films. *J. Am. Chem. Soc.* **2009**, *131* (50), 18040.

(42) Lynch, M. S.; Slenkamp, K. M.; Cheng, M.; Khalil, M. Coherent Fifth-Order Visible-Infrared Spectroscopies: Ultrafast Nonequilibrium Vibrational Dynamics in Solution. *J. Phys. Chem. A* **2012**, *116* (26), 7023–7032.

(43) van Wilderen, L. J. G. W.; Messmer, A. T.; Bredenbeck, J. Mixed IR/Vis Two-Dimensional Spectroscopy: Chemical Exchange beyond the Vibrational Lifetime and Sub-Ensemble Selective Photochemistry. *Angew. Chem. Int. Ed.* **2014**, *53* (10), 2667–2672.

(44) van Wilderen, L. J. G. W.; Bredenbeck, J. From Ultrafast Structure Determination to Steering Reactions: Mixed IR/Non-IR Multidimensional Vibrational Spectroscopies. *Angew. Chem. Int. Ed.* **2015**, *54* (40), 11624–11640.

(45) Oliver, T. A. A.; Lewis, N. H. C.; Fleming, G. R. Correlating the Motion of Electrons and Nuclei with Two-Dimensional Electronic-Vibrational Spectroscopy. *Proc. Natl. Acad. Sci. U. S. A.* **2014**, *111* (28), 10061–10066.

(46) Lewis, N. H. C.; Dong, H.; Oliver, T. A. A.; Fleming, G. R.; Lewis, N. H. C.; Dong, H.; Oliver, T. A. A.; Fleming, G. R. Measuring Correlated Electronic and Vibrational Spectral Dynamics Using Line Shapes in Two-Dimensional Electronic-Vibrational Spectroscopy Measuring Correlated Electronic and Vibrational Spectral Dynamics Using Line Shapes in Two-Dimensional Electronic-Vi. *J. Chem. Phys.* **2015**, *142*, 174202.

(47) Terenziani, F.; Painelli, A. Two-Dimensional Electronic-Vibrational Spectra: Modeling Correlated Electronic and Nuclear Motion. *Phys. Chem. Chem. Phys.* **2015**, *17* (19), 13074–13081.

(48) Dong, H.; Lewis, N. H. C.; Oliver, T. A. A.; Fleming, G. R. Determining the Static Electronic and Vibrational Energy Correlations via Two-Dimensional Electronic-Vibrational Spectroscopy. *J. Chem. Phys.* **2015**, *142* (17).

(49) Courtney, T. L.; Fox, Z. W.; Estergreen, L.; Khalil, M. Measuring Coherently Coupled Intramolecular Vibrational and Charge-Transfer Dynamics with Two-Dimensional Vibrational Electronic Spectroscopy. *J. Phys. Chem. Lett.* **2015**, *6* (7), 1286–1292.

(50) Park, K.; Cho, M. H. Time- and Frequency-Resolved Coherent Two-Dimensional IR Spectroscopy: Its Complementary Relationship with the Coherent Two-Dimensional Raman Scattering Spectroscopy. *J. Chem. Phys.* **1998**, *109* (24), 10559–10569.

(51) Cho, M. H. Triply Resonant Infrared-Infrared-Visible Sum Frequency Generation: Three-Dimensional Vibronic Spectroscopy for the Investigation of Vibrational and Vibronic Couplings. *J. Chem. Phys.* **2000**, *112* (20), 9002–9014.

(52) Cho, M. H. Two-Dimensional Vibrational Spectroscopy. VII. Investigation of the Vibronic and Vibrational Couplings by Using Novel Triply Resonant Two-Dimensional Vibrational Spectroscopies. *J. Chem. Phys.* **2000**, *113* (18), 7746–7755.

(53) Zhao, W.; Wright, J. C. Doubly Vibrationally Enhanced Four Wave Mixing: The Optical Analog to 2D NMR. *Phys. Rev. Lett.* **2000**, *84* (7), 1411–1414.

(54) Bonn, M.; Hess, C.; Miners, J. H.; Heinz, T. F.; Bakker, H. J.; Cho, M. Novel Surface Vibrational Spectroscopy: Infrared-Infrared-Visible Sum-Frequency Generation. *Phys. Rev. Lett.* **2001**, *86* (8), 1566–1569.

(55) Faeder, S. M. G.; Jonas, D. M. Two-Dimensional Electronic Correlation and Relaxation Spectra: Theory and Model Calculations. *J. Phys. Chem. A* **1999**, *103* (49), 10489–10505.

(56) DeFlores, L. P.; Nicodemus, R. A.; Tokmakoff, A. Two Dimensonal Fourier Transform Spectroscopy in the Pump-Probe Geometry. *Opt. Lett.* **2007**, *32* (20), 2966–2968.

(57) Shim, S.-H.; Strasfeld, D. B.; Ling, Y. L.; Zanni, M. T. Automated 2D IR Spectroscopy Using a Mid-IR Pulse Shaper and Application of This Technology to the Human Islet Amyloid Polypeptide. *Proc. Natl. Acad. Sci. U. S. A.* **2007**, *104* (36), 14197–14202.

(58) Vogler, A.; Kisslinger, J. Photosubstitution of Pentaamminechlororuthenium(III) Hexacyanoruthenate(II) Following Outer-Sphere Intervalence Excitation. *J. Am. Chem. Soc.* **1982**, *104* (8), 2311–2312.

(59) Slenkamp, K. M.; Lynch, M. S.; Van Kuiken, B. E.; Brookes, J. F.; Bannan, C. C.; Daifuku, S. L.; Khalil, M. Investigating Vibrational Anharmonic Couplings in Cyanide-Bridged Transition Metal Mixed Valence Complexes Using Two-Dimensional Infrared Spectroscopy. *J. Chem. Phys.* **2014**, *140* (8).

(60) Albrecht, A. W.; Hybl, J. D.; Faeder, S. M. G.; Jonas, D. M. Experimental Distinction between Phase Shifts and Time Delays: Implications for Femtosecond Spectroscopy and Coherent Control of Chemical Reactions. *J. Chem. Phys.* **1999**, *111* (24), 10934–10956.

(61) Ferro, A. W. A.; Hybl, J. D.; Faeder, S. M. G.; Jonas, D. M. Experimental Distinction between Phase Shifts and Time Delays: Implications for Femtosecond Spectroscopy and Coherent Control of Chemical Reactions (Vol 111, Pg 10934, 1999). *J. Chem. Phys.* **2001**, *115* (12), 5691.

(62) Grumstrup, E. M.; Shim, S.-H.; Montgomery, M. A.; Damrauer, N. H.; Zanni, M. T. Facile Collection of Two-Dimensional Electronic Spectra Using Femtosecond Pulse-Shaping Technology. *Opt. Express* **2007**, *15* (25), 16681–16689.

(63) Myers, J. A.; Lewis, K. L. M.; Tekavec, P. F.; Ogilvie, J. P. Two-Color Two-Dimensional Fourier Transform Electronic Spectroscopy with a Pulse-Shaper. *Opt. Express* **2008**, *16* (22), 17420–17428.

(64) Mukamel, S. *Principles of Nonlinear Optic and Spectroscopy*; Oxford University Press: New York, 1995.

(65) Gardecki, J. A.; Constantine, S.; Zhou, Y.; Ziegler, L. D. Optical Heterodyne Detected Spectrograms of Ultrafast Nonresonant Electronic Responses. *J. Opt. Soc. Am. B Opt. Phys.* **2000**, *17* (4), 652–662.

(66) Yeremenko, S.; Baltuska, A.; de Haan, F.; Pshenichnikov, M. S.; Wiersma, D. A. Frequency-Resolved Pump-Probe Characterization of Femtosecond Infrared Pulses. *Opt.*

Lett. **2002**, *27* (13), 1171–1173.

(67) Heiman, D.; Hellwarth, R. W.; Levenson, M. D.; Martin, G. Raman-Induced Kerr Effect. *Phys. Rev. Lett.* **1976**, *36* (4), 189–192.

(68) Sheikbahae, M.; Said, A. A.; Vanstryland, E. W. High-Sensitivity Single-Beam N2 Measurements. *Opt. Lett.* **1989**, *14* (17), 955–957.

(69) Fecko, C. J.; Eaves, J. D.; Tokmakoff, A. Isotropic and Anisotropic Raman Scattering from Molecular Liquids Measured by Spatially Masked Optical Kerr Effect Spectroscopy. *J. Chem. Phys.* **2002**, *117* (3), 1139–1154.

(70) Cong, P. J.; Chang, Y. J.; Simon, J. D. Complete Determination of Intermolecular Spectral Densities of Liquids Using Position-Sensitive Kerr Lens Spectroscopy. *J. Phys. Chem.* **1996**, *100* (21), 8613–8616.

(71) Gardecki, J. A.; Yu, G.; Constantine, S.; Peng, J.; Zhou, Y.; Ziegler, L. D. A Unified Treatment of Ultrafast Optical Heterodyne Detected and Z-Scan Spectroscopies. *J. Chem. Phys.* **2001**, *114* (8), 3586–3597.

(72) Wang, C. F.; Mohney, B. K.; Akhremitchev, B. B.; Walker, G. C. Ultrafast Infrared Spectroscopy of Vibrational States Prepared by Photoinduced Electron Transfer in (CN)(5)FeCNRu(NH3)(5)(-). *J. Phys. Chem. A* **2000**, *104* (18), 4314–4320.

Chapter 3

Experimental 2D Vibrational-Electronic Spectroscopy Measurements on Intramolecular Charge-Transfer Compounds

The work presented in this chapter has been published in the following paper:

- *Courtney, T. L.; Fox, Z. W.; Slenkamp, K. M.; and Khalil, M., "Two Dimensional Vibrational-Electronic Spectroscopy", J. Chem. Phys.,* ***2015****, 143, 154201.*

The VE spectra and related discussion are presented for each of three molecules introduced in Chapter 2 dissolved in FA: $[Fe^{III}(CN)_6]^{3-}$, FeRu, and $[Fe^{II}(CN)_6]^{4-}$. The structures and linear FTIR and UV/Vis/near-IR spectra of the compounds are shown in Figure 3-1. 1D VE and 2D VE spectroscopy techniques are demonstrated in the detection and analysis of the coupling of the ν_{CN} mode to the LMCT transition in $[Fe^{III}(CN)_6]^{3-}$ (Section 3.1). The selectivity of 2D VE spectroscopy is revealed in an analysis of relaxation dynamics of the ν_{CN} mode-specific couplings to the MMCT electronic transition in FeRu (Section 3.2). Finally, the distinction between fully resonant and optically nonresonant experiments is made with 2D VE data of $[Fe^{II}(CN)_6]^{4-}$ (Section 3.3).

3.1 Coupling of vibrations to LMCT transition in $[Fe^{III}(CN)_6]^{3-}$

The molecule $[Fe^{III}(CN)_6]^{3-}$ has strong charge transfer absorption bands and has been extensively studied by ultrafast spectroscopy. Recently, Gaffney and coworkers studied the hole delocalization dynamics after LMCT excitation in $[Fe^{III}(CN)_6]^{3-}$ using polarization selective transient IR spectroscopy.[1] Their results revealed that the hole delocalizes on all six CN ligands

upon photoexcitation and that the localization of the hole on a picosecond timescale is solvent-dependent. Additionally, ultrafast mid-IR pump-probe experiments of $[Fe^{III}(CN)_6]^{3-}$ and related compounds have measured vibrational energy relaxation (VER) in multiple solvents.[2] The VER time of $[Fe^{III}(CN)_6]^{3-}$ is <15 ps, decreasing slightly with solvent polarity. Photoexcitation of $[Fe^{III}(CN)_6]^{3-}$ yields $[Fe^{II}(CN)_6]^{4-}$ (Figure 3-1(a)). $[Fe^{II}(CN)_6]^{4-}$, which will be presented in Section 3.3, has a ν_{CN} vibration that is red shifted by ~74.5 cm^{-1} (Figure 3-1(b), dotted black line). In this section, I will demonstrate the new 2D VE spectroscopy on the molecule $[Fe^{III}(CN)_6]^{3-}$.

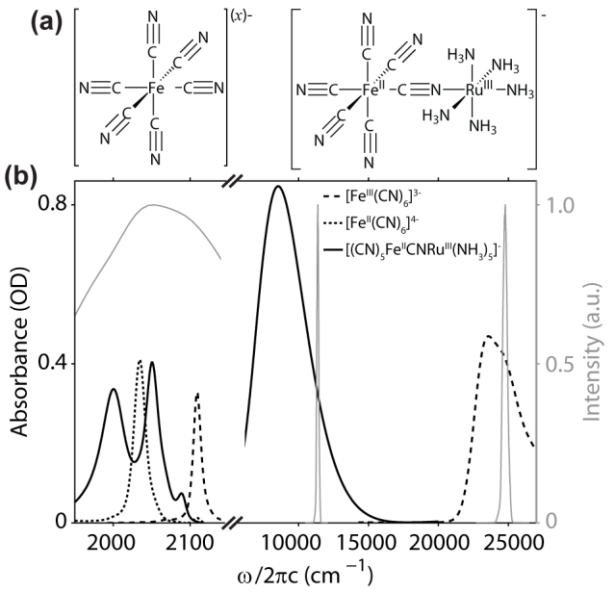

Figure 3-1 Hexacyanoferrates $[Fe(CN)_6]^{(x)-}$ and mixed valence complex of FeRu. (a) Molecular structures of $[Fe^{III}(CN)_6]^{3-}$ (x = 3), $[Fe^{II}(CN)_6]^{4-}$ (x = 4), and FeRu. (b) Linear, solvent-subtracted spectra of $[Fe^{III}(CN)_6]^{3-}$ (dashed black lines), $[Fe^{II}(CN)_6]^{4-}$ (dotted black line), and FeRu (solid black lines) in formamide share left vertical axis and are plotted with laser spectra (solid gray lines, right vertical axis). At mid-IR frequencies: FTIR spectra of $[Fe^{III}(CN)_6]^{3-}$, $[Fe^{II}(CN)_6]^{4-}$, and FeRu with pump spectrum ($\nu_{max\ mid\text{-}IR}$ = 2050 cm^{-1}). At optical frequencies: UV/visible $[Fe^{III}(CN)_6]^{3-}$ and probe ($\nu_{max\ visible}$ = 24750 cm^{-1}) spectra; near-IR FeRu and probe ($\nu_{max\ near\text{-}IR}$ = 11750 cm^{-1}) spectra. $[Fe^{II}(CN)_6]^{4-}$ is optically nonresonant. Transition frequencies are the following: $\nu_{max\ LMCT}$ = 23585 cm^{-1} and ν_{CN} = 2109.0 cm^{-1} in $[Fe^{III}(CN)_6]^{3-}$; ν_{CN} = 2034.5 cm^{-1} in $[Fe^{II}(CN)_6]^{4-}$; $\nu_{max\ MMCT}$ = 8547 cm^{-1} and ν_{CN} modes of ν_{bridge} = 2089.4 cm^{-1}, ν_{axial} = 2065 cm^{-1}, ν_{radial} = 2050.6 cm^{-1}, and ν_{trans} = 2002.0 cm^{-1} in FeRu.

Figure 3-1(b) displays the relevant electronic and vibrational transitions (dashed black lines) and laser spectra (solid gray lines) for $[Fe^{III}(CN)_6]^{3-}$ VE experiments, in which first the compound

is dissolved in FA and then excite the ν_{CN} = 2109.0 cm^{-1} vibration with a mid-IR pump (1D VE) or mid-IR pump pulse pairs (2D VE) centered at $\nu_{max\ mid\text{-}IR} \approx 2050\ cm^{-1}$. The resulting population is probed slightly to the blue side of the electronic transition ($\nu_{max\ LMCT} \approx 23585\ cm^{-1}$) with a visible pulse ($\nu_{max\ visible} \approx 24750\ cm^{-1}$). The 1D VE and 2D VE spectra of $[Fe^{III}(CN)_6]^{3-}$ dissolved in FA and of neat FA are shown in Figure 3-2. The 1D VE $[Fe^{III}(CN)_6]^{3-}$ (Figure 3-2(e)) and solvent only (Figure 3-2(j)) spectra are normalized to Figure 3-2(e); the 2D VE solute (Figure 3-2(a-d)) and solvent only (Figure 3-2(f-i)) spectra at a series of τ_2 delays are normalized to Figure 3-2(a). The neat FA spectra are collected immediately following the $[Fe^{III}(CN)_6]^{3-}$ spectra using the flowing apparatus to empty the sample, rinse with neat solvent, and circulate fresh FA while not adjusting the sample position or beam steering. To provide the most direct comparison between the solute and solvent only VE spectra, the copropagating signal and LO are attenuated by a neutral density filter after the neat solvent sample to match the LO intensity to that after the $[Fe^{III}(CN)_6]^{3-}$ sample to account for solute absorption. This comparison is limited by the accuracy of the neat FA signal reduction as follows. The probe is progressively absorbed throughout the $[Fe^{III}(CN)_6]^{3-}$ sample, yielding a weaker FA signal than that from the FA sample with no probe attenuation. However, the ratio of the FA signal fields between the two samples may not be equal to the ratio of resulting LO fields. Given this caveat, the attenuation of the probe beam after the neat FA sample matches the maximum counts of the neat FA and $[Fe^{III}(CN)_6]^{3-}$ LO spectra to within 1%. The maximum counts in the 1D VE signals are also matched to within 1%, as can be seen in Figure 3-2(e) and (j).

2D VE spectroscopy provides the temporal and excitation frequency resolutions to measure vibronic couplings, as illustrated by the 2D VE spectra of $[Fe^{III}(CN)_6]^{3-}$ in FA (Figure 3-2(a-d)). The coupling between the ν_{CN} mode and the LMCT charge transfer in $[Fe^{III}(CN)_6]^{3-}$ is evident

from the positive (red) GSB signal (corresponding to $D_{R,2} + D_{NR,2}$ in Figure 2-2) localized at the ω_1 of the ν_{CN} mode. The ω_1 position and intensity of this peak are relatively constant over early τ_2 delays, but the maximum intensity ω_3 position varies with τ_2 as discussed below. Additionally, a negative (blue) peak is centered at 2050 cm^{-1} in ω_1 (Figure 3-2(b-d)), which is attributed to excited state absorption (ESA) ($D_{R,1} + D_{NR,1}$ in Figure 2-2) of a combination mode, $\nu_{CN\text{-}low}$, of coupled high-frequency ν_{CN} and low-frequency (59 cm^{-1}) modes. As mentioned in Section 2.2, the relative amplitudes of 2D VE signals can be different for ν_{CN} and coupled ν_{CN} and low-frequency modes based on vibronic coupling factors. For ν_{CN} mode excitation, the overlap between $|g,0\rangle$ and $|e,0'\rangle$ states is stronger than that between $|g,1\rangle$ and $|e,1'\rangle$; however, for excitation of the $\nu_{CN\text{-}low}$ mode, the overlap between $|g,(1-low)\rangle$ and either $|e,(1-low)'\rangle$ or $|e,1'\rangle$ appears to dominate. As discussed in Section 2.3.2, all VE signals are reported as the product of signal and LO fields. Since the 2D VE signal of $[Fe^{III}(CN)_6]^{3-}$ represented in this manner has strength proportional to the probe field, the actual 2D VE signal field is expected to extend beyond the spectral width of the probe. Each 2D VE spectrum of $[Fe^{III}(CN)_6]^{3-}$ has only one peak along ω_3 at the ω_1 of a given electronically coupled IR-active mode, compared to the five labeled peaks in the Figure 2-2(d) cartoon spectrum. The absence of peaks 3-5 is due to the finite probe bandwidth. Furthermore, the ESA and GSB peaks (1 and 2, respectively, in Figure 2-2) likely have a large overlap in detection frequency, as even a vibrational mode-specific electronic transition is expected to be spectrally broad due to underlying vibronic structure compared to both the Δ_{eg} separation in ω_3 of peak centers and the probe bandwidth. The 2D VE spectra presented here display the noncanceling, broad portion of either the ESA or GSB signal at a given ω_1 that involves states favored by a Franck-Condon overlap.

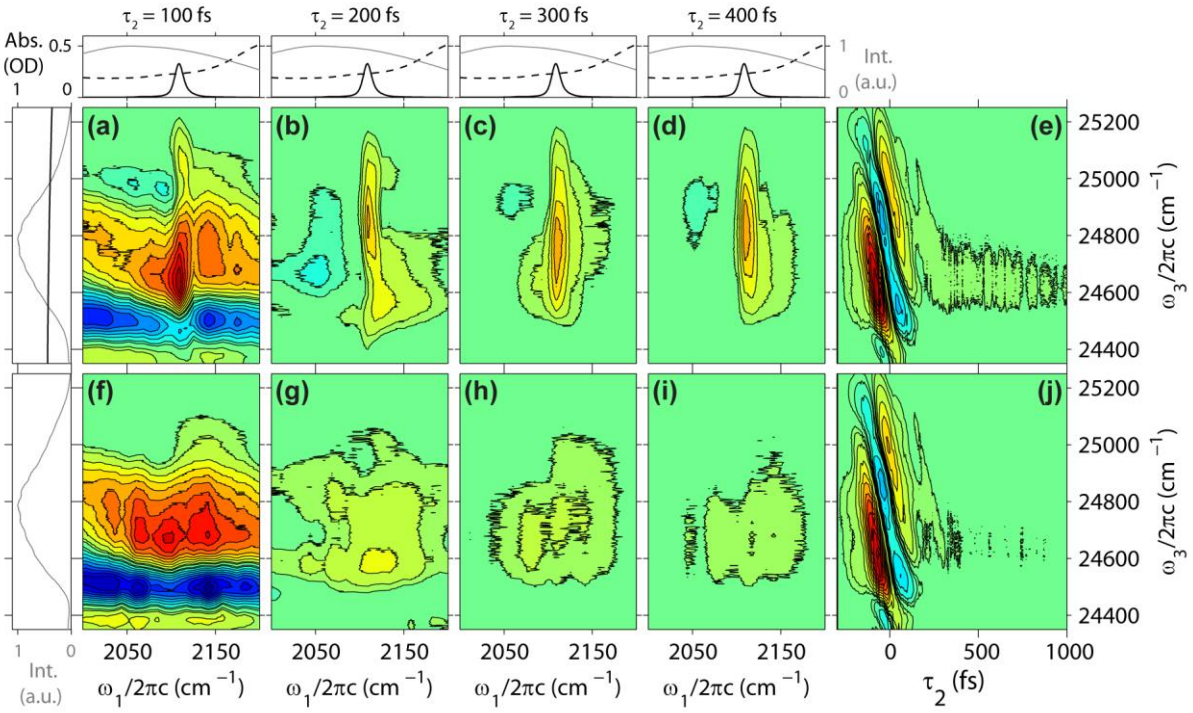

Figure 3-2 Vibrational-electronic (VE) spectra of $[Fe^{III}(CN)_6]^{3-}$ in formamide (FA) (a-e) and neat FA (f-j). Top panels: IR pump pulse spectra (solid gray lines) and FTIR spectra of both FA (dashed black lines) and solvent-subtracted $[Fe^{III}(CN)_6]^{3-}$ (solid black lines). Left panels: UV/visible probe pulse spectra (solid gray lines) and linear electronic spectrum of $[Fe^{III}(CN)_6]^{3-}$ in FA (solid black line). All linear (pulse) spectra are plotted in black (gray) to correspond with absorbance (intensity, Int.) axes. (a-d) 2D VE spectra of $[Fe^{III}(CN)_6]^{3-}$ for a series of waiting times show bleaches (red) at the cyanide stretching mode frequency. (f-i) Electronically nonresonant solvent signals in 2D VE spectra of neat FA underlie $[Fe^{III}(CN)_6]^{3-}$ 2D VE signals, most notably in (f). Panels (a-d, f-i) are normalized to panel (a). 1D vibrational-electronic (VE) spectra of $[Fe^{III}(CN)_6]^{3-}$ in formamide (FA) (e) and neat FA (j). Panel (j) spectrum is normalized to (e); 2D VE spectra are plotted using contour lines at the following positions: ±0.05, ±0.1, ±0.2, ±0.3, ±0.4, ±0.5, ±0.6, ±0.7, ±0.8, ±0.9, and ±1.0; 1D VE spectra have an additional ±0.025 contour line

The excitation frequency resolution of 2D VE spectroscopy proves advantageous in enhancing resonant VE signals with respect to background signals. In the 1D VE spectrum of $[Fe^{III}(CN)_6]^{3-}$, the resonant signal is evident only in the lowest positive contour (Figure 3-2(e)) as compared to the neat FA 1D VE spectrum (Figure 3-2(j)). As in the 1D VE spectra (Figure 3-2(e) and (j)), the background solvent 2D VE signal is nearly identical in the $[Fe^{III}(CN)_6]^{3-}$ and neat FA samples and is most notable near $\tau_2 = 0$. By $\tau_2 = 400$ fs (Figure 3-2(i)), the solvent signal persists at about 10% of the initial ($\tau_2 = 100$ fs) maximum counts; however, the maximum $[Fe^{III}(CN)_6]^{3-}$ bleach (Figure 3-2(d)) is >40% of the $\tau_2 = 100$ fs maximum. In contrast, the ID VE $[Fe^{III}(CN)_6]^{3-}$ and neat FA signal maxima at $\tau_2 = 400$ fs are ~15% and 10%, respectively, of the solvent-dominated $\tau_2 = 100$

fs maximum signal. The localization of the VE signal at the narrow ν_{CN} mode (12 cm^{-1} FWHM width) results in the increased ratio of resonant signal to broad background in 2D VE spectra. Still, the 2D VE $[Fe^{III}(CN)_6]^{3-}$ signals are weak above the FA background compared to those in FeRu (Section 3.2), which implies a small effective electronic dipole moment, $|\mu_{elec}^{eff}|$, where $|\mu_{elec}^{eff}|$ is a previously introduced quantifier of vibronic coupling.[3] Additionally, the implicit integration over ω_1 of the 1D VE spectra gives rise to the cancellation at higher detection frequencies of a portion of the GSB signal with the oppositely signed signal from the coupled low-frequency mode at 2050 cm^{-1}. Thus the weak 1D VE $[Fe^{III}(CN)_6]^{3-}$ signal detected at ~24600 cm^{-1} is also red-shifted from the peak maxima of 2D VE signals (Figure 3-2(c) and (d)), which are roughly centered on $\nu_{max\ visible} \approx 24750\ cm^{-1}$ with slight variation (discussed below). In 1D VE spectra or individual τ_1 slices of 2D VE time-domain data, the maximum magnitude signals correspond to absorbance changes of $|\Delta A| = 30$ mOD near $\tau_2 = 0$ and $|\Delta A| \approx 0.5$ mOD at positive τ_2 delays beyond the instrument response. Performing the FT produces 2D VE spectra with added information compared to 1D VE spectra: features narrow in ω_1 with high signal to noise, noncanceling features of opposite signs resolved in ω_1, and sensitivity of peak movement in ω_3 as a function of τ_2.

The line shapes and positions of 2D VE spectral peaks report on the correlations and couplings of vibrational modes and the electronic transition. In an earlier publication,[3] the Khalil group introduced an analysis of 2D VE spectral line shapes that uses a procedure most similar to the center line slope (CLS) ω_τ method.[4,5] Briefly, each ω_3 slice (parallel to the ω_1 axis) of a 2D VE spectrum is interpolated via a cubic spline to find the precise ω_1 frequency corresponding to the maximum of the ν_{CN} peak. These ω_1 maxima are plotted against ω_3 and fit to the form $\omega_1 = \omega_o + m(\omega_3 - \omega_c)\omega_1$, where ω_o is the ω_1 frequency at ω_c, a central ω_3 frequency in the 2D VE peak. The slopes, m, corresponding to the 2D VE spectra in Figure 3-2(a–d) are zero within errors of

distortions in $[Fe^{III}(CN)_6]^{3-}$ 2D VE spectra caused by solvent (Figure 3-2(f–i)). Unlike the tilted peaks in FeRu presented in earlier experiments[3] and discussed in Section 3.2, the 2D VE peaks in $[Fe^{III}(CN)_6]^{3-}$ do not imply frequency correlation between the charge transfer and ν_{CN} vibrations within the 180 fs time resolution of the experiment. Furthermore, the location of the ν_{CN} mode in $[Fe^{III}(CN)_6]^{3-}$ in ω_1 is constant across the four τ_2 delays in Figure 3-2(a–d), with $\omega_o = 2111.4 \pm 0.4$ cm^{-1} at $\omega_c = 24800$ cm^{-1}. However, the ω_3 position of the $[Fe^{III}(CN)_6]^{3-}$ 2D VE ν_{CN} peak changes with τ_2 delay in an oscillatory fashion as follows: 24540, 24880, 24770, and 24850 cm^{-1} for 100, 200, 300, and 400 fs delays, respectively, measured at $\omega_1 = 2109$ cm^{-1}. One possible explanation of this effect could be the nonresonant signal contribution. However, the nonresonant signal contribution decays monotonically with waiting time with a relatively consistent shape and location. Therefore, the oscillating position of the positive ν_{CN} peak may be attributed to a coherence during τ_2 between $|g,0\rangle$ and $|g,low\rangle$ states, where the low-frequency mode need not be the same 59 cm^{-1} mode observed in the ω_1 dimension. Another possibility is interference of the positive ν_{CN} and negative $\nu_{CN\text{-}low}$ peaks as a function of waiting time.

3.2 Relaxation dynamics of MMCT-coupled modes: $[(CN)_5Fe^{II}CNRu^{III}(NH_3)_5]^-$

FeRu (Figure 3-1(a)) is a cyanide-bridged complex containing two metal centers with different oxidation states. It is part of a class of two- and three-metal complexes that have been used in steady-state and time-resolved spectroscopic experiments to help understand the coupling between electronic and vibrational motions during ultrafast electron transfer reactions.[6–14] Transient IR, optical, and Raman spectroscopic studies have found that some of the high frequency ν_{CN} vibrations are involved in the charge transfer process[6,9,12,13] and that significant excitation exists in

the ν_{CN} modes upon ultrafast back electron transfer.[11,12,14] The Khalil group has used 2D IR spectroscopy of FeRu dissolved in D_2O and FA to study the vibrational anharmonic couplings among the four ν_{CN} modes and the role of solvent in modulating the molecular structure and anharmonic couplings of the molecule.[15] Previous work has assigned the electronic transition in FeRu to be a MMCT excitation from the Fe^{II} to the Ru^{III}, resulting in Fe^{III} and Ru^{II}.[6] To accomplish the present experiment, FeRu is dissolved in FA, excite four ν_{CN} vibrations,[15] ν_{bridge} (2089.4 cm^{-1}), ν_{axial} (2065 cm^{-1}), ν_{radial} (2050.6 cm^{-1}), and ν_{trans} (2002.0 cm^{-1}), with a mid-IR pump or pump pulse pair centered at $\nu_{max\ mid\text{-}IR} \approx 2050\ cm^{-1}$, and probe the resulting population on the blue side of the broad electronic transition ($\nu_{max\ MMCT} \approx 8547\ cm^{-1}$) with a near-IR continuum ($\nu_{max\ near\text{-}IR} \approx 11750\ cm^{-1}$).[3] Figure 3-1(b) includes laser spectra (solid gray lines) and solvent-subtracted FeRu linear absorption spectra (solid black lines) for the VE spectroscopy of FeRu. Because $\nu_{max\ near\text{-}IR}$ is more than one quantum of ν_{CN} vibration greater than $\nu_{max\ MMCT}$, the 2D VE signals of FeRu involve probe transitions from a ground state, $|g, n\rangle$, to the electronically excited state, $|e, (n+1)'\rangle$ (peaks 3 and 4 in Figure 2-2), or even $|e, (n+2)'\rangle$. Sample conditions in the FeRu and $[Fe^{III}(CN)_6]^{3-}$ solutions have the following similarities (Figure 3-1(b)): approximately equal maximum ν_{CN} mode absorptions, approximately equal charge transfer absorptions at the central probe frequencies, and comparable ν_{CN} mode line widths (12 cm^{-1} FWHM in $[Fe^{III}(CN)_6]^{3-}$, 5 to 21 cm^{-1} in FeRu[15]). Given the difference in energy of the ν_{CN} vibrations between $[Fe^{III}(CN)_6]^{3-}$ and $[Fe^{II}(CN)_6]^{4-}$, a shift of approximately Δ_{eg} = 74.5 cm^{-1} is expected in all four ν_{CN} modes in FeRu VE spectroscopies. The sign of Δ_{eg} and the oxidation states of Fe in electronic ground and excited states are reversed from those in the $[Fe^{III}(CN)_6]^{3-}$ VE experiments.

The 2D VE spectra of FeRu in FA are shown at a series of τ_2 delays in Figure 3-3, and all panels (Figure 3-3(a-e)) are normalized to Figure 3-3(a). As with the $[Fe^{III}(CN)_6]^{3-}$ experiment, VE spectra of neat FA are collected immediately following the sample spectra. However, a static sample cell is used, and care is taken to reproduce the sample position without adjusting any experimental alignment. Again, the LO counts are matched through attenuation of the probe beam after the neat FA sample. In both 1D VE and 2D VE spectra, the FeRu signal is stronger above the solvent signal (2D VE solvent comparison to previous work[3]) than in $[Fe^{III}(CN)_6]^{3-}$ (Figure 3-2). This could be attributed to one or more of the following: a larger total IR dipole moment in FeRu given the four ν_{CN} modes, a larger vibrational-electronic coupling between ν_{CN} modes and the charge transfer transition in FeRu, a difference in MMCT versus LMCT transitions, and the relative frequency separations between the probe and charge transition spectral centers. Also, the neat FA signal itself is much weaker with the near-IR probe than the visible probe (magnitude of 4 mOD compared to 30 mOD at ω_3 of maximum signal near $\tau_2 = 0$ in 1D VE spectra). A possible explanation for this could be the fact that at 400 nm, the probe is pre-resonant with the solvent UV/VIS spectra, which has a peak at 306 nm.

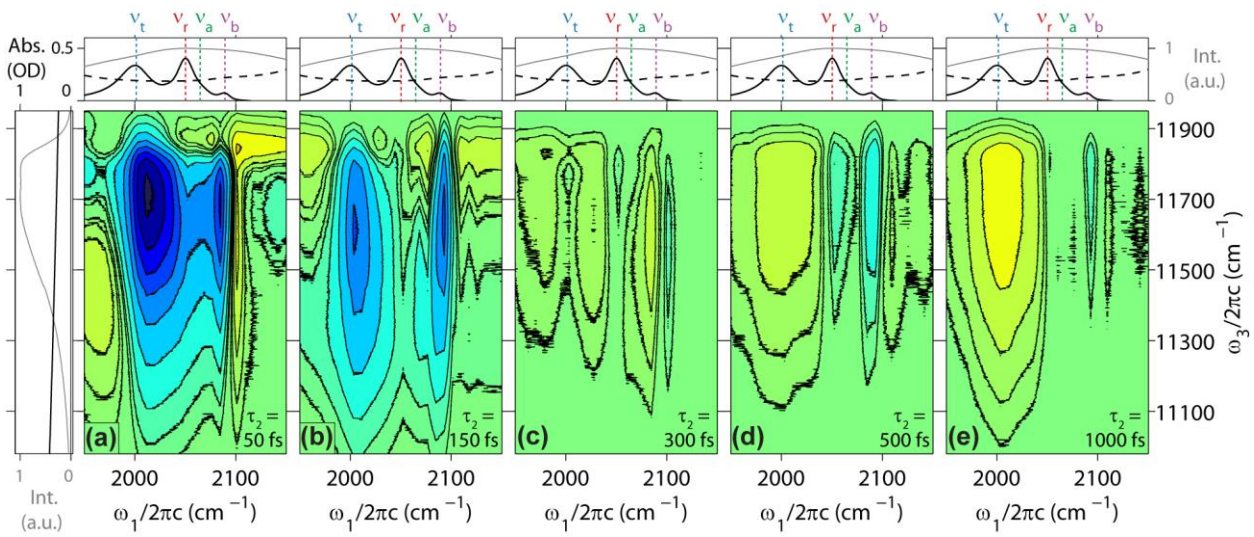

Figure 3-3 2D vibrational-electronic (2D VE) spectra of $[(CN)_5Fe^{II}CNRu^{III}(NH_3)_5]^-$ (FeRu) dissolved in formamide (FA). Top panels: IR pump pulse spectra (solid gray lines) and FTIR spectra of both FA (dashed black lines) and solvent-subtracted FeRu (solid black lines). Cyanide stretching modes are indicated by dashed vertical lines as follows: ν_{trans} (2002.0 cm^{-1}, blue), ν_{radial} (2050.6 cm^{-1}, red), ν_{axial} (2065 cm^{-1}, green), and ν_{bridge} (2089.4 cm^{-1}, purple). Left panel: near-IR probe pulse spectrum (solid gray line) and linear electronic spectrum of FeRu in FA (solid black line). All linear (pulse) spectra are plotted in black (gray) to correspond with absorbance (intensity, Int.) axes. (a,b) Early waiting time 2D VE spectra of FeRu are dominated by vibrational mode-specific absorptions (blue) at ν_{trans} and ν_{bridge} as well as ν_{axial} modes, which lie on the charge-transfer axis of the molecule. (c-e) The sign of the ν_{bridge} mode signal oscillates, negative signal emerges at the perpendicular ν_{radial} mode, and a broad positive signal develops at the ν_{trans} mode. Panels (a-e) are normalized to (a). Each spectrum is plotted using contour lines at the following positions: ±0.025, ±0.05, ±0.1, ±0.2, ±0.35, ±0.5, ±0.65, ±0.8, ±0.95, and ±1.0.

The strengths and dynamics of individual ν_{CN} modes can be obtained from the 2D VE spectra presented in Figure 3-3. As a result of the multiple ν_{CN} modes in FeRu and the resolution in ω_1, the 2D VE FeRu spectra are more informative than the either the 2D VE $[Fe^{III}(CN)_6]^{3-}$ or 1D VE FeRu spectra. Initially, FeRu has a 2D VE signal dominated by ESA (negative) contributions in the ν_{trans} and ν_{bridge} modes, which are the two Raman active ν_{CN} modes in FeRu,[12] and a small contribution from the ν_{axial} mode (Figure 3-3(a) and (b)). Also, the signal from a combination mode, $\nu_{bridge+low}$, of coupled ν_{bridge} and low-frequency (17 cm^{-1}) modes is present in each spectrum with a sign opposite from that of the ν_{bridge} mode. Previously, the relative strengths of mode-specific vibronic coupling in FeRu were quantified by comparing two types of spectra at each ν_{CN} mode: 1.) an integrated projection of an early τ_2 2D VE spectrum with an area

proportional to $|\mu_{IR}|^2\left|\mu_{elec}^{eff}\right|^2$; 2.) the FTIR spectrum with an area under the line shape proportional to $|\mu_{IR}|^2$, where μ_{IR} is the amplitude of the IR-active transition dipole moment, **M** in Eq. (2).[3] The effective dipole moment, $\left|\mu_{elec}^{eff}\right|$, for the four ν_{CN} modes had the following trend at early τ_2 delays: $\nu_{bridge} > \nu_{trans} > \nu_{axial} >> \nu_{radial}$.[3] However at τ_2 = 300 fs (Figure 3-3(c)), the 2D VE signal appears much weaker for all ν_{CN} modes, which implies smaller $\left|\mu_{elec}^{eff}\right|$, and includes sign changes, which are especially notable in the positive amplitude at the ν_{bridge} mode. By τ_2 = 500 fs (Figure 3-3(d)), the ν_{bridge} mode signal returns to negative. This oscillation in τ_2 of the ν_{bridge} mode and also the $\nu_{bridge+low}$ mode 2D VE cross-peaks could arise from the coupling of two high frequency ν_{CN} modes; for example, the frequency separation of the ν_{bridge} and ν_{trans} modes corresponds to an oscillation period of ~380 fs. While the FeRu ν_{bridge} mode signal is negative starting at τ_2 = 500 fs, the final two 2D VE spectra contain clear GSB signals at the ν_{trans} mode (Figure 3-3(d-e)). This strong positive ν_{trans} mode signal can be explained by VER from a FeRu vibration to the solvent or potentially intramolecular vibrational relaxation (IVR). Using IR pump-probe spectroscopy, the Khalil group has measured the population decay of the ν_{trans} mode to be dominated by a relatively fast (~1 ps) component.[15] Thus, beginning before τ_2 = 1 ps in the 2D VE experiments, the initially excited ν_{trans} mode vibrational population relaxes to the ground state by transferring vibrational energy to FA molecules, which results in the reduction of the ESA signal. The positive 2D VE signal centered at the ν_{trans} mode excitation either grows in by τ_2 = 500 fs or is uncovered by the reduction of ESA. The long-lived GSB feature for the ν_{trans} mode could arise from IVR to Raman active modes in FeRu. The role of IVR from IR to Raman active modes has been previously studied in $[Fe^{II}(CN)_6]^{4-}$, where the measured timescale was within a few picoseconds.[16] Finally, the ν_{radial} mode appears to have a measurable $\left|\mu_{elec}^{eff}\right|$ with a negative feature in the τ_2 = 500

fs spectrum (Figure 3-3(d)). The lack of 2D VE signal initially at the ν_{radial} mode indicates the absence of coupling of the ν_{radial} mode either to the charge transfer or to another ν_{CN} mode. Therefore, the appearance of the peak at a later τ_2 delay is attributed to the transfer of energy between ν_{CN} modes, such as from the initially excited ν_{radial} mode to the ν_{bridge} mode, which displays a similar negative signal. This 500 fs delay matches the ν_{radial}–to-ν_{bridge} mode IVR timescale obtained from a fit of 2D IR spectral cross-peak (ν_{radial}, ν_{bridge}) amplitudes as a function of τ_2 for FeRu in FA.[15]

The evolution of correlations between vibrational modes and the MMCT transition in FeRu is determined by an analysis of 2D VE spectral line shapes and peak positions. The procedure for line shape analysis described in Section 3.1 is used to obtain the slopes, *m*, and ω_o positions for the ν_{trans} and ν_{trans} mode peaks in 2D VE FeRu spectra. These two quantities have greater variation over the series of τ_2 delays than do their counterparts in $[Fe^{III}(CN)_6]^{3-}$ 2D VE spectra. For the ν_{trans} mode, *m* is initially -0.003 (τ_2 = 50, 150 fs) and increases in magnitude to -0.004 (τ_2 = 300, 500 fs) before approaching 0 (magnitude <0.001) at τ_2 = 1000 fs. The ν_{bridge} mode has oscillatory behavior not only in the sign and magnitude of the 2D VE signal but also in the slope of the line shape: *m* = 0.002, 0.007, 0.003, and 0.007, at τ_2 = 50, 150, 300, and 500 fs, respectively, before approaching 0 (magnitude <0.001) at τ_2 = 1000 fs. Overall, the slopes report on the correlations of ν_{CN} modes with the MMCT transition. It is proposed that the ν_{bridge} mode has a positive correlation because the ν_{CN} stretch modulates the Fe-Ru separation and efficacy of charge transfer and that the ν_{trans} mode has a negative correlation due to the effects of the solvent-ν_{CN} interaction on the metal-ligand backbonding along Fe-CN-Ru.[3] The loss of correlation (*m* = 0) after 1 ps in the FeRu 2D VE spectra is not surprising given similar time constants for spectral diffusion in 2D IR

experiments with analogous IR excitation of high-frequency molecular vibrations in polar solvents.[17,18] The 2D VE peak positions have different trends with τ_2 in FeRu than in $[Fe^{III}(CN)_6]^{3-}$. After accounting for nonresonant 2D VE background signal,[3] the peak centers of the ν_{CN} modes in FeRu show little variation in ω_3 over τ_2. However, the peak centers tracked at a central ω_3 frequency (11500 cm^{-1}) do vary in ω_1 over the τ_2 delays shown in Figure 3-3. The ν_{trans} and ν_{bridge} modes initially have ω_o positions of 2014 cm^{-1} and 2085 cm^{-1}, respectively, before approaching the measured FTIR peak frequencies with loss of frequency correlation.

3.3 Distinction between resonant and nonresonant 2D VE signals: $[Fe^{II}(CN)_6]^{4-}$

Figure 3-1(b) displays the vibrational spectrum for $[Fe^{II}(CN)_6]^{4-}$ in FA (dashed black line) with a ν_{CN} = 2034.5 cm^{-1} mode that lies among the frequencies of the four ν_{CN} modes in FeRu. The Fe atom in each of these molecules is in the second oxidation state. Therefore, the mid-IR pump (ν_{MIR} ≈ 2050 cm^{-1}) and near-IR continuum probe ($\nu_{max\ near\text{-}IR}$ ≈ 11750 cm^{-1}) pulse spectra (Figure 3-1(b), solid gray lines) are the same as in the FeRu experiments. As mentioned in Section 3.1, $[Fe^{II}(CN)_6]^{4-}$ is the photoproduct of $[Fe^{III}(CN)_6]^{3-}$ and has no charge transfer transition. A previous ultrafast IR pump-probe study has shown that the VER timescales of $[Fe^{II}(CN)_6]^{4-}$ depend more strongly on solvent polarity and solvent isotope effects than those of $[Fe^{III}(CN)_6]^{3-}$.[2] The VER timescales of the Fe^{II} complex in FA are 4 times longer than the Fe^{III} complex in FA.[2] However, the lack of electronic transition in $[Fe^{II}(CN)_6]^{4-}$ and FA results in nonresonant VE spectroscopies that will be used to validate the preceding signals in resonant VE spectroscopies.

The VE spectra of $[Fe^{II}(CN)_6]^{4-}$ in FA are compared to spectra of neat FA and of FeRu, all with near-IR probe. First, the 1D VE spectra of $[Fe^{II}(CN)_6]^{4-}$ and neat FA match to within the signal-

to-noise limit of the measurement, i.e., to well below the 2.5% contour that differentiates $[Fe^{III}(CN)_6]^{3-}$ and neat FA 1D VE spectra in the visible probe region (Figure 3-2), as expected with a nonresonant probe field. Any additional nonresonant contribution from the excitation of the narrow (~17 cm^{-1} FWHM) ν_{CN} mode with peak OD of 0.40 (Figure 3-1(b)) is negligible compared to the excitation of the FA baseline (OD ≥ 0.19 across the entire pump spectrum). As seen in the $[Fe^{III}(CN)_6]^{3-}$ results (Section 3.1), the resolution of the excitation frequency axis in a 2D VE spectrum helps distinguish weak, mode-specific signals from a broad nonresonant background. Figure 3-4 presents the 2D VE spectra at τ_2 = 500 fs of FeRu (Figure 3-4(a)), $[Fe^{II}(CN)_6]^{4-}$ (Figure 3-4(b)), and neat FA (Figure 3-4(c)), all normalized to the Figure 3-4(a) spectrum. At τ_2 = 500 fs and at shorter waiting times, the 2D VE signal from $[Fe^{II}(CN)_6]^{4-}$ (centered at ν_{CN} = 2034.5 cm^{-1}) is at the same contour level as the FA signal. By τ_2 = 500 fs, the nonresonant $[Fe^{II}(CN)_6]^{4-}$ signal, while still centered at the ν_{CN} excitation frequency, is at the noise limit for reproducibility of the FA signal (Figure 3-4(c)): ~10% of the maximum of τ_2 = 500 fs FeRu (Figure 3-4(a)) or <2% of the maximum of τ_2 = 50 fs FeRu (Figure 3-3(a)). The narrow ν_{CN} bandwidth and long VER timescale of the $[Fe^{II}(CN)_6]^{4-}$ could cause the nonresonant signal to be longer lived than that of neat FA. Still, the ratio of 2D VE $[Fe^{II}(CN)_6]^{4-}$ signal to neat FA signal is well below a similar ratio for $[Fe^{III}(CN)_6]^{3-}$ and neat FA even though $|\mu_{IR}|^2$ is larger for $[Fe^{II}(CN)_6]^{4-}$. Therefore, the $\left|\mu_{elec}^{eff}\right|$ for $[Fe^{II}(CN)_6]^{4-}$ is found to be approximately zero, which confirms the necessity of coupled vibrational and electronic transitions for a meaningful VE spectroscopic signal.

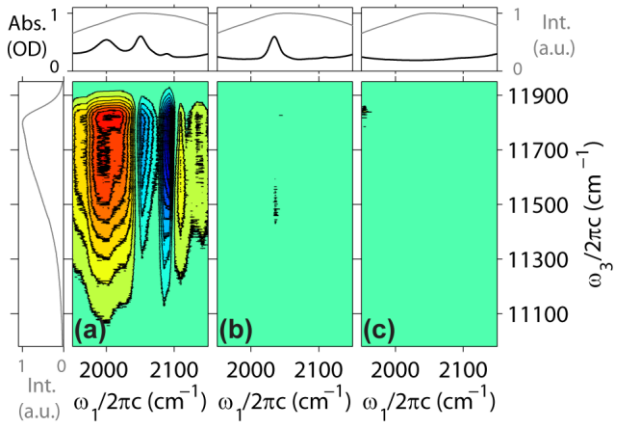

Figure 3-4 2D vibrational-electronic (VE) spectra at τ_2 = 500 fs. (a) $[(CN)_5Fe^{II}CNRu^{III}(NH_3)_5]^-$ (FeRu) dissolved in formamide (FA). (b) $[Fe^{II}(CN)_6]^{4-}$ dissolved in FA. (c) Neat FA. Each 2D VE spectrum has a panel above it with the IR pump pulse spectrum (gray lines) and the FTIR spectrum (including solvent) of the corresponding sample (black lines). Left panel: near-IR probe pulse spectrum (gray line). All linear (pulse) spectra are plotted in black (gray) to correspond with absorbance (intensity, Int.) axes. (b,c) The electronically nonresonant signals are aligned in ω_1 with absorptions from a broad FA baseline and a narrow cyanide stretching mode. (a) The fully resonant 2D VE FeRu signals are much stronger. Panels (a-c) are normalized to (a). Each 2D VE spectrum is plotted using contour lines at the following positions: ±0.1, ±0.2, ±0.3, ±0.4, ±0.5, ±0.6, ±0.7, ±0.8, ±0.9, and ±1.0.

3.4 Summary and Outlook

We have demonstrated the capabilities and versatility of 2D VE spectroscopy by measuring the vibronic coupling of high frequency stretching vibrations with either MMCT (near-IR) or LMCT (visible) optical transitions in the FeRu or $[Fe^{III}(CN)_6]^{3-}$ complex, respectively. Resulting 2D VE spectra contain cross-peaks localized to the charge transfer-coupled ν_{CN} mode in the ω_1 dimension. Similar but oppositely signed peaks arise in both molecules from combination modes of high and low frequencies, $\nu_{CN\pm low}$, that are coupled to the MMCT and LMCT transitions. Temperature-dependent 2D VE spectra may help to determine the roles of low-frequency modes in the following observed 2D VE spectral signatures: broadening in ω_3, presence of $\nu_{CN\pm low}$ mode signals, and oscillation in τ_2 of $[Fe^{III}(CN)_6]^{3-}$ peak maxima positions in ω_3 due to possible low-frequency mode coherences. The sign of each single, broad peak in ω_3 indicates the nonoverlapping contribution of the strongest transition (bleach or absorption) between vibrational states in the ground and electronic states within the frequency range accessible by the probe, which

is centered ~0.5 quantum (~1.5 quanta) to the blue of the LMCT (MMCT) transition. In future experiments, a scanning optical probe or one with increased bandwidth across the electronic transition over several quanta of a vibration should provide insight into the vibronic structure along ω_3. While the typical frequencies of vibrational anharmonicities and shift Δ_{eg} will cause significant cancellation of paired oppositely signed signals, the potential to resolve features at successive quanta of the vibration could help elucidate how Franck-Condon factors and non-Condon effects contribute to 2D VE peaks

2D VE spectroscopy enables the measurement of time-evolving mode-specific vibrational-electronic coupling strength and reports on vibrational-electronic frequency correlations, inter- and intramolecular vibrational relaxation, and vibrational mode coupling. The initial mode-specific electronic coupling strength in FeRu ($\nu_{bridge} > \nu_{trans} > \nu_{axial} \gg \nu_{radial}$) fluctuates over 1 ps due to coherences between ν_{CN} modes, the transfer of energy from the ν_{radial} to ν_{bridge} modes, and the energy transfer from the ν_{trans} mode to FeRu Raman modes or the solvent beginning at 500 fs. All frequency correlation in FeRu is lost by 1 ps, and no correlation is observed in $[Fe^{III}(CN)_6]^{3-}$ in the time resolution of this experiment. Further interpretation of these observations would benefit from a more complete understanding of whether vibrational and electronic frequencies interact with the same coupled bath modes of the polar solvent and the physical significance of correlated and uncorrelated frequency fluctuations of the vibrational and electronic frequencies. Performing the complementary 2D EV spectroscopy on these molecules should also be informative. Additionally, exploring the effect of 2D VE pump and probe polarizations on the strengths of individual modes or the solute-to-solvent signal ratio would be a useful exercise in determining the orientational response of the molecules.

In summary, the goal of this paper has been to detail the experimental implementation of a new third order nonlinear 2D spectroscopy and to show its selectivity for probing coupled vibrational and electronic motions. Given the interest in mapping energy flow among coupled vibrational and electronic degrees of freedom in natural and artificial light-harvesting phenomena, I expect 2D VE spectroscopy to have broad applications in the study of materials for photochemical energy conversion processes.

References

(1) Zhang, W.; Ji, M.; Sun, Z.; Gaffney, K. J. Dynamics of Solvent-Mediated Electron Localization in Electronically Excited Hexacyanoferrate(III). *J. Am. Chem. Soc.* **2012**, *134* (5), 2581–2588.

(2) Sando, G. M.; Zhong, Q.; Owrutsky, J. C. Vibrational and Rotational Dynamics of Cyanoferrates in Solution. *J. Chem. Phys.* **2004**, *121* (5), 2158–2168.

(3) Courtney, T. L.; Fox, Z. W.; Estergreen, L.; Khalil, M. Measuring Coherently Coupled Intramolecular Vibrational and Charge-Transfer Dynamics with Two-Dimensional Vibrational Electronic Spectroscopy. *J. Phys. Chem. Lett.* **2015**, *6* (7), 1286–1292.

(4) Kwak, K.; Park, S.; Finkelstein, I. J.; Fayer, M. D. Frequency-Frequency Correlation Functions and Apodization in Two-Dimensional Infrared Vibrational Echo Spectroscopy: A New Approach. *J. Chem. Phys.* **2007**, *127* (12).

(5) Kwak, K.; Rosenfeld, D. E.; Fayer, M. D. Taking Apart the Two-Dimensional Infrared Vibrational Echo Spectra: More Information and Elimination of Distortions. *J. Chem. Phys.* **2008**, *128* (20).

(6) Wang, C. F.; Mohney, B. K.; Akhremitchev, B. B.; Walker, G. C. Ultrafast Infrared Spectroscopy of Vibrational States Prepared by Photoinduced Electron Transfer in (CN)(5)FeCNRu(NH3)(5)(-). *J. Phys. Chem. A* **2000**, *104* (18), 4314–4320.

(7) Barbara, P. F.; Meyer, T. J.; Ratner, M. A. Contemporary Issues in Electron Transfer Research. *J. Phys. Chem.* **1996**, *100* (31), 13148–13168.

(8) Son, D. H.; Kambhampati, P.; Kee, T. W.; Barbara, P. F. Femtosecond Multicolor Pump-Probe Study of Ultrafast Electron Transfer of [(NH3)(5)(RuNCRuII)-N-III(CN)(5)](-) in Aqueous Solution. *J. Phys. Chem. A* **2002**, *106* (18), 4591–4597.

(9) Tominaga, K.; Kliner, D. A. V; Johnson, A. E.; Levinger, N. E.; Barbara, P. F. Femtosecond Experiments and Absolute Rate Calculations on Intervalence Electron-Transfer of Mixed Valence Compounds. *J. Chem. Phys.* **1993**, *98* (2), 1228–1243.

(10) Lynch, M. S.; Slenkamp, K. M.; Khalil, M. Communication: Probing Non-Equilibrium Vibrational Relaxation Pathways of Highly Excited C≡N Stretching Modes Following

Ultrafast Back-Electron Transfer. *J. Chem. Phys.* **2012**, *136* (24), 241101.

(11) Lynch, M. S.; Van Kuiken, B. E.; Daifuku, S. L.; Khalil, M. On the Role of High-Frequency Intramolecular Vibrations in Ultrafast Back-Electron Transfer Reactions. *J. Phys. Chem. Lett.* **2011**, *2* (17), 2252–2257.

(12) Wang, C. F.; Mohney, B. K.; Williams, R. D.; Petrov, V.; Hupp, J. T.; Walker, G. C. Solvent Control of Vibronic Coupling upon Intervalence Charge Transfer Excitation of (CN)(5)FeCNRu(NH3)(5)(-) as Revealed by Resonance Raman and near-Infrared Absorption Spectroscopies. *J. Am. Chem. Soc.* **1998**, *120* (23), 5848–5849.

(13) Doorn, S. K.; Dyer, R. B.; Stoutland, P. O.; Woodruff, W. H. Ultrafast Electron-Transfer and Coupled Vibrational Dynamics in Cyanide Bridged Mixed-Valence Transition-Metal Dimers. *J. Am. Chem. Soc.* **1993**, *115* (14), 6398–6405.

(14) Tivansky, A. V; Wang, C. F.; Walker, G. C. Vibrational Mode Coupling to Ultrafast Electron Transfer in [(CN)(5)OsCNRu(NH3)(5)](-) Studied by Femtosecond Infrared Spectroscopy. *J. Phys. Chem. A* **2003**, *107* (43), 9051–9058.

(15) Slenkamp, K. M.; Lynch, M. S.; Van Kuiken, B. E.; Brookes, J. F.; Bannan, C. C.; Daifuku, S. L.; Khalil, M. Investigating Vibrational Anharmonic Couplings in Cyanide-Bridged Transition Metal Mixed Valence Complexes Using Two-Dimensional Infrared Spectroscopy. *J. Chem. Phys.* **2014**, *140* (8).

(16) Ohta, K.; Maekawa, H.; Tominaga, K. Vibrational Population Relaxation and Dephasing Dynamics of Fe(CN)(6)(4-) in D2O with Third-Order Nonlinear Infrared Spectroscopy. *J. Phys. Chem. A* **2004**, *108* (8), 1333–1341.

(17) Ohta, K.; Tayama, J.; Saito, S.; Tominaga, K. Vibrational Frequency Fluctuation of Ions in Aqueous Solutions Studied by Three-Pulse Infrared Photon Echo Method. *Acc. Chem. Res.* **2012**, *45* (11, SI), 1982–1991.

(18) Brookes, J. F.; Slenkamp, K. M.; Lynch, M. S.; Khalil, M. Effect of Solvent Polarity on the Vibrational Dephasing Dynamics of the Nitrosyl Stretch in an Fe-II Complex Revealed by 2D IR Spectroscopy. *J. Phys. Chem. A* **2013**, *117* (29), 6234–6243.

Chapter 4

Implementation of Continuous Fast Scanning Detection in Femtosecond Fourier-Transform 2D VE Spectroscopy to Decrease Data Acquisition Time

The work presented in this chapter has been submitted for publication:

- *Fox, Z. W.; Blair, T. J.; Weakly, R. B.; Courtney, T. L; and Khalil, M., "Implementation of Continuous Fast Scanning Detection in Femtosecond Fourier-Transform Two-Dimensional Vibrational-Electronic Spectroscopy to Decrease Data Acquisition Time", Rev. Sci. Instr., **2018**, Submitted*

4.1 Introduction

Femtosecond two-dimensional (2D) Fourier transform (FT) spectroscopy is an invaluable tool in the modern day spectroscopist's toolbox. The ability to directly measure the coherent coupling between molecular degrees of freedom provides insight into the structural dynamics of complex biological, chemical and material systems.[1–4] Two-dimensional electronic spectroscopy (2D ES) has been used to understand electron delocalization and determine the energy transfer pathways in complex systems across many disciplines of study.[5–9] Similarly, 2D FT infrared (IR) spectroscopy has been used to study a range of molecular systems providing insight into vibrational energy transfer, structure-function relationships, and inter- and intra-molecular covalent interactions.[10–12] Recently, the next generation of 2D FT spectroscopies has been demonstrated, combining the vibrational and electronic regimes to look at the extreme cross peaks in the 2D FT spectroscopic landscape. The Fleming group introduced 2D electronic vibrational (2D EV) spectroscopy to directly observe the correlation between electronic state and molecular structure, using a pair of

optical pump pulses and probing the resulting nuclear motion.[13] The Khalil group has developed 2D vibrational-electronic (2D VE) spectroscopy to detect how vibrational motion effects charge transfer by probing how the electronic absorption of the system is modulated after excitation by a mid-IR (MIR) pump pair.[14] The wide applicability of the above-described 2D FT spectroscopies as reliable analytical tools hinges on being able to collect 10-100s of 2D spectra as a function of external stimuli (temperature, pH, time-delay, etc.) under the same experimental conditions. In most cases, data collection times are limited by the stability of the laser system. In this chapter, I describe a fast scanning 2D VE spectrometer, which allows for the collection of 2D spectra with a high signal-to-noise ratio (SNR) in less time.

Two-dimensional FT spectroscopies are third-order nonlinear experiments characterized by three field-matter interactions and the signal is detected in the correct phase-matched direction.[15,16] These experiments are characterized by three time delays, τ_1, τ_2 and τ_3 and the 2D spectrum is obtained by Fourier transforming the τ_1 and τ_3 delays to provide a map of coherently coupled frequencies as a function of ω_1 and ω_3. A commonly used geometry is the partially collinear pump-probe geometry where a pair of collinear pump beams intersect with a probe beam at the sample.[17–21] Beam-splitting optics are used to separate and recombine the pump pairs with a controlled delay between the two arms of the interferometer and the signal co-propagates with the probe beam. The delay between the pump beams (τ_1) is controlled by mechanically adjusting the effective difference in their path lengths, which provides the time domain axis that is Fourier transformed into the pump frequency axis, ω_1, in the final spectrum. Most 2D FT experiments employ multiplexed detection in the ω_3 dimension by using a spectrometer to effectively measure all the signal frequencies. Therefore, building the ω_1 axis is the main component contributing to the time required to collect high quality spectra.

Advances in femtosecond laser sources have allowed for building 2D FT spectrometers with repetition rates exceeding those of the conventional 1 kHz systems. There have been recent reports of collecting 2D spectra at 100 kHz where researchers can collect the same volume of data, but orders of magnitude faster.[22,23] Other methods of active modulation of the pump beams to generate the τ_1 axis efficiently include the use of pulse-shapers and novel phase-cycling schemes. Femtosecond pulse shapers in the UV and optical regimes have facilitated the development of 2D ES and 2D EV spectroscopy without the need for building interferometers for determining the ω_1 axis.[13,17,24–28] Though MIR pumps used in 2D IR spectroscopy do not lend themselves to pulse shaping as easily as the optical pumps of 2D ES, researchers are using similar pulse shaping techniques for 2D IR spectroscopy.[29,30] Even without direct pulse shaping of the MIR pump pulses, other time-saving techniques, such as fast scanning and compressed scanning, have been used to reduce the data collection time significantly in 2D FT IR experiments.[20,31,32]

Two-dimensional vibrational-electronic (2D VE) spectroscopy employs two MIR pump beams and a near IR probe beam entering the sample in a pump-probe geometry. The initial demonstration of 2D VE by Courtney et al. generated the τ_1 axis using the step scan method with a laser system running at 1 kHz.[14,33] In this method a mechanical delay stage is incrementally advanced with data corresponding to the current τ_1 value averaged over 2000 laser shots. Collecting one 2D VE spectrum with sufficient SNR using the step-scan method required ~ 13 hours. The low signal amplitude of 2D VE coupled with 4% RMS error in the near infrared (NIR) continuum used makes it difficult to collect a series of 2D VE spectra while keeping the laser conditions constant to eliminate experimental systematic errors. Instead of building the τ_1 axis by slowly stepping a mechanical stage, as described above, the stage can be continuously scanned hereby referred to as fast scanning (FS).[20,32] This method builds the complete τ_1 axis in seconds

while minimizing experimental and environmental changes. Not only does FS speed up the overall collection of data, but it also allows the researcher to collect data in an efficient manner, spending more time selectively averaging weaker signals. The use of collinear pumps in 2D VE allows a simple implementation of FS setup and complete control of individual pump beam characteristics, such as polarization and frequency.[19] In this work, the addition of FS to the existing 2D VE experiment combines ideas from similar FS 2D IR work,[20] but designed with the communication required for CCD detection. Much of the power of 2D VE spectroscopy is in the ability to separate the interactions between individual vibrational modes and delocalized electron motion. By successfully adding FS to 2D VE spectroscopy, more spectra parametrized by the waiting time (τ_2) can be collected in a single data run. This will allow the researcher to explore effects vibrational relaxation and couplings between high frequency and low frequency IR modes coupled to the same electronic transition.

In this chapter, the implementation of a FS detection scheme in a 2D VE experiment is presented along with modifications to the data collection and processing protocols. The improvement in data quality versus time gained by FS detection of 2D VE spectroscopy is characterized. The 2D VE experiments are performed on the mixed valence sample system, $[(CN)_5Fe^{II}\text{-}CN\text{-}Ru^{III}(NH_3)_5]^-$ (FeRu) dissolved in formamide, which has been previously studied using 2D IR and 2D VE spectroscopy.[14,34,35]

4.2 Experimental Setup

The schematic for this experiment is outlined in Figure 4-1. The basic layout for the 2D VE experiment has been given in detail in previously and is described here in brief.[33] A passively mode-locked Ti:Sapphire oscillator (Tsunami, Spectra Physics) pumped by a diode-pumped, frequency-doubled continuous wave Nd:YVO_4 laser (Millennia, Spectra Physics) is used to seed

a Ti:sapphire regenerative amplifier (Spitfire Pro XP, Spectra Physics) which is pumped by a diode-pumped, Q-switched, doubled Nd:YLF laser (Empower, Spectra Physics). The resulting 1 kHz pulsed output is spectrally centered at 800 nm with a 40 fs duration.

The MIR pump pulses are generated from difference frequency generation (DFG) of the NIR signal and idler outputs of an optical parametric amplifier (OPA 800C, Spectra Physics) in $AgGaS_2$ (United Crystal). Approximately 800 μJ of 800 nm light is sent into the OPA for conversion. The MIR light is sent through a Mach-Zehnder interferometer with a mechanically controlled delay stage (XMS50, Newport) to control the delay, τ_1 between MIR pulses. The two pulses are split and collinearly recombined using ZnSe beamsplitters (Rocky Mountain). The interferometer bright output (fully constructive at $\tau_1 = 0$) is finally routed to the sample area providing ~400 nJ per pump. The dark output (fully deconstructive at $\tau_1 = 0$) is collected with an amplified single channel Mercury Cadmium Telluride (MCT) detector (Infrared Systems). During experimentation, the mechanical stage is continuously scanned across the experimental range of τ_1 (-100 – 1400 fs) at 0.08 m/s.

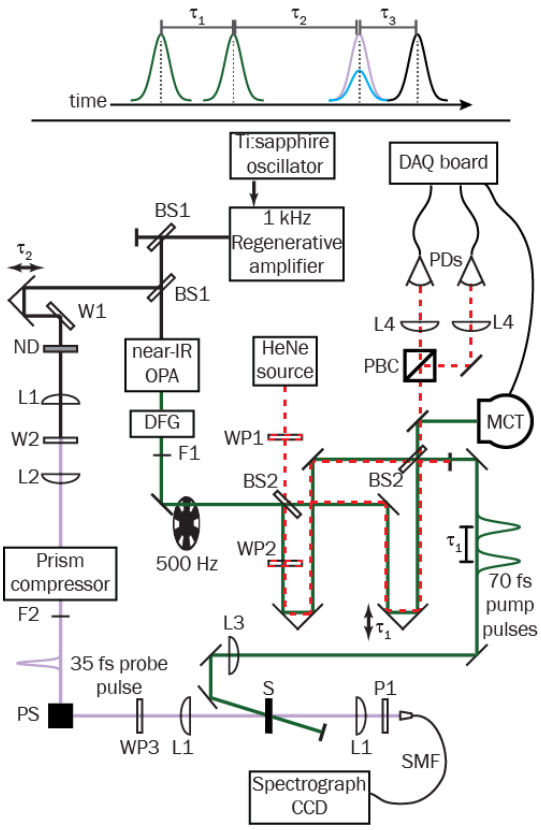

Figure 4-1 Experimental schematic. The laser pulse sequence for 2D VE. The two MIR pumps (green) are separated by τ_1, followed by the NIR probe (purple) after τ_2. The signal (blue) is emitted after with the probe, and by using the probe as the local oscillator (LO, black), τ_3 for this experiment is, by definition, 0 fs. Pulsed laser light is sourced from a titanium sapphire regenerative amplifier centered at 800 nm. The near-IR probe (purple) is created by focusing a slight reflection into a 3 mm thick sapphire window (W2). After the pulse is filtered and compressed, it is routed to the sample (S). The probe is collected in a single mode fiber (SMF) and routed to a spectrograph and CCD for detection. The pump pulse is generated via difference frequency generation (DFG) to give MIR light (green). The pump arm is chopped at 500 Hz and routed to a Mach-Zehnder interferometer with a controlled delay stage to vary the time between each individual pump pulse, τ_1. The waiting time between the pump and the probe pulses, τ_2, is controlled via a delay stage in the probe arm. The dark output of the interferometer is routed to a mercury cadmium telluride detector (MCT). The optical stage tracking uses a continuous wave HeNe laser (dashed red) polarized to 45° using a $\lambda/2$ waveplate (WP1). The tracking beam enters the same Mach-Zehnder interferometer as the pump, with the addition of a $\lambda/4$ waveplate (WP2) in one arm. The output of the tracking beam from the interferometer is used for quadrature detection in PDs. BS1: 800 nm dielectric beams splitter, BS2: 50:50 ZnSe beam splitter, F1: Ge filter; L1: fused silica (near-IR AR coated) plano-convex (PC) lens, f = 100 mm; L2: fused silica (near-IR AR coated) PC lens, f = 50 mm; L3: CaF_2 PC lens, f = 150 mm; L4: fused silica (Vis AR coated) PC lens, f = 50 mm.

The NIR continuum probe pulse is created by focusing <1 nJ 800 nm light into a 3 mm thick sapphire window (Newlight Photonics) before being routed through a fused silica prism compressor with a prism separation of 70 cm. The delay between the MIR pump and NIR continuum probe pulses is controlled with a long, mechanical, retroreflecting stage in the probe beamline (ILS150CC, Newport). After interaction with the sample, the probe is coupled into a

single-mode fiber (780HP, Thorlabs) and routed to a spectrograph (Shamrock 303i, Andor) outfitted with an 800 nm blazed grating (SR3-GRT-0600-0800, Andor, 600 grooves/mm) and CCD camera (Newport 970 EMCCD-UV, Andor). To achieve 1 kHz acquisition rate from the CCD, the active pixel range is restricted to 1600 × 15 pixels in full vertical bin mode which give the final 1600 × 1 experimental detection axis, ω_3. A sample of 20 mM FeRu dissolved in formamide is continuously flowed through a home-built flow cell with 1 mm thick CaF_2 windows. The optical pathlength between the two windows is 140 μm.

To implement fast scanning, another laser line must be added to the previously described 2D VE setup. For fast scanning 2D VE (FS 2D VE) a continuous wave (CW) Helium-Neon (HeNe) laser 632.8 nm (1137P, JDS Uniphase) is coupled into the Mach-Zehnder interferometer to track the instantaneous delay without relying on the relatively slow mechanical encoders in the delay stages. The HeNe follows the same path as the MIR (entering through the back of the first interferometer beam splitter, BS2, Figure 4-1) but offset vertically by approximately 2 cm center to center. All optics in the interferometer are shared between the MIR and HeNe beam paths providing an exact feedback of any pathlength variations within the interferometer. The 2" optics used within the interferometer provide enough space for the MIR (1 cm diameter) and HeNe (5 mm diameter) to use common optics with a vertical offset between the beams. Quadrature detection necessitates the addition of polarization optics into the interferometer. The incoming linearly polarized HeNe light is rotated 45º out of the vertical/horizontal lab reference frame using a $\lambda/2$ waveplate (05RP02-24, Newport) set to 22.5° before transmitting through BS2. A $\lambda/4$ waveplate (05RP04-24, Newport) is placed in one arm to generate circularly polarized light. The two arms are recombined on the same beam splitter as the MIR resulting in interference between them. The recombined beam is sent through a polarizing beamsplitter cube (PBS121, Thorlabs)

which separates S and P polarizations and their respective interference contributions. A pair of matched, reverse bias (2.5 V), Si photodiodes (DET10A, Thorlabs), (PDs) detect the resulting two beams. The two detected signals are collected simultaneously and in synchronization with the CCD camera using a DAQ board (USB-6356 BNC, National Instruments).

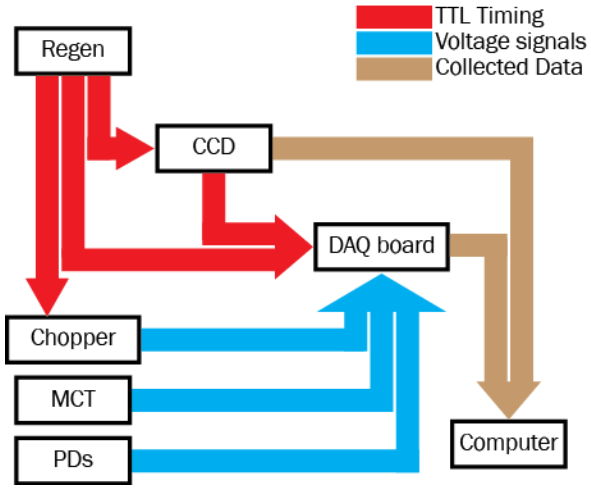

Figure 4-2 Data and communication flow. Digital TTL pulses (red) are used to synchronize the timing of all data taking devices with the laser output. Upon triggering from the CCD camera, the DAQ board reads the voltages from the chopper control, MCT detector, and both fast scanning photodiodes via coaxial connections (blue). The final collected data is sent to the control computer via a high-speed USB interface (brown).

In order to lock all devices to the repetition rate of the laser, outputs from the timing delay generator (TDG) from the regenerative amplifier are used to control the clocks of the chopper, CCD, and DAQ board. Each of these is controlled by a different TDG output which allows for fine tuning of the timing delay (in 1 ns steps) experienced by each device. Figure 4-2 shows how the communication channels are connected amongst all the instrumentation required for this setup. The two PDs and the MCT are analog detectors which continuously register signal as a change in voltage. Coaxial cables carry a live reading of this voltage to separate analog inputs on the DAQ board. To ensure simultaneous voltage sensing of the DAQ board, each input to the DAQ board must have a separate analog-to-digital converter. The chopper output is a square wave signal which indicates whether the chopper is open (high voltage, 5 V) or closed (low voltage, 0 V). This

information is received by a separate analog input on the DAQ board. More detailed discussion of the instrument timing and communication is found in Appendix B.

4.3 Data Processing

Upon the initializing of data collection, the CCD sends a TTL trigger pulse to the DAQ board to indicate that it has started to collect data. A set number of laser shots, normally 60,000 (1 minute acquisition), are collected consecutively by the CCD and stored in the camera's memory buffer. The number of shots collected at once is limited by the memory buffer in the CCD. The DAQ board collects the PD signals, chopper status, and IR intensity for each laser shot corresponding to those collected by the CCD. Once all 60,000 shots have been collected, the CCD and DAQ data are relayed to the computer via high speed USB for processing.

The data that are received by the computer contain the experimental spectroscopic information detected by the CCD as well as all of the individual shot parameters affecting that signal. Each CCD shot is indexed to the corresponding voltages for the chopper, MCT, and PDs. The time between the CCD trigger and the DAQ board beginning its acquisition has been experimentally determined to be 2 laser shots, which means that the first DAQ index corresponds to the third CCD index. Because this is a constant offset, the resulting data are adjusted accordingly by removing the first two CCD indices and the last two DAQ indices. After adjusting the indices of the data, a full workup of the data can be done automatically as outlined in Figure 4-3.

To determine the experimental τ_1 time for each laser shot, the PD signals must be treated as described below. The interference of the HeNe laser light detected by the PDs can be converted directly to distance as the period of the interference fringes defined by the HeNe wavelength (632.8

nm). A complete cycle of interference is therefore the result of the mechanical stage changing the beam pathlength by 632.8 nm (wavelength of the tracking HeNe beam), which translates to a 2.11 fs change in the experimental delay τ_1. In quadrature detection, the two photodiodes detect a sinusoidal HeNe interference pattern, 90º out-of-phase from one another.[36] The combination of two tracking beams with a known phase delay between them allows for more accurate and quicker determination of the distance traveled by the delay stage.[32] Plotting the PD signals against one another results in a circle which is fit in LabVIEW and used to determine the relative phase for each data point (see panel 2 of Figure 4-3). This phase is directly proportional to the distance traveled by the mechanical stage. The resolution of the distance traveled is limited to half cycles, or 1.055 fs. For MIR light centered at 2050 cm^{-1} this corresponds to approximately 1/16 of a period, providing sufficient resolution in the time domain. By binning the data into 180° increments, an evenly spaced selection of τ_1 points is created which can be directly Fourier transformed to generate the final ω_1 axis. This binning technique prevents any PD noise from having a large effect on the resulting stage timing. A bin counting system is used which determines whether the relative phase of the fit data crosses 0º or 180º and in what direction. The first shot is assigned a bin value of 0 and the following shots are changed by 0, +1, or -1 bins, depending on whether or not the phase moved into a new half cycle. For example, if the phase of adjacent shots goes from quadrant I (QI) to quadrant IV (QIV) (see Figure 4-3), the bin counter will determine there must have been a clockwise, 0º crossing, resulting in a decrease in the bin value by 1 between shots. If the phase of adjacent shots goes from QIV to QIII, then there will be no change in bin value between the two shots. A more detailed explanation of the LabVIEW code used to collect and bin the data can be found in Section C.1. Once each shot is analyzed, an indexed vector of bins is available detailing the τ_1 position for each laser shot. Once bins have been assigned to

every shot, all shots that fall within the same bin are averaged together. To generate the final τ_1 assignment for the averaged bins the conversion factor of 1.055 fs/bin is applied. This conversion factor is the time associated with half a cycle of HeNe 632.8 nm light.

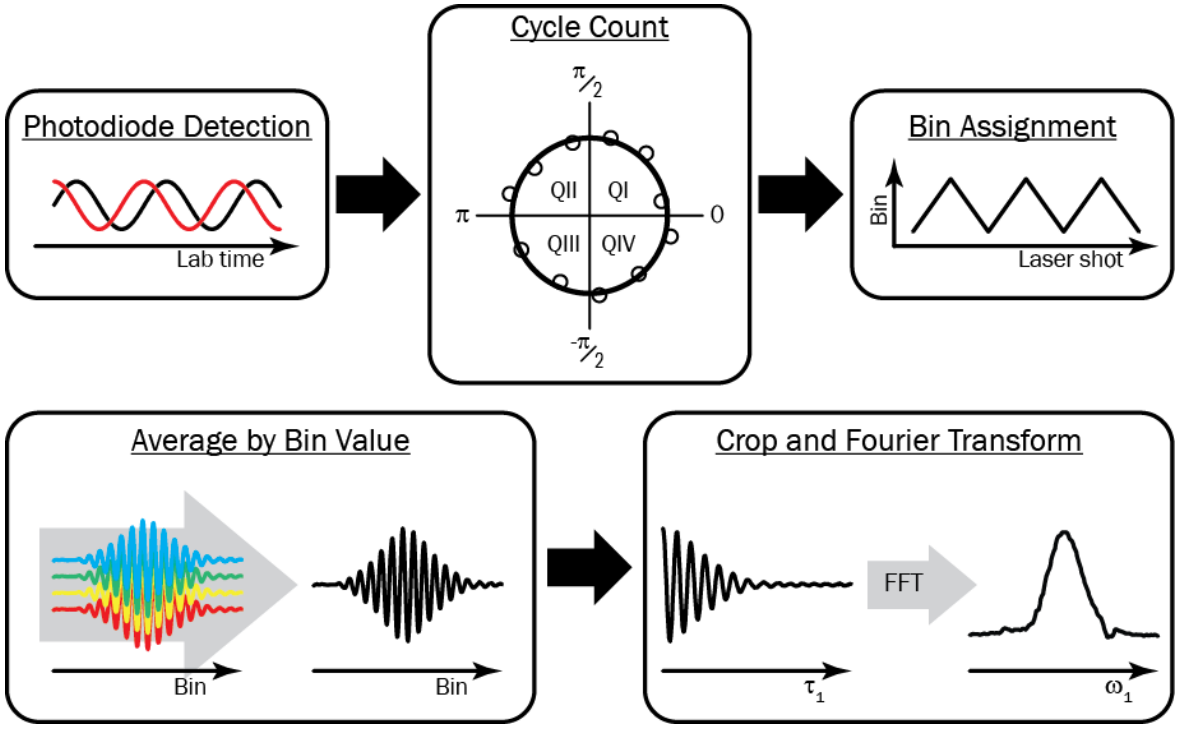

Figure 4-3 Data processing flow chart. The tracking PDs collect the real time movement of the mechanical stages as they move. The combined quadrature signal from the PDs is used to calculate the phase difference between adjacent shots. Shots falling within the bins defined by [0:π) and [π:2 π) are averaged together. Because the sign of the relative phase is known, the direction of the stage is also known allowing for continuous scanning back and forth through the region of interest in τ_1. After data has been collected, all laser shots in bins of the same value are averaged together. Using the inteferogram of the pump pulses collected in the MCT, all data at $\tau_1 < 0$ is discarded and the asymmetric FFT is performed. The resulting frequency domain data is used to build ω_1 in the 2D VE spectrum.

In order for further analysis to be performed, the bin associated with $\tau_1 = 0$ fs, t_0, must be determined. The minimum of the interferometer dark output MCT data is used as the measure for t_0 because it corresponds to the maximum VE signal amplitude associated with the pump interference being fully constructive in the bright output. To enforce proper order of the pump pulses, any bin values that correspond to $\tau_1 < 0$ fs are removed. This also ensures that the second pump pulse does not enter the waiting time, τ_2. The resulting half interferograms are zero padded

from approximately 1500 to 4096 points and undergo a fast Fourier transform (FFT). Only the real part of the FFT result is kept as the imaginary component is an artifact leftover from the asymmetric nature of the input data. The final spectrum is the result of multiple scans of the same τ_2 delay, which are worked up and combined while taking data until the time domain averaging results in a sufficient SNR. Outline of the MATLAB code used to work up the final data can be found in Section C.2.

The SNRs are calculated by comparing the one-sided power spectral density (PSD) of the signal and noise regions of ω_1. The PSD is defined as: $PSD(\omega) = S(\omega)^2$, where $0 < \omega < \omega_{\text{Nyquist}}$, and $S(\omega)$ is the frequency domain spectrum obtained via FFT as described above. In these experiments, with 1.055 fs time steps, $\omega_{\text{Nyquist}} = 4.73$ THz. The signal region is determined to be the frequencies that show clear 2D VE response, and the noise region is all other frequencies beyond the DC component not included in the signal region (see Figure 4-4). The SNR calculation uses the power density of the signal and noise regions defined as:

$$P = \frac{1}{\Delta\omega}\int PSD(\omega)d\omega \tag{4.1}$$

This gives the average power for a given region. The SNR is reported as the decibel difference between the signal and noise power density:

$$\frac{S}{N}\,10\log_{10}\left(\frac{P_{signal}}{P_{noise}}\right) \tag{4.2}$$

All SNRs are calculated at the peak of the FeRu response along the CCD detection frequency, $\omega_3 = 11534$ cm^{-1}.

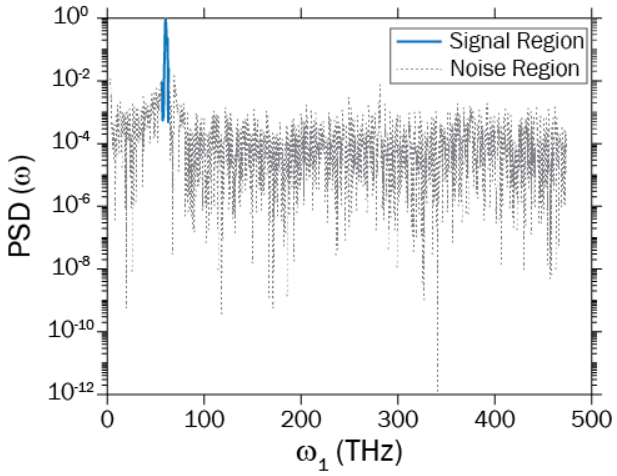

Figure 4-4 PSD for FS 2D VE. The signal region (blue solid line) is selected to best represent the expected signal for the 2D VE experiment. The noise region (grey dotted line) includes all data not in the signal region and above the DC component of the FFT (not shown). The PSD is calculated at the peak of the FeRu response along the CCD detection frequency, $\omega_3 = 11534$ cm^{-1}.

4.4 Results

When traditional step scanning is used to collect any kind of interferometric signal, the loss of correlation between adjacent laser shots means that each individual time point along the interferogram should be thought of as an independent experiment with no memory of the previous time point. In each of the step scanning experiments, a single data point is averaged for 2 seconds before the stage is stepped to the next time point. The movement of the stage, and equilibration add another second to collection time for each time step. Because the laser conditions continually drift, comparing individual steps becomes less significant. This effect shows up in the noise levels

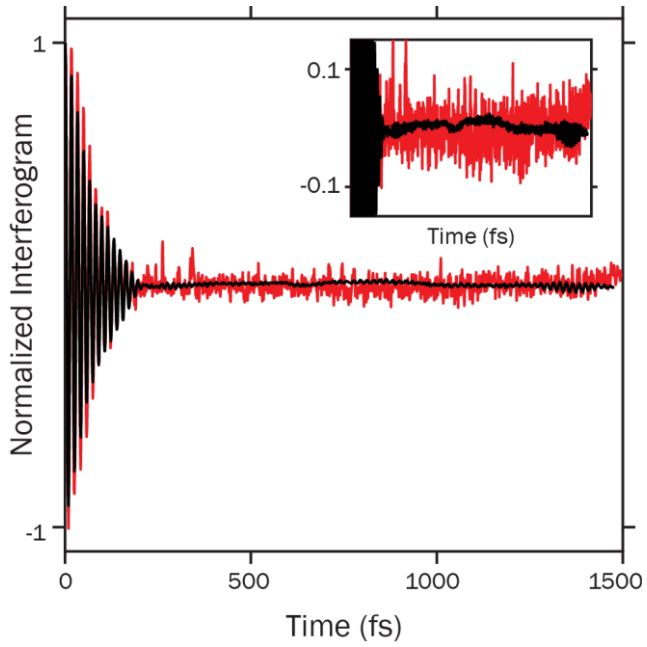

Figure 4-5 Noise comparison between fast scanned IR interferogram (black) and step scanned IR interferogram (red) collected in an integrated MCT detector. The interferogram of this pump pair is used to determine $\tau_1 = 0$ during data processing. The effects of laser instability over long time periods and general drift result in significantly higher noise in measured pump power which shows up as noise in the final 2D VE spectrum. The drift experienced by the laser over the course of a full step scan is nearly 10% of the IR intensity (inset) and results in a 2.5 dB difference in SNR between the two collection methods.

of the detected signals. In comparison, fast scanning allows an entire interferometric scan to be completed within 2 seconds and a higher level of correlation is maintained throughout the scan. A comparison of the noise levels of an IR interferogram, shown in Figure 4-5, clearly shows a reduction in the noise level at the edges of the scan despite the two order of magnitude reduction in the number of shots being used in the collection of the signal. The quantitative reduction in noise is reported in Table 4-1, demonstrating that by collecting data quickly in the FS scheme increases the SNR by 3 dB.

Table 4-1 Comparison of SNRs and laser shots of fast scanned and step scanned experiments.

Experiment	*2D VE*[a]			*IR Interferogram*	
Detection Method	FS (1 min)	FS (1 hr)	SS (13 hr)	FS (1 min)	SS (40 min)
#Total Shots	60,000	3,600,000	26,880,000	60,000	1,100,000
SNR (dB)	11.8[b]	26.1[b]	28.9[b]	31[c]	28.6[c]

[a] *Calculated at detection frequency ω_3 = 11534 cm^{-1}*
[b] *signal bandwidth, $\Delta\omega$ = 19 THz*
[c] *signal bandwidth, $\Delta\omega$ = 27 THz*

The 2D VE experiment directly probes the coupling between excited vibrational modes and an electronic transition. In the case of FeRu dissolved in formamide, the vibrational modes associated with the C≡N stretches have been shown to couple to the electronic transition associated with a metal-to-metal charge transfer (MMCT) from the iron to the ruthenium using various spectroscopic methods.[37,38] In formamide, the C≡N vibrations show 4 distinct modes in the FTIR spectrum (see Figure 4-6). The four modes, trans (ν_t, 2002 cm^{-1}), radial (ν_r = 2050 cm^{-1}), axial (ν_a = 2064 cm^{-1}) and bridging (ν_b = 2089 cm^{-1}), are anharmonically coupled to one another as detailed in 2D IR experiments.[34] Using 2D VE spectroscopy, the mode-specific vibronic coupling strengths between each of the C≡N vibrations and the MMCT transition were determined previously using the step-scan method to generate the τ_1 axis. It was shown that the bridging C≡N vibration couples most strongly to the MMCT transition.[14,33]

The results of the FS 2D VE shown in Figure 4-6, are consistent with previous experiments described above. The 2D VE spectra shown in Figure 4-6 show a clear, negative, excited state absorption (ESA) feature, corresponding to frequencies in ω_1 associated with the ν_{trans} and ν_{bridge} C≡N modes of FeRu as shown in the FTIR spectra above each 2D VE panel. The primary goal of fast scanning implementation is to reduce the data collection time. Even after a minimal collection time of 1 minute, spectral features begin to resolve (Figure 4-6(a)). After 60 minutes of FS data collection (Figure 4-6(b)), the 2D VE spectrum is similar to that of a step scanned (SS) data set

(Figure 4-6(c)). However, the SS is a result of 7 averages which each take ~110 minutes each (13 hours total). In summary, FS is able to collect data of similar quality to SS in a fraction of the time. Additionally, the ability to work up the FS data as it is being collected means that data must only be collected until the desired quality of data has been reached. This allows the experimentalist to move on to other τ_2 points more quickly, reducing the time wasted by over-averaging data at each time point.

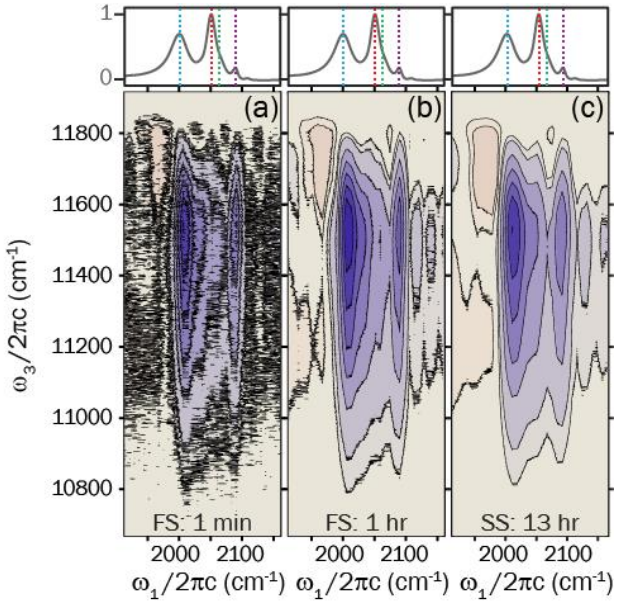

Figure 4-6 Normalized experimental 2D VE of FeRu at τ_2 = 260 fs using different spectroscopic techniques with FeRu. FTIR for reference (top panels). The colored dashed lines (blue, red, green, and purple) correspond to the peak centers for the ν_{CN} modes ν_t, ν_r, ν_a, and ν_b respectively. Comparison of 1 minute of FS-2D VE (a), 60 minutes of FS-2D VE (b), and 780 minutes of SS 2D VE (c). The general shape of the spectrum can be seen even after 1 minute of data collection and continued acquisition increases the SNR to a similar degree that the step scanning can achieve in less than 1/10th the time. Contour lines for all spectra at: ±0.05, ±0.1, ±0.25, ±0.40, ±0.55, ±0.70, ±0.85, ±1.0.

4.5 Conclusions

This work demonstrates a successful fast scanning incorporation into 2D VE spectroscopy using a molecular sample of experimental interest, while confirming previously published results. Here, CCD detection is successfully combined with fast scanning while tracking the delay of MIR light. This method not limited to 1 kHz rep rate laser systems and can be integrated into any experiment which uses mechanical stages to control laser delay regardless of the rep rate of the

system. The increased speed of the experiment carries with it the added benefit of increasing SNR by performing the entire experiment within the window of high shot-to-shot laser correlation. The flexibility in data collection allows for efficiency without a loss of quality by focusing data collection time of weaker signals and provides quick feedback while optimizing experimental parameters.

Fast scanning is a significant improvement to the 2D VE experiment as the decreased experiment time without loss in data quality expand what can be accomplished in an experiment. The increased speed of data acquisition will allow future studies to use this powerful technique in greater detail. Data acquisition time is only dependent on the SNR level, which allows the researcher to most efficiently use their time during experimentation. As such, the researcher can monitor samples over many time points or take multiple polarization sensitive measurements in a short amount of time. In addition, automated data processing provides extremely quick feedback which gives the possibility of live monitoring of the experiment as it happens. Fast scanning can be assimilated into many detection schemes with limited adaptation while addressing many of the challenges associated with multidimensional spectroscopy: large data collection times, small SNR, and limited feedback during experimentation.

References

(1) Mukamel, S. Multidimensional Femtosecond Correlation Spectroscopies of Electronic and Vibrational Excitations. *Annu. Rev. Phys. Chem.* **2000**, *51*, 691–729.

(2) Cho, M. Coherent Two-Dimensional Optical Spectroscopy. *Chem. Rev.* **2008**, *108* (4), 1331–1418.

(3) Jonas, D. M. Two-Dimensional Femtosecond Spectroscopy. *Annu. Rev. Phys. Chem.* **2003**, *54*, 425–463.

(4) Kraack, J. P.; Hamm, P. Surface-Sensitive and Surface-Specific Ultrafast Two-Dimensional Vibrational Spectroscopy. *Chem. Rev.* **2017**, *117* (16).

(5) Hybl, J. D.; Albrecht, A. W.; Gallagher Faeder, S. M.; Jonas, D. M. Two-Dimensional

Electronic Spectroscopy. *Chem. Phys. Lett.* **1998**, *297*, 307–313.

(6) Cowan, M. L.; Ogilvie, J. P.; Miller, R. J. D. Two-Dimensional Spectroscopy Using Diffractive Optics Based Phased-Locked Photon Echoes. *Chem. Phys. Lett.* **2004**, *386* (1–3), 184–189.

(7) Brixner, T.; Stiopkin, I. V; Fleming, G. R. Tunable Two-Dimensional Femtosecond Spectroscopy. *Opt. Lett.* **2004**, *29* (8), 884–886.

(8) Tian, P. F.; Keusters, D.; Suzaki, Y.; Warren, W. S. Femtosecond Phase-Coherent Two-Dimensional Spectroscopy. *Science (80-.).* **2003**, *300* (5625), 1553–1555.

(9) Borca, C. N.; Zhang, T. H.; Li, X. Q.; Cundiff, S. T. Optical Two-Dimensional Fourier Transform Spectroscopy of Semiconductors. *Chem. Phys. Lett.* **2005**, *416* (4–6), 311–315.

(10) Asplund, M. C.; Zanni, M. T.; Hochstrasser, R. M. Two-Dimensional Infrared Spectroscopy of Peptides by Phase-Controlled Femtosecond Vibrational Photon Echoes. *Proc. Natl. Acad. Sci. U. S. A.* **2000**, *97* (15), 8219–8224.

(11) Khalil, M.; Demirdöven, N.; Tokmakoff, A. Coherent 2D IR Spectroscopy: Molecular Structure and Dynamics in Solution. *J. Phys. Chem. A* **2003**, *107* (27), 5258–5279.

(12) Asbury, J. B.; Steinel, T.; Stromberg, C.; Gaffney, K. J.; Piletic, I. R.; Fayer, M. D. Hydrogen Bond Breaking Probed with Multidimensional Stimulated Vibrational Echo Correlation Spectroscopy. *J. Chem. Phys.* **2003**, *119* (24), 12981–12997.

(13) Oliver, T. A. A.; Lewis, N. H. C.; Graham, R. Correlating the Motion of Electrons and Nuclei with Two-Dimensional Electronic–vibrational Spectroscopy. *Proc. Natl. Acad. Sci.* **2014**, *111* (28), 10061–10066.

(14) Courtney, T. L.; Fox, Z. W.; Estergreen, L.; Khalil, M. Measuring Coherently Coupled Intramolecular Vibrational and Charge-Transfer Dynamics with Two-Dimensional Vibrational-Electronic Spectroscopy. *J. Phys. Chem. Lett.* **2015**, *6*, 1286–1292.

(15) Cho, M. *Two-Dimensional Optical Spectroscopy*; CRC Press: Boca Raton, 2009.

(16) Mukamel, S. *Principles of Nonlinear Optic and Spectroscopy*; Oxford University Press: New York, 1995.

(17) Grumstrup, E. M.; Shim, S.-H.; Montgomery, M. A.; Damrauer, N. H.; Zanni, M. T. Facile Collection of Two-Dimensional Electronic Spectra Using Femtosecond Pulse-Shaping Technology. *Opt. Express* **2007**, *15* (25), 16681–16689.

(18) Myers, J. A.; Lewis, K. L. M.; Tekavec, P. F.; Ogilvie, J. P. Two-Color Two-Dimensional Fourier Transform Electronic Spectroscopy with a Pulse-Shaper. *Opt. Express* **2008**, *16* (22), 17420–17428.

(19) DeFlores, L. P.; Nicodemus, R. A.; Tokmakoff, A. Two Dimensonal Fourier Transform Spectroscopy in the Pump-Probe Geometry. *Opt. Lett.* **2007**, *32* (20), 2966–2968.

(20) Helbing, J.; Hamm, P. Compact Implementation of Fourier Transform Two-Dimensional IR Spectroscopy without Phase Ambiguity. *J. Opt. Soc. Am. B* **2011**, *28* (1), 171–178.

(21) Courtney, T. L.; Park, S. D.; Hill, R. J.; Cho, B.; Jonas, D. M. Enhanced Interferometric Detection in Two-Dimensional Spectroscopy with a Sagnac Interferometer. *Opt. Lett.* **2014**, *39* (3).

(22) Kearns, N. M.; Mehlenbacher, R. D.; Jones, A. C.; Zanni, M. T. Broadband 2D Electronic Spectrometer Using White Light and Pulse Shaping : Noise and Signal Evaluation at 1 and 100 KHz. *Opt. Express* **2017**, *25* (7), 1169–1173.

(23) Luther, B. M.; Tracy, K. M.; Gerrity, M.; Brown, S.; Krummel, A. T. 2D IR Spectroscopy at 100 KHz Utilizing a Mid-IR OPCPA Laser Source. *Opt. Express* **2016**, *24* (4).

(24) Senlik, S. S.; Policht, V. R.; Ogilvie, J. P. Two-Color Nonlinear Spectroscopy for the Rapid Acquisition of Coherent Dynamics. *J. Phys. Chem. Lett.* **2015**, *6* (13).

(25) Guo, L.; Monahan, D. M.; Fleming, G. Rapid and Economical Data Acquisition in Ultrafast Frequency-Resolved Spectroscopy Using Choppers and a Microcontroller. *Opt. Express* **2016**, *24* (16), 18126–18132.

(26) Son, M.; Mosquera-Vázquez, S.; Schlau-Cohen, G. S. Ultrabroadband 2D Electronic Spectroscopy with High-Speed, Shot-to-Shot Detection. *Opt. Express* **2017**, *25* (16), 18950–18962.

(27) Harel, E.; Fidler, A. F.; Engel, G. S. Single-Shot Gradient-Assisted Photon Echo Electronic Spectroscopy. *J. Phys. Chem. A* **2011**, *115* (16), 3787–3796.

(28) Turner, D. B.; Stone, K. W.; Gundogdu, K.; Nelson, K. A. Three-Dimensional Electronic Spectroscopy of Excitons in GaAs Quantum Wells. *J. Chem. Phys.* **2009**, *131* (14).

(29) Shim, S.-H.; Strasfeld, D. B.; Ling, Y. L.; Zanni, M. T. Automated 2D IR Spectroscopy Using a Mid-IR Pulse Shaper and Application of This Technology to the Human Islet Amyloid Polypeptide. *Proc. Natl. Acad. Sci. U. S. A.* **2007**, *104* (36), 14197–14202.

(30) Nite, J. M.; Cyran, J. D.; Krummel, A. T. Active Bragg Angle Compensation for Shaping Ultrafast Mid-Infrared Pulses. *Opt. Express* **2012**, *20* (21), 23912–23920.

(31) Dunbar, J. A.; Osborne, D. G.; Anna, J. M.; Kubarych, K. J. Accelerated 2D-IR Using Compressed Sensing. *J. Phys. Chem. Lett.* **2013**, *4*, 2489–2492.

(32) Roberts, S. T.; Loparo, J. J.; Ramasesha, K.; Tokmakoff, A. A Fast-Scanning Fourier Transform 2D IR Interferometer. *Opt. Commun.* **2011**, *284*, 1062–1066.

(33) Courtney, T. L.; Fox, Z. W.; Slenkamp, K. M.; Khalil, M. Two-Dimensional Vibrational-Electronic Spectroscopy. *J. Chem. Phys.* **2015**, *143* (15), 154201.

(34) Slenkamp, K. M.; Lynch, M. S.; Kuiken, B. E. Van; Brookes, J. F.; Bannan, C. C.; Daifuku, S. L.; Khalil, M. Investigating Vibrational Anharmonic Couplings in Cyanide-Bridged Transition Metal Mixed Valence Complexes Using Two-Dimensional Infrared Spectroscopy Investigating Vibrational Anharmonic Couplings in Cyanide-Bridged Transition Metal Mixed Valence Complex. *J. Chem. Phys.* **2014**, *140*, 084505.

(35) Slenkamp, K. M.; Lynch, M. S.; Brookes, J. F.; Bannan, C. C.; Daifuku, S. L.; Khalil, M. Investigating Vibrational Relaxation in Cyanide-Bridged Transition Metal Mixed-Valence

Complexes Using Two-Dimensional Infrared and Infrared Pump-Probe Spectroscopies. *Struct. Dyn.* **2016**, *3* (2).

(36) Downs, M. J.; Raine, K. W. An Unmodulated Bi-Directional Fringe-Counting Interferometer System for Measuring Displacement. *Precis. Eng.* **1979**, 85–88.

(37) Wang, C.; Mohney, B. K.; Akhremitchev, B. B.; Walker, G. C. Ultrafast Infrared Spectroscopy of Vibrational States Prepared by Photoinduced Electron Transfer in (CN)5FeCNRu(NH3)5-. *J. Phys. Chem. A* **2000**, *104* (18), 4314–4320.

(38) Wang, C. F.; Mohney, B. K.; Williams, R. D.; Petrov, V.; Hupp, J. T.; Walker, G. C. Solvent Control of Vibronic Coupling upon Intervalence Charge Transfer Excitation of (CN)(5)FeCNRu(NH3)(5)(-) as Revealed by Resonance Raman and near-Infrared Absorption Spectroscopies. *J. Am. Chem. Soc.* **1998**, *120* (23), 5848–5849.

Chapter 5

Polarization Selective 2D VE Spectroscopy to Distinguish Orientational Response from Vibronic Coupling in an Intramolecular Charge-Transfer Complex

The work presented in this chapter is being prepared for publication:

- *Fox, Z. W.; Blair, T. J.; Leger, J.; Weakly, R. B.; and Khalil, M., "Polarization Selective 2D Vibrational Electronic Spectroscopy to Distinguish Orientation Response from Vibronic Coupling in an Intramolecular Charge-Transfer Complex", J. Chem. Phys. Lett.,* ***2018****, In preparation*

Energy transfer within molecules is a multifaceted process which includes coupling between vibrational and electronic motion on an ultrafast timescale that is difficult to probe. Directly probing the coupling behavior that drives energy transfer in molecules and materials is the best way to develop a strong understanding of the many different underlying processes involved. As multidimensional techniques such as 2D electronic and 2D infrared (IR) spectroscopies become commonplace in the ultrafast community, complex problems such as energy transfer mechanisms in light harvesting materials and semiconductors, or the molecular dynamics in hydrogen bonded system can be understood better than ever before.[1–5] With the development of 2D electronic-vibrational (EV) and 2D vibrational-electronic (VE) spectroscopies, the direct observation of coupling between vibrational and electronic motion has become possible in multidimensional coherent spectroscopies, opening the doors to a better understanding of correlated motion within important biological and materials systems.[6,7]

The next step towards disentangling the complex signals that arise from 2D VE spectroscopy is to distinguish between the enhancement of vibrational modes that arises from orientational dependence and contributions of the transition dipoles dependent on vibronic coupling.[8] The metal-to-metal charge transfer (MMCT) compound $[(CN)_5Fe^{II}–CN–Ru^{III}(NH_3)_5]^-$ (FeRu) provides an excellent case to demonstrate the power of 2D VE when both strong vibronic coupling and an orientationally dependent response combines to make quantitative interpretation of 2D spectra difficult. The modulation of the MMCT by the cyanide stretching vibrations (ν_{CN}) has been demonstrated in previous publications by this group, but without the ability to separate the orientational effects from the extreme angles found within the structure of FeRu. While the MMCT is necessarily oriented between the two metal centers of the molecule, not all ν_{CN} modes are in line with this transition dipole. In fact, the ν_{CN} modes range from near parallel to near perpendicular.[9] By using polarization selective methods the true extent of vibronic coupling can be elucidated as well as the angles between the transitions being studied, something previously only studied directly in 2D spectroscopies with polarization selective 2D EV.[10,11]

5.1 Response Function Model and Fitting Routine

The 2D VE experiment presented here is similar to those previously reported by this group, using a pair of mid-IR (MIR) pumps, separated by the vibrational coherence, τ_1, to excite the sample followed, after a waiting time, τ_2, by a noncollinear near-IR (NIR) probe.[6] By using the pump-probe geometry, both rephrasing (R) and nonrephasing (NR) third-order signals will copropagate with the probe, which acts as a local oscillator (LO), and the fully absorptive 2D VE signal is detected.[12–14] Previous work has not included polarization control over the pump and probe pulses.[6,15] With polarization control, each light matter interaction can be controlled in the laboratory frame. Here, by selecting the signals resulting from polarization specific interactions

of the pump and probe with the sample, both fully parallel (ZZZZ) and crossed (ZZYY) experiments are undertaken at the same τ_2 in order to determine the orientational response of the FeRu sample in formamide (FA).

As previous experiments have demonstrated, the expected 2D VE signal at this probe frequency is negative which is indicative of an excited state absorption (ESA) pathway.[15] Each vibrational mode coupled to the MMCT will be separated along the experimental ω_1 axis (horizontal) because of the different frequencies associated with the absorbance of MIR light. The third-order signal is not only dependent on the resonant MIR excitation, but also on the electronic excitation which results from the vibrationally excited samples interaction with the resonant NIR probe. The amplitudes of the detected signal will be modified by how strongly interacting the sample is to each impinging light pulse as well as the relative dipole orientation to the electric field of the incoming light.[16,17] When the electric field is projected onto the molecular transition dipole, any deviation from parallel will reduce the effective electric field magnitude. Without explicitly accounting for polarization dependence, the relative importance of these two effects is not clear. This work uses a model response function, based on Bloch formalism, dependent on both the magnitude of the individual dipole transitions as well as the derived orientational response functions.[17] The collected absorptive experimental data is fit to a simulated spectrum calculated from the time domain response function to extract physically meaningful quantitative measurements of FeRu using polarization dependent 2D VE.

To simplify the fitting procedure, only those Louiville pathways associated with an ESA involving a single IR transition were included, and dynamics arising from the τ_2 were ignored. The time domain response function followed the general form, demonstrated by the ESA, R response function:

$$R_{ESA,R}(\tau_1,\tau_3) = -\mu_{IR}^2\,\mu_{IR,e}^2\;\mathrm{Y}_{IJKL}(\theta_{IR,e})\exp\left(\frac{-i\omega_{IR}}{2\pi}\tau_1 - \Gamma_{IR}\tau_1\right)\exp\left(\frac{-i\omega_e}{2\pi}\tau_3 - \Gamma_e\tau_3\right) \quad (5.1)$$

In this model, the dipole moment of the vibrational transition, μ_{IR}, the effective electronic dipole moment after vibrational excitation, $\mu_{\mathrm{IR,elec}}$, which includes the transition dipole moment, Frank-Condon factors, and non-Condon effects, and the orientational response function $Y_{IJKL}(\theta_{IR,elec})$ are responsible for the amplitude of each transition fit. The parameters associated with the orientational response function are the polarization components of the time ordered sequence of light matter interactions, dependent on the angle between the excited IR transition dipole and the electronic transition dipole. The frequency centers of each IR transition, ω_{IR}, and the electronic transition, ω_{elec}, correspond to peaks centered on ω_1 and ω_3, respectively, after a Fourier transform. Finally, the exponential decay component Γ, is the width of the resulting Lorentzian lineshape in the frequency domain upon Fourier transform. The resulting time domain response functions were fast Fourier transformed along both τ_1 and τ_2 to generate the frequency axes ω_1 and ω_3, respectively. The R and NR components are added together to generate a fully absorptive simulation spectrum. The simulated data was splined to match the experimental axis and both spectra were cropped to the region of interest in both ω_1 and ω_3. To reduce the parameter space sampled during a fitting routine, the vibrational linewidths as well as angles between individual vibrational modes from previously published FTIR and 2D IR work on FeRu were used.[9] The three vibrational modes fit in this paper correspond to the ν_{trans}, ν_{radial}, and ν_{bridge} C≡N vibrational modes previously published with the following linewidths: 20.5 cm^{-1}, 8.7 cm^{-1}, and 5.3 cm^{-1}, respectively, as well as the calculated angles: $\theta_{\mathrm{trans,radial}}$ = 85°, $\theta_{\mathrm{trans,bridge}}$ = 6° and $\theta_{\mathrm{radial,bridge}}$ = 88° Although the angles between the vibrational modes are known from 2DIR, this does not directly apply to the angle between the vibrational transition and the electronic transition, $\theta_{\mathrm{IR,elec}}$. Instead, the known angles between each vibrational mode, $\theta_{\mathrm{IRx,IRy}}$ (x,y = trans, radial, or bridge),

were used to calculate $\theta_{IRx,elec}$ for each pathway using a rotating frame defined only by the angle between ν_{bridge} and the MMCT in FeRu. This reduces the total number of angle parameters being fit from three to one. After freezing these parameters, a nonlinear least squares curve fit routine was used to fit the experimental spectra of both ZZZZ and ZZYY with the above model at the same time using the remaining fit parameters: $\mu_{IRx,elec}$, $\theta_{IR3,elec}$, ω_{IRx}, ω_{elec}, and Γ_{elec} for the x=1,2,3 vibrational transitions modeled. In order to accurately fit the response, the LO spectrum is divided out of the experimental data to provide the pure third-order signal field. The assumption that the known vibrational angles $\theta_{IRy,IRz}$ are rigid within the fit does not allow for any uncertainty in their measurement so a random sampling of 90 geometries with $\theta_{IRy,IRz} = \theta_{IRy,IRz} \pm 5°$ were fit individually to generate an array of possible fit parameters. This random sampling provides a range of possible fit results within the rigid molecule assumption. For details on the fitting routine as well as the MATLAB code that was used see Section C.3.

5.2 Experimental and Fitting Results

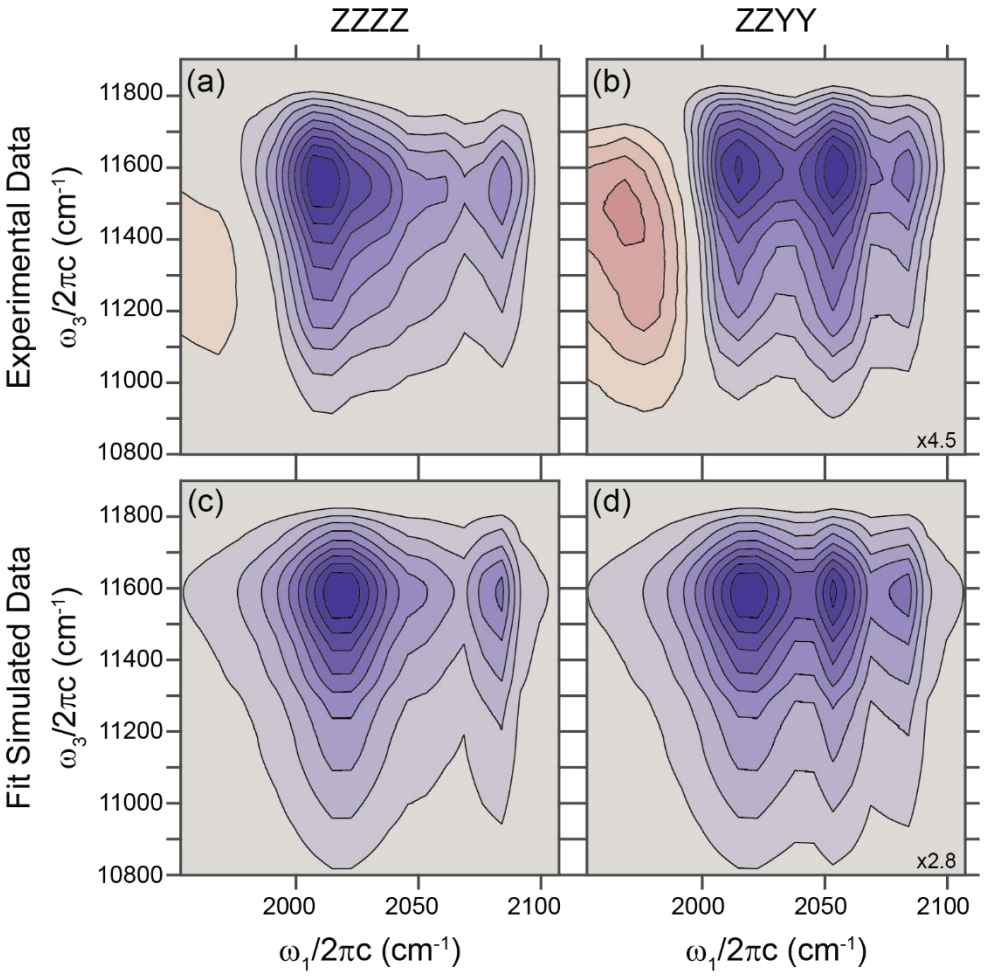

Figure 5-1 Results from the polarization selective 2D VE experiment at τ_2 = 120 fs for ZZZZ (a) and ZZYY (b) polarization as well as the simulated fits for that data (c,d). The ZZYY data has been scaled to match the intensity of the ZZZZ data for clarity. The simulated data is masked by multiplication by the probe along ω_3 to best be visualized in comparison to the experimental data. Contours at 10% intervals.

The resulting experimental 2D VE spectra at τ_2 = 120 fs shown in Figure 5-1(a,b) show the expected negative (blue) ESA features for three IR transitions, as previously discussed. Along ω_1, the ZZZZ spectrum is dominated by the wide ν_{trans} feature at ~2010 cm^{-1}, with significant contribution from the ν_{bridge} mode at ~2090 cm^{-1}. The ν_{radial} mode is greatly enhanced in the ZZYY spectrum which is to be expected from a pathway that includes a near perpendicular angle between

the two transition dipoles. Positive (red) signal below 2000 cm^{-1} is generally contributed to nonresonant formamide (FA) solvent response as previously reported.[15] The simulated spectra using the optimized fit parameters are shown in Figure 5-1(c,d). As discussed above, both the dipole interaction and the orientational response are responsible for the amplitude associated with each vibrational transition, so the bridging C≡N has a large relative $\mu_{IR,elec}$ resulting from strong vibronic coupling between the near parallel vibrational and electronic transitions. On the other hand, ν_{radial} is strongly enhanced only in the ZZYY experiment as the crossed polarization allows for a stronger response to a vibrational mode closer to perpendicular to the electronic transition. The full results for the simulated fits are provided in Table 5-1. These results match transient IR studies on FeRu which report anisotropy measurements consistent with the ν_{trans} and ν_{bridge} modes being approximately parallel to the charge transfer axis and the ν_{radial} mode perpendicular to the charge transfer axis.[18]

Table 5-1 Fit parameters from 90 fixed molecular geometries. The grey values indicate parameters not optimized during fitting.

Transition	μ_x^2	ω_x (cm^{-1})	$\frac{\lvert\mu_{IRx,elec}\rvert^2}{\lvert\mu_{IR1,elec}\rvert^2}$	Γ_x (cm^{-1})	$\theta_{x,elec}$ (°)
IR_1	1.0	2010.7 ± 0.1	1.0 ± <0.01	20.5	9 ± 1
IR_2	0.31	2048.0 ± 0.3	0.51 ± 0.03	8.7	92 ± 2
IR_3	0.05	2074 ± 2	2.83 ± 0.02	5.3	3 ± 1

To demonstrate the importance of being able to separate $\mu_{IR,elec}$ from Y_{IJKL} to the simulation results, Figure 5-2 shows what a spectrum with equivalent $\mu_{IR,elec}$ would look like. In this simulation only the orientational response is allowed to modify the amplitudes of the ESA signals which prevents the bridge mode from showing up as it has a weak IR dipole and is parallel to the charge transfer axis. Clearly the amplitude difference seen in the experimental data (Figure 5-1(a,b)) are highly dependent on the coupling between the MMCT and the individual vibrational

modes. Even though the vibrations are similar in energy to one another, their coupling intensity varies wildly as seen in Table 5-1. Alternatively, without the ability to include Y_{IJKL}, there is no way to simulate different spectra as a result of polarization changes in the experiment.

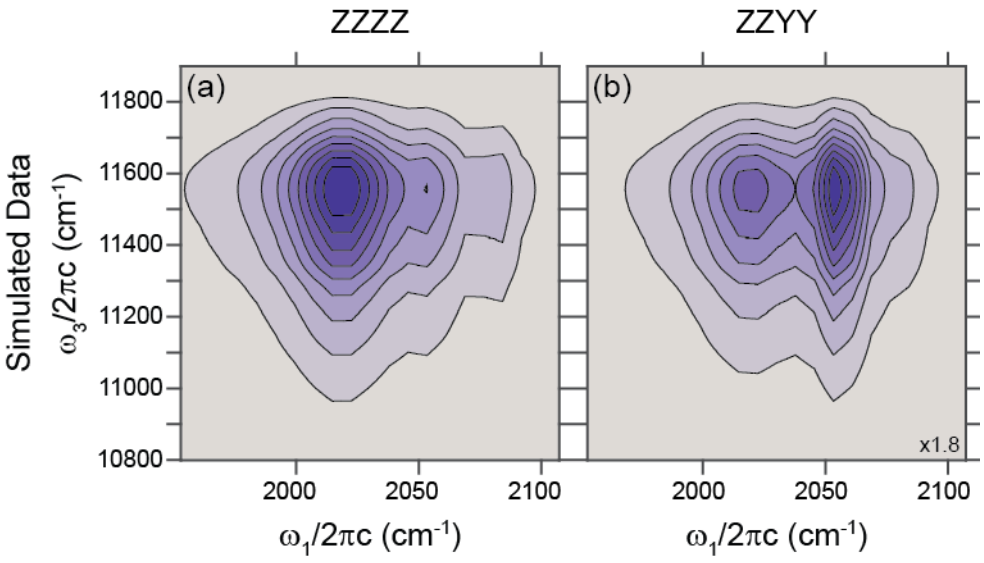

Figure 5-2 Simulated data when all of the electronic transition dipole moments are set to 1. The bridging CN mode at 2089 cm^{-1} barely shows any intensity compared with the trans and radial modes (2002 cm^{-1} and 2052 cm^{-1} respectively), in contrast to the experimental data.

In summary, this work describes the continued development of 2D VE with the addition of polarization sensitive measurements which provide insights into the structure of the molecule as well as the structure of the transition states associated with any vibronically coupled electron transfer. The use of this technique can be easily applied to samples of importance in biology and materials science when the role and orientation of electronically coupled vibrational modes is being investigated. By separating the orientational and transition dipole factors of spectral amplitude, the result of vibrationally-driven electron transfer is directly observed and quantified. As techniques such as 2D VE and 2D EV evolve, their value to the spectroscopy community increases and molecular information not previously accessible is directly measured.

5.3 Experimental Methods

The FeRu sample used in this experiment was synthesized using literature methods with modifications previously described by our group.[9,19] After synthesis, ~110 mg of FeRu was dissolved in 12 mL of FA and stirred overnight to form a 20 mM solution. The solution was syringe filtered (0.45 μm pore radius) to remove any undissolved sample and linear spectra were collected to check purity using a FTIR (FT/IR-4100, JASCO). The 2D VE setup with fast scanning detection here has been described in detail in previous works and will be reprised here briefly with current configuration.[6][Fast Scanning Paper] All pulses are generated from the output of a 1 kHz Ti:sapphire regenerative amplifier (800 nm, 35 fs, 2.5 W). The MIR pumps are generated by seeding a dual pass optical parametric amplifier (OPA-800C, Newport) which produces a NIR signal, idler pair that are difference frequency mixed in a 0.5 mm thick $AgGaS_2$ crystal. The resulting MIR light is centered at ~2050 cm^{-1} and has a bandwidth of ~200 cm^{-1}. Next, a Mach-Zehnder interferometer equipped with helium-neon (HeNe) laser fast tracking is used to split the pump into two independently timed pulses. During experimentation, τ_1 is scanned by a computer-controlled stage and its position monitored by the HeNe tracking system. The τ_1 step size is determined by the HeNe light used to track the stages, 1.055 fs, and corresponds to ~16 points per MIR cycle (8x oversampled). At the sample area, the pumps are vertically polarized and focus to a $1/e^2$ spot size of ~150 μm. To control τ_2, the portion of the 800 nm amplifier output used for the NIR probe is sent through a long retroreflecting computer-controlled stage before focusing ~500 nJ into a 3 mm thick sapphire window. The resulting continuum is compressed using a pair of fused silica prisms and the fundamental is filtered out using a long pass filter (>850 nm). The probe (10 nJ) is routed to the sample area as a vertically polarized to match the MIR pump. A linear polarizer (LPNIR050-MP2, ThorLabs) set at 45° off of the laboratory vertical reference

projects the light to be 50:50 vertical:horizontal polarization. Another linear polarizer is placed after the sample to select which experiment will be detected, with the polarizer allowing vertically polarized light through for the ZZZZ experiment and horizontally polarized light through for the ZZYY experiment. When focused through the sample, the probe has a spot size of ~100 μm in diameter. The sample is continuously flowed in a home built brass sample cell with 140 μm thick Teflon spacers between 1 mm thick CaF_2 windows used to create the cell pathlength. In addition to flowing, the sample cell is translated perpendicular to the incident beams to avoid damage to the sample or window.

Detection of the probe LO and the signal is accomplished through single mode fiber coupling (750 HP, ThorLabs) to a 0.303 m Czerny-Turner spectrometer (Shamrock SR-303i with 600 groove/mm grating,800 nm blaze, and f/4 optics, Andor) with an attached 1600 × 200 pixel CCD array (DU970P-UV, front illuminated, Andor). The light detected by the CCD contains the collinear probe (LO) and the signal on top, $\left|\hat{E}_{LO}(\omega_3) + \hat{E}^{(3)}_{sig}(\tau_1, \omega_3, \tau_2)\right|^2$ but by chopping the pumps at 500 Hz, alternating shots can be used to subtract $I_{\mathrm{LO}}(\omega_3)$ leaving only the dominating cross term: $\hat{E}_{LO}(\omega_3) \cdot \hat{E}^{(3)}_{sig}(\tau_1, \omega_3, \tau_2)$. Data is collected for a single τ_2 point by continuously scanning τ_1 over a range of -100 – 1500 fs, as determined by HeNe tracking. The experimental τ_1 = 0 is confirmed and a Fourier transform is performed on the background subtracted cross term along τ_1 resulting in the absorptive 2D VE spectrum as a function of ω_1 and ω_3 parametrized by the waiting time τ_2.

References

(1) Li, X.; Zhang, T.; Borca, C. N.; Cundiff, S. T. Many-Body Interactions in Semiconductors Probed by Optical Two-Dimensional Fourier Transform Spectroscopy. *Phys. Rev. Lett.* **2006**, *96*, 057406.

(2) Ginsberg, N. S.; Cheng, Y.-C.; Fleming, G. R. Two-Dimensional Electronic Spectroscopy of Molecular Aggregates. *Acc. Chem. Res.* **2009**, *42* (9), 1352–1363.

(3) Thielges, M. C.; Fayer, M. D. Protein Dynamics Studied with Ultrafast Two-Dimensional Infrared Vibrational Echo Spectroscopy. *Acc. Chem. Res.* **2012**, *45* (11), 1866–1874.

(4) Woutersen, S.; Hamm, P. Time-Resolved Two-Dimensional Vibrational Spectroscopy of a Short α-Helix in Water. *J. Chem. Phys.* **2001**, *115* (16), 7737–7743.

(5) Oudenhoven, T. A.; Joo, Y.; Laaser, J. E.; Gopalan, P.; Zanni, M. T. Dye Aggregation Identified by Vibrational Coupling Using 2D IR Spectroscopy. *J. Chem. Phys.* **2015**, *142* (21), 212449.

(6) Courtney, T. L.; Fox, Z. W.; Slenkamp, K. M.; Khalil, M. Two-Dimensional Vibrational-Electronic Spectroscopy. *J. Chem. Phys.* **2015**, *143* (15), 154201.

(7) Oliver, T. A. A.; Lewis, N. H. C.; Fleming, G. R. Correlating the Motion of Electrons and Nuclei with Two-Dimensional Electronic-Vibrational Spectroscopy. *Proc. Natl. Acad. Sci.* **2014**, *111* (28), 10061–10066.

(8) Golonzka, O.; Khalil, M.; Demirdöven, N.; Tokmakoff, A. Coupling and Orientation between Anharmonic Vibrations Characterized with Two-Dimensional Infrared Vibration Echo Spectroscopy. *J. Chem. Phys.* **2001**, *115* (23), 10814–10828.

(9) Slenkamp, K. M.; Lynch, M. S.; Kuiken, B. E. Van; Brookes, J. F.; Bannan, C. C.; Daifuku, S. L.; Khalil, M. Investigating Vibrational Anharmonic Couplings in Cyanide-Bridged Transition Metal Mixed Valence Complexes Using Two-Dimensional Infrared Spectroscopy Investigating Vibrational Anharmonic Couplings in Cyanide-Bridged Transition Metal Mixed Valence Complex. *J. Chem. Phys.* **2014**, *140*, 084505.

(10) Jonas, D. M.; Lang, M. J.; Nagasawa, Y.; Joo, T.; Fleming, G. R. Pump−Probe Polarization Anisotropy Study of Femtosecond Energy Transfer within the Photosynthetic Reaction Center of *Rhodobacter Sphaeroides* R26. *J. Phys. Chem.* **1996**, *100* (30), 12660–12673.

(11) Lewis, N. H. C.; Dong, H.; Oliver, T. A. A.; Fleming, G. R.; Lewis, N. H. C.; Dong, H.; Oliver, T. A. A.; Fleming, G. R. Measuring Correlated Electronic and Vibrational Spectral Dynamics Using Line Shapes in Two-Dimensional Electronic-Vibrational Spectroscopy Measuring Correlated Electronic and Vibrational Spectral Dynamics Using Line Shapes in Two-Dimensional Electronic-Vi. *J. Chem. Phys.* **2015**, *142*, 174202.

(12) DeFlores, L. P.; Nicodemus, R. A.; Tokmakoff, A. Two-Dimensional Fourier Transform Spectroscopy in the Pump-Probe Geometry. *Opt. Lett.* **2007**, *32* (20), 2968.

(13) Myers, J. A.; Lewis, K. L. M.; Tekavec, P. F.; Ogilvie, J. P. Two-Color Two-Dimensional Fourier Transform Electronic Spectroscopy with a Pulse-Shaper. *Opt. Express* **2008**, *16* (22), 17420–17428.

(14) Faeder, S. M. G.; Jonas, D. M. Two-Dimensional Electronic Correlation and Relaxation Spectra: Theory and Model Calculations. *J. Phys. Chem. A* **1999**, *103* (49), 10489–10505.

(15) Courtney, T. L.; Fox, Z. W.; Estergreen, L.; Khalil, M. Measuring Coherently Coupled Intramolecular Vibrational and Charge-Transfer Dynamics with Two-Dimensional

Vibrational-Electronic Spectroscopy. *J. Phys. Chem. Lett.* **2015**, *6*, 1286–1292.

(16) Sung, J.; Silbey, R. J. Four Wave Mixing Spectroscopy for a Multilevel System. *J. Chem. Phys.* **2001**, *115* (20), 9266.

(17) Golonzka, O.; Tokmakoff, A. Polarization-Selective Third-Order Spectroscopy of Coupled Vibronic States. *J. Chem. Phys.* **2001**, *115* (1), 297–309.

(18) Wang, C.; Mohney, B. K.; Akhremitchev, B. B.; Walker, G. C. Ultrafast Infrared Spectroscopy of Vibrational States Prepared by Photoinduced Electron Transfer in (CN)5FeCNRu(NH3)5-. *J. Phys. Chem. A* **2000**, *104* (18), 4314–4320.

(19) Vogler, A.; Kisslinger, J. Photosubstitution of Pentaaminechlororuthenium (III) Hexacyanoruthenate (II) Following Outer-Sphere Intervalence Excitation. *J. Am. Chem. Soc.* **1982**, *104*, 2311–2312.

Appendix A

Synthesis of Mixed Valence Compounds

This appendix includes the detailed synthesis of the mixed valence compounds used in this dissertation as well as in other experiments not presented in this work. All molecules exhibit an intramolecular metal-to-metal charge transfer (MMCT), as well as strong CN vibrational markers bridging the metal centers. This makes them ideal candidates to study how charge transfer is affected by vibrational motion. These compounds have been synthesized multiple times and tested for purity before being used in spectroscopy experiments.

A.1 $Na[(CN)_5Fe^{II}(CN)Ru^{III}(NH_3)_5]$ Synthesis

The synthesis of $Na[(CN)_5Fe^{II}(CN)Ru^{III}(NH_3)_5]$ (FeRu) followed the procedure outlined in work by Vogler et al.[1] for the synthesis of a diruthenium cyano-bridged compound. This synthetic procedure was later modified to make the iron-ruthenium dimer version used in the Khalil lab.[2] Our full synthesis version is published here with further minor modifications from the original documents which were found to be helpful for quickly producing large (1-2 grams) quantities of very pure material.

There are two columns used during the synthesis of FeRu. The first is an ion exchange column required to convert the potassium form of FeRu to the desired sodium form. To prepare the ion exchange column, Dowex 50WX8 hydrogen form resin is purchased from Sigma Aldrich and packed into a column. 1.5 M NaCl is sent through the column until the pH of the column output is neutral indicating that all H^+ in the column has been converted to Na^+. After every use of the column the Na^+ is recharged by putting a bed-volume of 1.5 M NaCl through the column. The

second, size-exclusion purifying column of Bio-Gel P2 polyacrylamide beads (Bio-Rad Laboratories) is packed using the instructions provided in the user manual.

The starting materials, $K_4Fe^{II}(CN)_6 \cdot 3H_2O$ (**1**), and $[Ru^{III}(NH_3)_5Cl]Cl_2$ (**2**) were purchased from Sigma Aldrich and Alfa Aesar respectively and used without further purification. 253 mg (0.6 mmol) of (**1**) is dissolved in 15 mL of H_2O, while 175 mg (0.6 mmol) of (**2**) is dissolved in 35 mL H_2O while being gently stirred and heated to 35 °C. Once the solution of (**2**) is fully dissolved to form a light-yellow solution, (**1**) is added which will immediately form a green solution of $K[(CN)_5Fe^{II}(CN)Ru^{III}(NH_3)_5]$. This solution is allowed to stir for 2 hours at 60 °C over which the color of the solution will continue to darken. After 2 hours the solution is filtered hot using a Buchner funnel and Watman 50 filter paper. The dark green solution is reduced in volume to ~5 mL by blowing dry air over the top. Once the volume is reduced, the solution is sent through the Dowex ion exchange column. The collected sodium form FeRu is dried and then redissolved in minimal <5 mL H_2O. Any leftover precipitate is discarded at this stage and the clear solution is placed in the Bio-Gel size exclusion column. The dark green band containing pure FeRu is collected and dried for storage/combining. To check the purity of the sample, a 5-10 mg sample is dissolved in 1 mL of formamide (FA) and the FTIR is taken on a JASCO FT/IR-4100 (Figure A-1 (a)). The UV-Visible spectrum in H_2O is taken using a Cary 5000 (Agilent) (Figure A-1(b)).

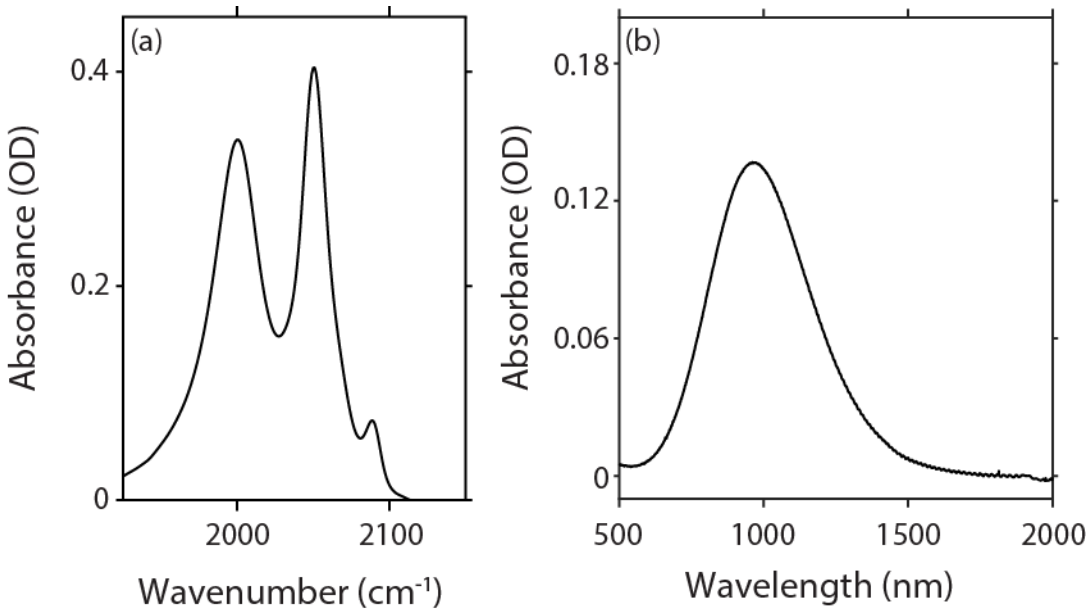

Figure A-1 Linear spectra of FeRu. The FTIR of the ν_{CN} region (a) is taken in FA solvent 20 mM with a 140 μm pathlength, the solvent background has been subtracted out. The UV-Visible spectrum (b) is taken in H_2O solvent 40 mM with a 50 μm pathlength sample cell, the solvent background has been subtracted out.

A.2 $Na_4[(CN)_5Fe^{II}(CN)Pt^{IV}(NH_3)_4(NC)Fe^{II}(CN)_5]$ Synthesis

The synthesis of $Na_4[(CN)_5Fe^{II}(CN)Pt^{IV}(NH_3)_4(NC)Fe^{II}(CN)_5]$ (FePtFe) follows the procedure outlined in work by Watson et al.[3] The starting materials, $K_3Fe^{III}(CN)_6$ (**3**) and $Pt^{II}(NH_3)_4(NO_3)_2$ (**4**) were purchased from Sigma Aldrich and used without further purification. 329 mg (1 mmol) of (**3**) were dissolved in 25 mL of H_2O while 194 mg (0.5 mmol) of (**4**) were dissolved in another 25 mL of H2O. The two solutions are combined and the resulting deep amber solution is sent through an Amberlite 120IR Na^+ form ion exchange column and air dried to generate the final FePtFe product. The FePtFe is redissolved in <5 mL and sent through a different Bio-Gel size exclusion (see Section A.1 for details) than the one used in the synthesis of FeRu to prevent cross contamination. Cyclic voltammetery (CV) measurements showed that in order to completely remove any (**3**) starting material the size exclusion column needed to be run twice (see Figure A-2(a)). Sample was checked again for purity by UV-visible spectroscopy using a JASCO V-630 spectrometer (Figure A-2(b)), FTIR using a JASCO FT/IR-4100 (Figure A-2(c)).

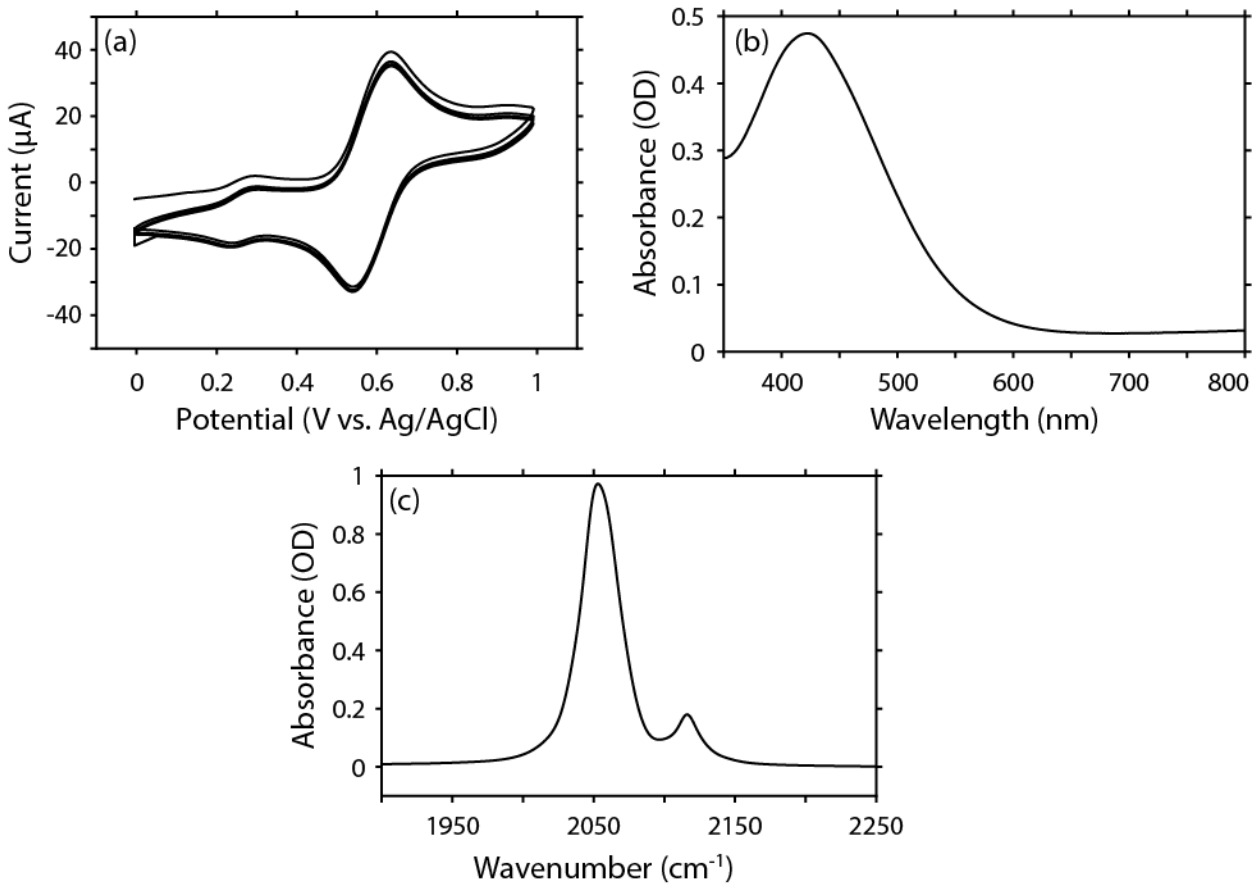

Figure A-2 Linear Spectra of FePtFe. The CV of FePtFe (a) shows the starting material (3) as a small side peak in addition to the main FePtFe feature of the iron red/ox. The UV-Visible spectrum of pure FePtFe (b) shows the MMCT peak centered at ~420 nm. The FTIR of pure FePtFe ν_{CN} region (c) has two main features in H_2O. The optical spectra were both taken of 40 mM solutions in H_2O with a 50 μm pathlength sample cell where the solvent has been subtracted.

A.3 $Na_4[Fe^{III}(CN)_6Ru^{II}(C_6H_5N)_4Fe^{III}(CN)_6]$ Synthesis

The synthesis of $Na_4[Fe^{III}(CN)_6Ru^{II}(C_6H_5N)_4Fe^{III}(CN)_6]$ (FeRuFe) was outlined in the work of Alborés et al.[4] The full procedure requires the synthesis of the starting material *trans*-$RuCl_2(py)_4$ (**5**) through the known synthetic procedure outlined by Evans et al.[5] All materials are purchased from Sigma Aldrich and used without further purification. The size exclusion column is packed with Sephadex LH-20 gel using methanol as the mobile phase.

To synthesize (**5**), 969 mg (2 mmol) of $RuCl_2(dmso)_4$ (**6**) is combined with 9.8 mL of pyridine and 25 mL of ethanol in a small round bottom flask fixed with a condenser. The solution is stirred

and refluxed at 80 °C for 3 hours. A color change from bright yellow to orange should occur during this time. The orange solution should be gravity filtered twice while still hot using Whatman 40 filter paper to completely collect the fine orange precipitate. An ethanol wash completes the synthesis of (**6**) which was should dry overnight before use in the next step of synthesis. The ^{1}H-NMR of (**6**) was used to check purity (Bruker, 500 MHz) by comparing the spectrum (Figure A-3) with literature values of similar compounds reported in Coe et al.[6]

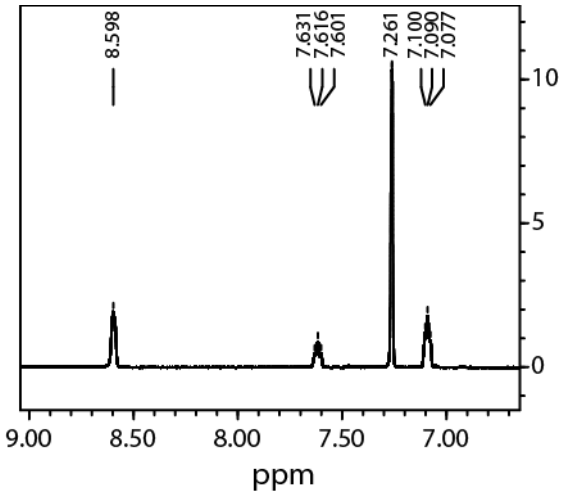

Figure A-3 ^{1}H-NMR spectrum of (**6**) dissolved in $CDCl_3$ zoomed into the shift region of the pyridine hydrogens demonstrating a pure sample. All shifts are relative to TMS.

Once pure starting material was confirmed, 0.41 mg (1 mmol) of (**6**) was combined with excess (> 10 mmol) (**3**) in 50 mL of a 4:1 H_2O:ethanol solution in a round-bottom flask fit with a condensing column. The apparatus was covered in foil to prevent any photodegradation and flushed with N_2 and kept under positive pressure inert environment with an N_2 bubbler. The solution was refluxed with stirring at 87 °C for 4 hours and then set to cool (still foil covered) until room temperature (~1 hour). 100 mL of methanol is added to the solution to precipitate out any leftover (**3**) and the fine precipitate is removed by vacuum filtration through a medium grit glass filter frit. The filtrate is allowed to air dry before being dissolved in a minimal volume of H_2O. While stirring, 1.43 g of $(C_6H_5)_4PCl$ is added to form a light green slurry of FeRuFe but with

$(C_6H_5)_4P^+$ counterions replacing the Na^+. This product is allowed to sit overnight at 0 °C. The solution is then vacuum filtered using a medium grit glass filter frit and washed with methanol before being condensed to 10 mL by blowing air over the solution. At this point the solution is sent through the Sephadex size exclusion column and the dark green product band is recovered and allowed to air dry. Further purification is accomplished by vapor diffusion of diethyl ether into methanol to form dark green needle-like crystals. Finally, the product is ion-exchanged for Na^+ counterions by dissolving the crystals in acetonitrile and combining with 8.2 mg of $NaClO_4$ and vacuum filtering the solution through a medium grit filter frit to collect the final FeRuFe solid and finally washing with H_2O. The final product is checked for purity by FTIR and UV-visible spectroscopy (Figure A-4).

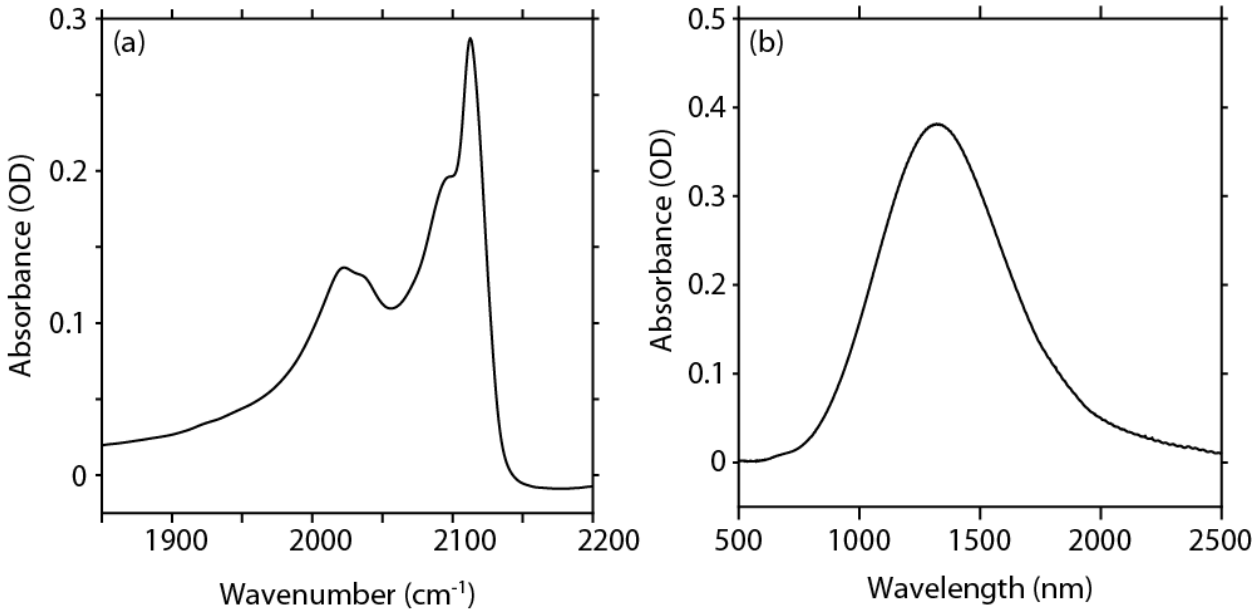

Figure A-4 Linear spectra of FeRuFe. The FTIR of the ν_{CN} region (a) is generally complex and difficult to background subtract regardless of solvent. The UV-Visible spectrum (b) shows that FeRuFe has a much lower energy MMCT band which peaks at 1320 nm. Both spectra shown here are 40 mM solutions in H_2O using a 50 μm pathlength sample cell.

References

(1) Vogler, A.; Kisslinger, J. Photosubstitution of Pentaamminechlororuthenium(III) Hexacyanoruthenate(II) Following Outer-Sphere Intervalence Excitation. *J. Am. Chem. Soc.* **1982**, *104* (8), 2311–2312.

(2) Walker, G. C.; Barbara, P. F.; Doorn, S. K.; Dong, Y.; Hupp, J. T. Ultrafast Measurements on Direct Photoinduced Electron Transfer in a Mixed-Valence Complex. *J. Phys. Chem.* **1991**, *95*, 5712–5715.

(3) Watson, D. F.; Tan, H. S.; Schreiber, E.; Mordas, C. J.; Bocarsly, A. B. Femtosecond Pump-Probe Spectroscopy of Trinuclear Transition Metal Mixed-Valence Complexes. *J. Phys. Chem. A* **2004**, *108*, 3261–3267.

(4) Alborés, P.; Slep, L. D.; Weyhermüller, T.; Baraldo, L. M. Fine Tuning of the Electronic Coupling between Metal Centers in Cyano-Bridged Mixed-Valent Trinuclear Complexes. *Inorg. Chem.* **2004**, *43* (21), 6762–6773.

(5) Evans, I. P.; Spencer, A.; Wilkinson, G. Dichlorotetrakis(Dimethyl Sulphoxide)Ruthenium(II) and Its Use as a Source Material for Some New Ruthenium(II) Complexes. *J. Chem. Soc. Dalt. Trans.* **1973**.

(6) Coe, B. J.; Meyer, T. J.; White, P. S. Synthetic and Structural Studies on Trans-Tetrapyridine Complexes of Ruthenium(II). *Inorg. Chem.* **1995**, *34* (3), 593–602.

Appendix B

Fast Scanning Communication and Timing

The constant monitoring of multiple data streams makes the timing and communication in the fast scanning 2D VE experiment extra challenging. In this appendix some of the pitfalls are discussed as well as details that make the experiment work as it is supposed to.

B.1 Timing

All of the various instruments that are used in this experiment require a master clock to ensure synchrony. As with many of the other experiments performed in the Khalil lab, the regenerative amplifiers timing delay generator (TDG) acts as the master clock to synchronize the detection instruments with the actual laser pulses. Master clock timing is communicated through coaxial cables fit with BNC connectors for quick adjustment when necessary. These cables transmit the 1 kHz TTL pulses which mark each laser pulse. Three separate delay channels are used to control the hardware: channel 6 (C6), channel 7 (C7), and channel 8 (C8). Each channel is able to be individually delayed to compensate for the length of cable being used as well, as response time of the instrument receiving the timing signal.

C6 controls the DAQ board clock set to 0 μs. This timing is set with respect to the response time of the mercury cadmium telluride single channel detector (MCT). Plugging the MCT into the oscilloscope, and triggering off of C6 should give align the rising edge/top of the MCT response with the trigger TTL pulses. If the timing is off the DAQ board will miss the detectors response to the laser pulse. It is important to remember that the DAQ board does not collect a gated integrated signal, but rather a single voltage value upon being triggered. The fast response of the MCT is also important to accuracy of the stage tracking. The DAQ board simultaneously

collects the MCT voltage along with the two fast scanning photodiode (PD) voltages, and the chopper TTL voltage. As the stage is consistently moving, a delayed response by the DAQ board would calculate a time shift that was incorrect for the laser shot associated with that shift.

The least sensitive channel timing is that of C7. This controls the chopper wheel and generally should center the laser pulse within the 500 Hz signal output and was set to 860 μs for this experiment. The chopper TTL output is a square-wave function with a period of 1 ms so any reading within the 500 μs window around the laser pulse should correctly report on the chopper condition for that laser shot. When adjusting the chopper, the phase control on the chopper box should be used to ensure that there is no leakage of the pump when the pump should be blocked. Setting the chopper is easily done by looking at the pulse train of the pump after the chopper on the oscilloscope and making sure that alternating pulses are completely blocked. Any leakage can be compensated for using the phase control on the chopper box.

The last timing signal comes from C8 for the CCD camera. Unlike the DAQ board, the CCD does collect a gated integrated signal with a 10 μs exposure window which is the minimum exposure time possible for our device. The setting used for this experiment was 145 μs and can be set by maximizing the signal while looking at the probe spectrum. If only C8 is changed, any amplitude change in the probe spectrum will come as a result of the exposure windowing becoming more or less aligned with the laser pulse timing. The CCD is also used to trigger all data collection. Once data collection begins the CCD sends a TTL trigger to the DAQ board via coaxial cable indicating that data is being stored in the camera memory. This trigger pulse is received by the DAQ board which will simultaneously begin to collect data. This ensures that all detectors are running at the same time for all laser shots.

It is likely that the DAQ board will not be able to begin collection on the same laser shot as the CCD, this is a because it is programed to wait for the CCD fire trigger to collect data. This offset between shot indices is corrected for in LabVIEW by throwing away a number of shots from the front of the CCD data equal to the delay between the CCD and DAQ board. Likewise, the last shots the DAQ board records must be thrown away as they do not have corresponding CCD data. This delay is variable and mostly dependent on C8 timing and the length of the cable connecting the CCD fire trigger to the DAQ board. The CCD offset box in the LabVIEW detection codes which utilize fast scanning and relates to the number of shots to remove from the front/back of the CCD/DAQ board data respectively. Errors in the channel timing should be made obvious by extremely low or noisy signal.

B.2 Communication Between Devices

The communication between all devices was roughly laid out in Figure 4-2 but will be more explicitly outlined here. As explained in Section B.1, the regenerative amplifier TDG is connected directly with the DAQ board (C6), the chopper box (C7) and the CCD camera (C8). This connection delivers the 1 kHz TTL clock which times the experiment. The CCD also sends the start trigger to the DAQ board indicating the beginning of data collection for all devices. In addition to those connections which pass timing information (red arrows in Figure 4-2), there are 4 analogue inputs used on the DAQ board which are read with each laser shot (blue arrows in Figure 4-2. AI_1 and AI_3 connect to the fast scanning PDs, AI_4 connects to the chopper box output, and AI_6 connects to the MCT. These 4 channels show up on the LabVIEW front panel as the physical channels to be detected and need to be double checked, especially if the analogue channels used changes. LabVIEW will read the channels in ascending order so switching the order of the inputs will result in unwanted behavior.

The final data set is communicated to the computer via two high speed USB connections, one for the DAQ board and one for the CCD. This data is delivered in chunks, limited by the buffer available on the CCD. The memory limit is near 120,000 shots for the acquisition setup used in this experiment, but 60,000 shots (1 minute) was used to ensure that the computer memory wasn't overloaded during data processing (see Appendix C). All collection is controlled via homebuilt LabVIEW software which collects all data, does minimal processing, and saves the data for full workup.

Appendix C

Fast Scanning Data Workup

Fast scanning detection is a marked change from the way that data is traditionally collected in the Khalil lab, and requires careful workup to avoid slowdowns or excessive data volumes while collecting and working up the data. Unlike the step scanning experiments, where the stages do not move, and consecutive laser shots can be averaged together, fast scanning requires the collection of meta data for each individual laser shot to keep track of the stage position, and chopper status. These data must be used later to properly average laser shots of the same type together. In this appendix, I will outline the LabVIEW collection programs as well as the steps required to get from raw data to the final presented form of the data.

C.1 Live LabVIEW Scripts

There are two main sub programs to handle the data during data acquisition: the fast scanning binning program which converts the fast scan photodiode voltage readings into bin values, and the bin averaging program which averages all laser shots with the same bin value and subtracts off the chopper on background spectra. These are incorporated directly into the data collection routine to avoid massive raw data file-sizes. Without binning and averaging, this experiment will generate multiple gigabytes of data per minute, versus the tens of megabytes generated with averaging.

C.1.1 Calculating Bin Values for each Shot

Without actively binning each laser shot, fast scanning is not possible. This means that as the data are collected the index corresponding to laser shot must have the following information in order to be processed: The relative bin value, the chopper mode, the MCT detector voltage, and the CCD spectrum. The relative bin value is determined during the experiment using the fast

scanning photodiode voltages read by the DAQ board simultaneously with each laser shot. The bin value calculating sub VI (HeNeTrace_circle_fit_PostProcessVersion.vi) takes the two photodiode voltage values and fits them to the *x* and *y* components of the fit to sphere function. The *z* data is fed a zeros vector of the same length as *x* and *y* to fit the data to a circle instead of a sphere. The circle fit is used to fit the data to a unit circle by subtracting the central *x* and *y* value from the raw data and then dividing by the circle radius. A single complex value number associated with each laser shot is defined as $x + iy$ and LabVIEW performs the coordinate transformation from the complex plane to r and θ. The variable θ allows each shot to be placed into the quadrants of a unit circle for binning (See Figure 4-4). The calculated angles are assigned to bins using the logic tree shown in Figure C-1. It is important to make sure that the stage is not moving too quickly as it will cause the binning program to undercount the number of bins passed through.

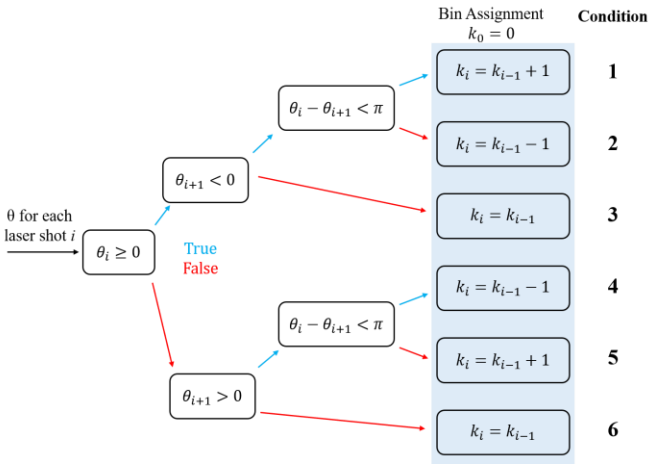

Figure C-1 Logic chain for the assignment of bins during fast scanning. The first shot is assigned k = 0 and each laser shot, i, is assigned a bin relative (blue box) to the first shot using this logic chain. Conditions **1** and **5** result in an increase in k of 1 compared with the previous shot, conditions **2** and **4** result in a decrease in k of 1 compared with the previous shot, and conditions **3** and **6** do not change the value of k from the previous shot.

C.1.2 Averaging Like Bins in Raw Data

As previously mentioned, collecting 1600 pixels every millisecond generates extremely large file sizes if all the information is stored for post processing. To avoid this, data are "folded" by averaging together all of the data that fall within the same value as defined by the binning program outlined in Section C.1.1. The complication here is that the bin values do not necessarily change shot to shot (conditions **3** and **6** in Figure C-1) so the change in shot index between same valued bins varies. Data folding during data collection is accomplished by using a MATLAB node within LabVIEW. This has been found to be more efficient than using functions within LabVIEW itself to do the mid-experiment data processing.

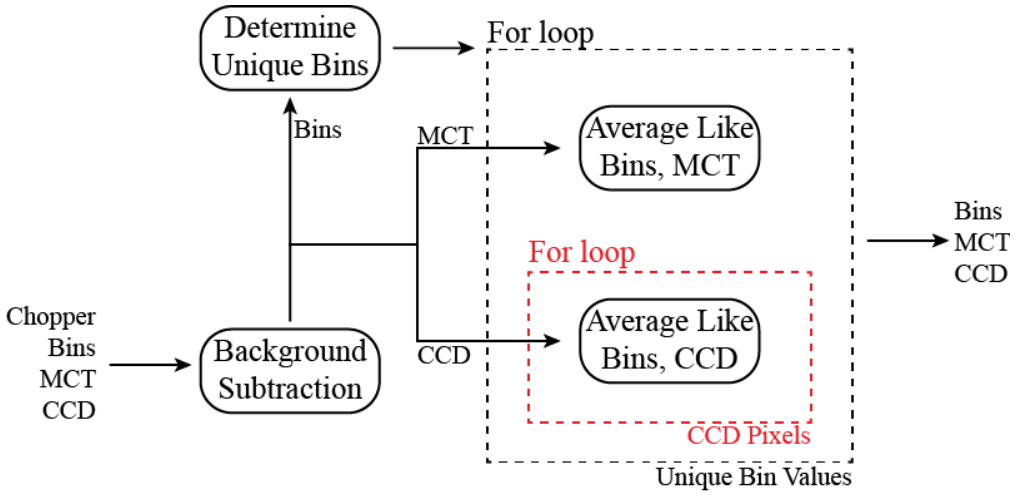

Figure C-2 MATLAB coding flow used during the experiment to average the data together providing smaller file sizes. The for loops are stacked, meaning that each iteration of the outer loop must go through the entire inner loop requiring total iterations equal to the product of each loops iteration size. This is the main time drag for the data collection process and can add minutes to the processing time depending on the number of unique bin values. To combat this, the inner loop (red) is run in parallel using MATLABs built in parfor loop function.

A flow chart outlining the MATLAB code used in the in-experiment data workup is given in Figure C-2. First the data must be background subtracted by using the chopper input to determine the chopper condition (*on* or *off*) of the first shot. Because the chopper is run at 500 Hz, adjacent laser shots will have alternating chopper conditions. If the chopper is *on* (pump is blocked) during

the first shot, odd indexed shots (i = 1, 3, 5, …) are subtracted from the even indexed shots (i = 2, 4, 6, …) giving the background subtracted data (2-1, 4-3, 6-5, …). If the chopper is *off* (pump is unblocked) than the opposite subtraction occurs. Only the bin values for the chopper *off* conditions are kept, as these are the shots which provide the actual signal data.

Next, the script determines the unique bin values calculated in the binning programming and uses logical indexing to extract all data corresponding to those unique bin values using a for loop. This process is simple for the MCT data, but the large size of the CCD data slows the processing down considerably. Each pixels data are independent of one another, making manipulation of their data a great candidate for parallel processing. This is accomplished using a *parfor* loop nested within the bin value loop. MATLAB handles the distribution of information across the available CPU cores automatically which minimizes the challenges normally associated with parallel computing. Once both the MCT and CCD data streams have been averaged according to bin, they are saved into a timestamped MATLAB data file for ease of integration into the post processing described in Section C.2.

C.2 Data Processing

Once the data has been collected there will be separate MATLAB data files for every 1 minute chunk of data collected. This data consists of two variables: MCT_avg, and CCD_avg. They should be the same length (corresponding to the number of unique bins, Nbin), either 1 × Nbin (MCT_avg) or Nbin × 1600 (CCD_avg). The MCT data is used to experimentally determine which bin corresponds to τ_1 = 0, t_0. The background of the MCT signal is removed using the *detrend* function in MATLAB and the maximum intensity defines t_0 for each scan. Because the stages are scanning across the same range, each scan should have approximately the same bin

value, k_{max}, corresponding to t_0 (See Figure C-3). In fact, instead of simply using the bin associated with the max MCT signal, the mode of those bins is used as k_{max}. This will occasionally cause a phase shift which will need to be corrected, but in general keeps those phase corrections to a minimum compared to other way of determining k_{max}.

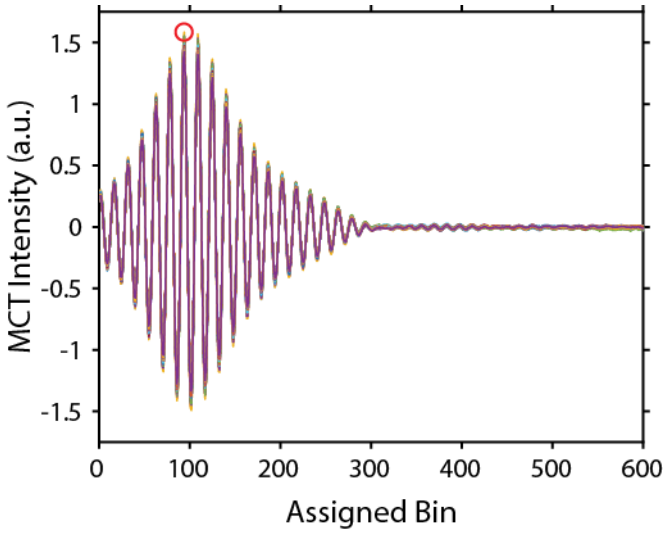

Figure C-3 Background subtracted data from the MCT detector. Each trace is from the output of a 60 second scan. The bin value at the maximum of each trace corresponds to the experimental point t_0. Here, because the data peaks at bin value k_{max} = 94 (red circle), all data corresponding to bins k = 1 to 93 are discarded.

The most obvious indication of a phasing problem will show up in the frequency domain pump spectrum recovered from the real part of the Fourier transform of the MCT interferogram, cropped at k_{max}. A bin shift by 1 in the time domain shows up very clearly in the frequency domain as a phase twist on the IR spectrum, as shown in Figure C-4. Averaging should not be relied upon to correct for these errors, as they are easily fixable by shifting the data on specific scans by 1 bin. All examples here have relied upon the MCT interferogram data because of the large signal amplitude and obvious phase dependence, but it is important to remember to repeat any manipulation done to the MCT indices (cropping or shifting) to the CCD data.

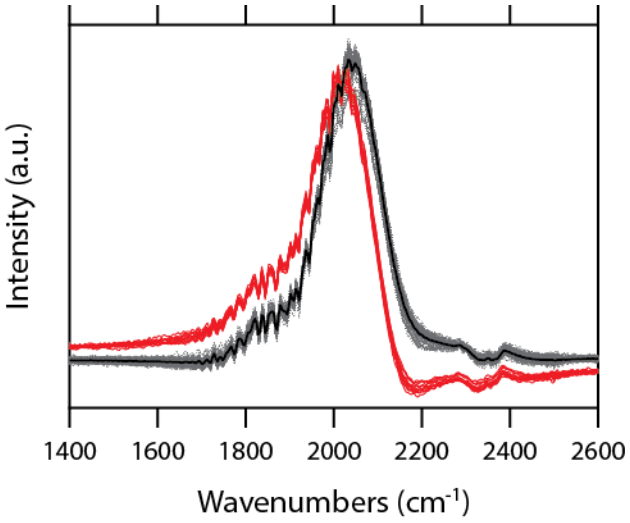

Figure C-4 Errors in the MCT spectra occur when there is a phase shift. When k_{max} is off by one on an individual scan the Fourier transformed spectra exhibits a slightly dispersive twist (red lines) resulting from the phase shift. In general most scans should be correctly phased (grey lines). Once the phase shifted spectra are fixed the averaged spectrum (black) clearly shows agreement with the grey spectra.

Once all of the bins of each scan are aligned, the data which falls in the bins before k_{max} is discarded. Some of the scans will have a few extra bins preventing the data from being concatenated into a single matrix. All of the scans are cropped at high bin values to the shortest scan to enable concatenation and thus averaging without having to use a for loop. An example of a single pixel (pixel 600) of 2D VE time domain data is shown in Figure C-5 after all scans have been averaged.

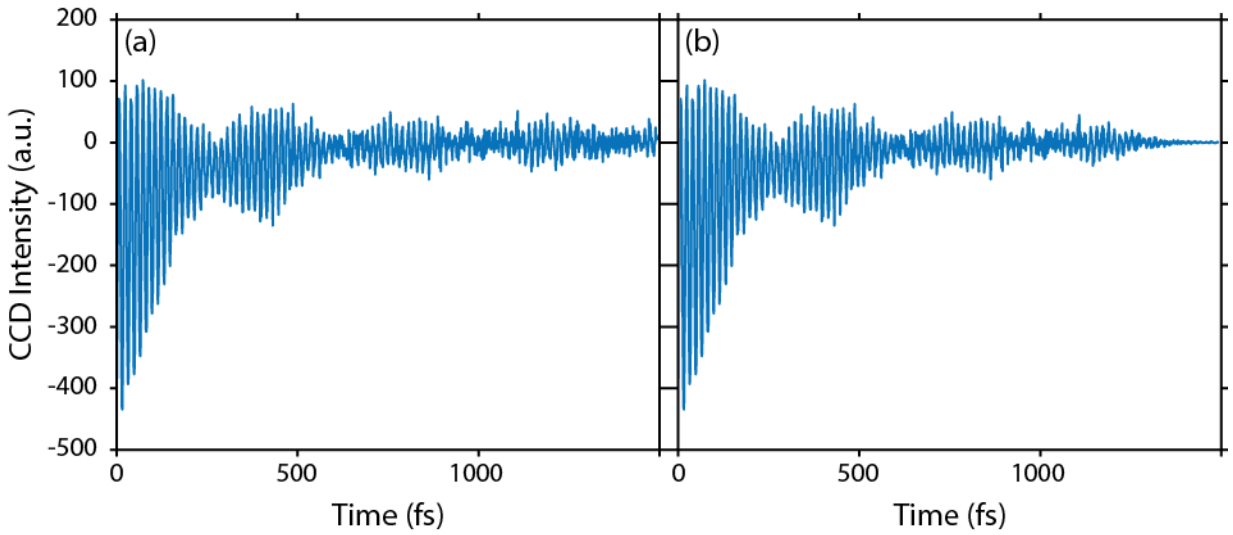

Figure C-5 The trace of the VE time domain data from pixel 600. (a) The averaged time domain VE signal after being cropped at t_0 but before apodization. (b) The time domain signal is filtered by multiplying the signal by a hyperbolic tangent apodization function centered at 1250 fs with a 150 fs FWHM.

To reduce noise in the frequency domain Fourier transform signal, a hyperbolic tangent apodization function is applied to the data (Figure C-5). The cropped and filtered time domain data is zero padded out to 2 times the next highest power of 2 and fast Fourier transformed using the *fft* function in MATLAB. For example, if the scan is 2000 shots long, the zero padding will go out to 4096 points (2×2^{11} points).

C.3 Fitting Routine, MATLAB Code

In order to extract meaningful physical information, the worked up data must be fit using the response function model described in Chapter 5. The challenge is to reduce the parameter space such that convergence is possible and within the physical bounds that we know to be true about the compound already. The fitting function is provided here in its entirety, but an outline of the strategy is also provided in Figure C-6.

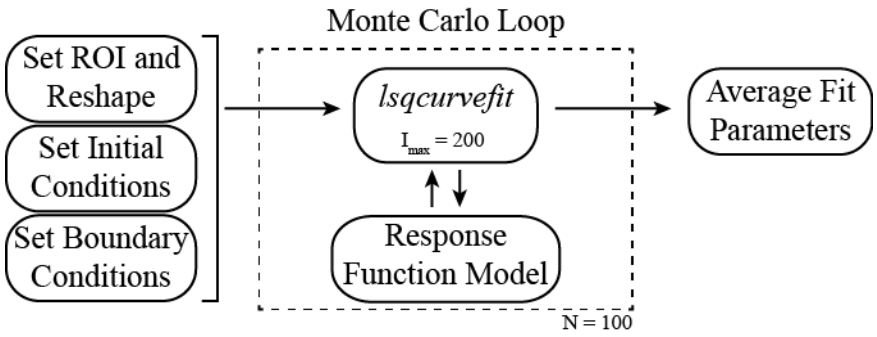

Figure C-6 Flow chart describing the fitting routine when it is combined with a Monte Carlo distribution of starting conditions. The experimental region of interest (ROI) is important to ensure that the simulated data is fit only to the experimental data corresponding to the signal. A tight bound for the ROI is essential for the fits to converge properly. The initial conditions vary throughout the Monte Carlo loops by the angles associated with the FeRu structure. There were 100 different geometries sampled over the course of the fit. The fitting function was limited to 200 iterations and 1000 function evaluations.

The MATLAB code provided here is broken up into the 9 different scripts and functions necessary to perform the data fitting including angle restriction and Monte Carlo geometry sampling.

C.3.1 VEfit_input_MC

```
clear all; clc;
tic

%dbstop if error  %use if debugging

NTrials = 100; %number of geometries sampled
ExpSet = 1; % 1 for the data from 5/15/18 and 2 for data from
5/18/18 still need to choose which polarization etc.

diary('FitCommandLine') %determine if iteration failed

if ExpSet == 1
    load('C:\Users\Khalil Group\Desktop\VE_Fitting\FitData2')
    FT_size = 4096;
else
    load('FitData_052518')
    FT_size = 8192;
end
Exp_Omega_1 = Omega_1;
Exp_Omega_3 = Omega_3;
%%%%%  VE fit input/run file
```

```
ExpROI = [1995, 2097, 11600, 10900];
E_index_P = 1; % ZZZZ: 1=150, 2=260 ZZYY: 3=150, 4=260
P_index_P = 2; % 1=ZZZZ t,260; 2=ZZZZ t,150; 3=ZZYY all %for
0525 data: 1 = ZZZZ, 3 = ZZYY

E_index_X = 3; % ZZZZ: 1=150, 2=260 ZZYY: 3=150, 4=260
P_index_X = 3; % 1=ZZZZ t,260; 2=ZZZZ t,150; 3=ZZYY all %for
0525 data: 1 = ZZZZ, 3 = ZZYY

w1 = 2002;
w2 = 2050;
w3 = 2089;
we = 11400;
muE1 = 1;
muE2 = 0.7;
muE3 = 2;
theta3 = 5;
thetabt = 6+2.5.*rand(NTrials,1);
thetabr = 88+2.5.*rand(NTrials,1);
thetatr = 85+2.5.*rand(NTrials,1);
ge = 400;
step_IR = 1.055; %fs
step_e = 0.5; %fs
R_IR = 4000; % # of steps
R_e = 1000; % # of steps
t1 = ((1:R_IR)-1).*step_IR;
t3 = ((1:R_e)-1).*step_e;
[T1, T3] = meshgrid(t1,t3);

TAx = cat(3,T1,T3);

dOIR = Omega_1(2);

Exp_ROI_I(1) = floor(ExpROI(1)./dOIR)+1;
Exp_ROI_I(2) = ceil(ExpROI(2)./dOIR)+1;
[~, Exp_ROI_I(3)] = min(abs(Omega_3-ExpROI(3)));
[~, Exp_ROI_I(4)] = min(abs(Omega_3-ExpROI(4)));

if ExpSet == 1
    FT_CCD_div_ZZZZ = bsxfun(@rdivide, squeeze(FT_CCD( ...
          E_index_P, :, :))',ProbeDivision(:, P_index_P));

    FT_CCD_div_ZZYY = bsxfun(@rdivide,squeeze(FT_CCD( ...
          E_index_X, :, :))',ProbeDivision(:, P_index_X));

else
    FT_CCD_div_ZZZZ = bsxfun(@rdivide, FT_CCD_smooth_ZZZZ, ...
```

```
            ProbeSpectra(:, P_index_P));
        FT_CCD_div_ZZYY = bsxfun(@rdivide, FT_CCD_smooth_ZZYY, ...
            ProbeSpectra(:, P_index_X));

end

O1_spline = (Omega_1(Exp_ROI_I(1)):1:Omega_1(Exp_ROI_I(2)));
ExpData_ZZZZ = interp1(Omega_1(Exp_ROI_I(1):Exp_ROI_I(2)), ...
     FT_CCD_div_ZZZZ(Exp_ROI_I(3):Exp_ROI_I(4), ...
     Exp_ROI_I(1):Exp_ROI_I(2))', O1_spline,'spline')';

ExpData_ZZYY = 3.*interp1(Omega_1(Exp_ROI_I(1):Exp_ROI_I( ...
     2)),  FT_CCD_div_ZZYY(Exp_ROI_I(3):Exp_ROI_I(4), ...
     Exp_ROI_I(1):Exp_ROI_I(2))', O1_spline,'spline')';

ExpData_comb = cat(3,ExpData_ZZZZ,ExpData_ZZYY);

f0 = [w1, w2, w3, we, muE1, muE2, muE3, theta3, ge];
lb = [2000, 2000, 2000, 9000, 0, 0, 0, 0, 0];
ub = [2040, 2100, 2095, 15000, inf, inf, inf, 90, inf];
options=optimset('MaxFunEvals', 10000, 'MaxIter', 200);
f2 = zeros(11,NTrials);
ci2 = zeros(9,2,NTrials);

for ii = 1:NTrials
    PassFun = @(f,TAx)VEfit_MC_noglobal(f, TAx,thetabt(ii), ...
          thetatr(ii), thetabr(ii), Exp_ROI_I, Exp_Omega_1, ...
          Exp_Omega_3);
    [f,resnorm,resid,exitflag,output,lambda,jacob] = ...
          lsqcurvefit(PassFun, f0, TAx, ExpData_comb, lb, ...
          ub, options);
    ci =  nlparci(f,resid,'jacobian',jacob);
    s2 = var(resid);
    [theta1, theta2] = FeRuAngles_MC(f(8), thetabt(ii), ...
          thetabr(ii), thetatr(ii));
    f2(:,ii) = [f(1:7),theta1,theta2,f(8:9)];
    ci2(:,:,ii) = ci;
    disp(['Iteration', num2str(ii)])
    save('MC_Fit_output','f2','ci2')

end

disp('end')

toc
```

C.3.2 VEfit_MC

```
function [ Sim_comb ] = VEfit_MC(f, Tax, thetabt, thetatr, ...
     thetabr, Exp_ROI_I, Exp_Omega_1, Exp_Omega_3)

%frozen parameters
muIR1 = 1;
muIR2 = 0.56;
muIR3 = 0.22;
gIR1 = 20.5*2*pi()*c();
gIR2 = 8.7*2*pi()*c();
gIR3 = 5.3*2*pi()*c();
[theta1, theta2] = FeRuAngles_MC(f(8),thetabt,thetatr,thetabr);

f_units = [f(1:7),theta1,theta2,f(8:9)];
f_units(1:4) = f(1:4).*2.*pi().*c();
f_units(11) = f(9)*2*pi()*c();
f_units(8:10) = f_units(8:10).*pi()./180;

FT_size = 4096;
step_IR = 1.055; %fs
step_e = 0.5; %fs
R_IR = 4000; %fs
R_e = 1000; %fs
t1 = ((1:R_IR)-1).*step_IR;
t3 = ((1:R_e)-1).*step_e;

%[T1, T3] = meshgrid(t1,t3);


T1 = Tax(:,:,1);
T3 = Tax(:,:,2);

[R1, NR1] = ESAResponse(muIR1,f_units(5), f_units(1), ...
     f_units(4), gIR1, f_units(11),T1,T3);

[R2, NR2] = ESAResponse(muIR2, f_units(6), f_units(2), ...
     f_units(4), gIR2, f_units(11), T1, T3);

[R3, NR3] = ESAResponse(muIR3, f_units(7), f_units(3), ...
     f_units(4), gIR3, f_units(11), T1, T3);

Y1_ZZZZ = ParPolarESA(f_units(8));
Y2_ZZZZ = ParPolarESA(f_units(9));
Y3_ZZZZ = ParPolarESA(f_units(10));

Y1_ZZYY = XPolarESA(f_units(8));
Y2_ZZYY = XPolarESA(f_units(9));
Y3_ZZYY = XPolarESA(f_units(10));
```

```
RR_ZZZZ = real(Y1_ZZZZ*R1+Y2_ZZZZ*R2+Y3_ZZZZ*R3);
RNR_ZZZZ = real(Y1_ZZZZ*NR1+Y2_ZZZZ*NR2+Y3_ZZZZ*NR3);

RR_ZZYY = real(Y1_ZZYY*R1+Y2_ZZYY*R2+Y3_ZZYY*R3);
RNR_ZZYY = real(Y1_ZZYY*NR1+Y2_ZZYY*NR2+Y3_ZZYY*NR3);

fd_R_ZZZZ = fft2(RR_ZZZZ,FT_size/2,FT_size);
fd_NR_temp_ZZZZ = fft2(RNR_ZZZZ,FT_size/2,FT_size);
fd_NR_ZZZZ = [fd_NR_temp_ZZZZ(:,2:end),fd_NR_temp_ZZZZ(:,1)];
%nonrephasing requires assymetric shift to properly align

fd_NR_ZZZZ = fliplr(fd_NR_ZZZZ);
fd_R_shift_ZZZZ = real(fftshift(fd_R_ZZZZ));
fd_NR_shift_ZZZZ = real(fftshift(fd_NR_ZZZZ));

fd_R_ZZYY = fft2(RR_ZZYY,FT_size/2,FT_size);
fd_NR_temp_ZZYY = fft2(RNR_ZZYY,FT_size/2,FT_size);
fd_NR_ZZYY = [fd_NR_temp_ZZYY(:,2:end),fd_NR_temp_ZZYY(:,1)];
%nonrephasing requires assymetric shift to properly align

fd_NR_ZZYY = fliplr(fd_NR_ZZYY);
fd_R_shift_ZZYY = real(fftshift(fd_R_ZZYY));
fd_NR_shift_ZZYY = real(fftshift(fd_NR_ZZYY));

Freq_IR = GenFreqDomain_shift(step_IR,FT_size); %in cm-1
Freq_e = GenFreqDomain_shift(step_e,FT_size/2); %in cm-1

Abs_sig_ZZZZ = fd_R_shift_ZZZZ + fd_NR_shift_ZZZZ;
Abs_sig_ZZYY = 3.*(fd_R_shift_ZZYY + fd_NR_shift_ZZYY);

Sim_comb_tot = cat(3, Abs_sig_ZZZZ, Abs_sig_ZZYY);

[Sim_comb, EO1, EO3] = Fit_ROI_3D(Sim_comb_tot, Freq_IR, ...
     Freq_e, Exp_ROI_I, Exp_Omega_1, Exp_Omega_3);


end
```

C.3.3 FeRuAngles_MC

```
function [ theta_t, theta_r ] = FeRuAngles_MC( theta_b,...
     theta_bt, theta_br, theta_tr )

%unit vectors defining each normal mode
b = [0, 0, 1];
t = zeros(size(b));
r = zeros(size(b));
```

```
%solve for t and r *defining r as restricted to the ZY plane
(r(1) = 0)
t(3) = cos(theta_bt*pi()/180);
r(3) = cos(theta_br*pi()/180);
r(2) = sqrt(1-r(3)^2);
t(2) = (cos(theta_tr*pi()/180)-t(3)*r(3))/r(2);
t(1) = sqrt(1-t(2)^2-t(3)^2);

%rotational matrix about X in the new coordinate frame defined
by the
%electronic transition unit vector [0, 0, 1]
Rx = [1, 0, 0;...
    0, cos(theta_b*pi()/180), -sin(theta_b*pi()/180);...
    0, sin(theta_b*pi()/180), cos(theta_b*pi()/180)];

%new unit vectors rotated into the electronic frame of reference
Rb = b*Rx;
Rt = t*Rx;
Rr  = r*Rx;


%The experimentally relevant angles between the electronic
transition and
%vibrational coordinates (the bridge mode angle is an input)
theta_t = acos(dot([0,0,1],Rt))*180/pi();
theta_r = acos(dot([0,0,1],Rr))*180/pi();

end
```

C.3.4 Fit_ROI_3D

```
function [ Sim_ROI, O1_spline, expO3 ] = Fit_ROI_3D...
     ( Abs_sig,Freq_IR, Freq_e, Exp_ROI_I, Exp_Omega_1, ...
     Exp_Omega_3 )

%%%% spline onto experimental axis
[~,O1_I(1)] = min(abs(Freq_IR-Exp_Omega_1(Exp_ROI_I(1))));
[~,O1_I(2)] = min(abs(Freq_IR-Exp_Omega_1(Exp_ROI_I(2))));

[~,O3_I(1)] = min(abs(Freq_e-Exp_Omega_3(Exp_ROI_I(4))));
%switched order because Omega_3 is decreasing

[~,O3_I(2)] = min(abs(Freq_e-Exp_Omega_3(Exp_ROI_I(3))));

Abs_sig_cropped = Abs_sig(O3_I(1):O3_I(2),O1_I(1):O1_I(2),:);
O1_spline = (Exp_Omega_1(Exp_ROI_I(1)):1:Exp_Omega_1...
     (Exp_ROI_I(2)));

%Sim_ROI = zeros(Exp_ROI_I(4)-Exp_ROI_I(3)+1,length(O1_spline));
```

```
[SimX, SimY] = meshgrid(Freq_IR(O1_I(1):O1_I(2)), ...
     Freq_e(O3_I(1):O3_I(2)));

[SimXq, SimYq] = meshgrid(O1_spline,flipud( ...
     Exp_Omega_3(Exp_ROI_I(3):Exp_ROI_I(4))));

[m, n] = size(SimXq);

Sim_ROI = zeros(m,n,2);
for ii = 1:2
    Sim_ROI(:,:,ii) = interp2(SimX,SimY, ...
          Abs_sig_cropped(:,:,ii),SimXq,SimYq,'spline');
end

expO1 = Exp_Omega_1(Exp_ROI_I(1):Exp_ROI_I(2));
expO3 = Exp_Omega_3(Exp_ROI_I(3):Exp_ROI_I(4));
end
```

C.3.5 ESAResponse

```
function [ R, NR ] = ESAResponse( mu_1, mu_3, w_1, w_3, ...
     g_1, g_3, t_1, t_3)

R = -mu_1.^2.*mu_3.^2.*exp(-1i.*w_1.*t_1-g_1.*t_1) ...
     .*exp(-1i.*w_3.*t_3-g_3.*t_3);
NR = -mu_1.^2.*mu_3.^2.*exp(1i.*w_1.*t_1-g_1.*t_1) ...
     .*exp(-1i.*w_3.*t_3-g_3.*t_3);

end
```

C.3.6 ParPolarESA

```
function [ Yzzzz ] = ParPolarESA( Theta )

Yzzzz = (1/15)*(3*cos(Theta)^2+sin(Theta)^2);

end
```

C.3.7 XPolarESA

```
function [ Yzzyy ] = XPolarESA( Theta )

Yzzyy = (1/15)*(cos(Theta)^2+2*sin(Theta)^2);

end
```

C.3.8 GenFreqDomain

```
function [ FAx ] = GenFreqDomain( t_step, FT_size )
```

```
c = 2.9979248E-5; %speed of light cm/fs

f_range = 1/t_step;  %frequency range in 1/fs
f_step_hz = f_range/FT_size; %step size in 1/fs
f_step_wave = f_step_hz/c; %step size in cm-1

FAx = (0:FT_size-1).*f_step_wave;
end
```

C.3.9 GenFreqDomain_shift

```
function [ FAx ] = GenFreqDomain_shift( t_step, FT_size )


c = 2.9979248E-5; %speed of light cm/fs

f_range = 1/t_step;  %frequency range in 1/fs
f_step_hz = f_range/FT_size;  %step size in 1/fs
f_step_wave = f_step_hz/c;  %step size in cm-1

FAx = (-FT_size/2+1:FT_size/2).*f_step_wave;
end
```

Vita

Zachary W. Fox was born in Salt Lake City, UT in 1990. He graduated from Brighton High School in 2008 and began his undergraduate work at the University of Utah. There, he studied chemistry and received his Honors Bachelor of Science degree in May 2012. After beginning graduate school at the University of Washington in September 2012 he joined the Khalil Research group in February 2013. He completed his Doctor of Philosophy in Chemistry in August 2018.